Springer

Hand

Crysta
Growt

Springer Handbook of Crystal Growth

Springer Handbooks provide a concise compilation of approved key information on methods of research, general principles, and functional relationships in physical sciences and engineering. The world's leading experts in the fields of physics and engineering will be assigned by one or several renowned editors to write the chapters comprising each volume. The content is selected by these experts from Springer sources (books, journals, online content) and other systematic and approved recent publications of physical and technical information.

The volumes are designed to be useful as readable desk reference books to give a fast and comprehensive overview and easy retrieval of essential reliable key information, including tables, graphs, and bibliographies. References to extensive sources are provided.

Springer Handbook of Crystal Growth

Govindhan Dhanaraj, Kullaiah Byrappa,
Vishwanath Prasad, Michael Dudley (Eds.)

With DVD-ROM, 1320 Figures, 134 in four color and 124 Tables

Editors
Govindhan Dhanaraj
ARC Energy
18 Celina Avenue, Unit 17
Nashua, NH 03063, USA
dhanaraj@arc-energy.com

Kullaiah Byrappa
Department of Geology
University of Mysore
Manasagangotri
Mysore 570 006, India
kbyrappa@gmail.com

Vishwanath Prasad
University of North Texas
1155 Union Circle #310979
Denton, TX 76203-5017, USA
vish.prasad@unt.edu

Michael Dudley
Department of Materials Science & Engineering
Stony Brook University
Stony Brook, NY 11794-2275, USA
mdudley@notes.cc.sunysb.edu

ISBN: 978-3-540-74182-4 e-ISBN: 978-3-540-74761-1
DOI 10.1007/978-3-540-74761-1
Springer Heidelberg Dordrecht London New York

Library of Congress Control Number: 2008942133

© Springer-Verlag Berlin Heidelberg 2010
This work is subject to copyright. All rights are reserved, whether the whole or part of the material is concerned, specifically the rights of translation, reprinting, reuse of illustrations, recitation, broadcasting, reproduction on microfilm or in any other way, and storage in data banks. Duplication of this publication or parts thereof is permitted only under the provisions of the German Copyright Law of September 9, 1965, in its current version, and permission for use must always be obtained from Springer. Violations are liable to prosecution under the German Copyright Law.
The use of general descriptive names, registered names, trademarks, etc. in this publication does not imply, even in the absence of a specific statement, that such names are exempt from the relevant protective laws and regulations and therefore free for general use.

Production and typesetting: le-tex publishing services GmbH, Leipzig
Senior Manager Springer Handbook: Dr. W. Skolaut, Heidelberg
Typography and layout: schreiberVIS, Seeheim
Illustrations: Hippmann GbR, Schwarzenbruck
Cover design: eStudio Calamar Steinen, Barcelona
Cover production: WMXDesign GmbH, Heidelberg
Printing and binding: Stürtz GmbH, Würzburg

Printed on acid free paper

Springer is part of Springer Science+Business Media (www.springer.com)

57/3180/YL 5 4 3 2 1 0

Preface

Over the years, many successful attempts have been made to describe the art and science of crystal growth, and many review articles, monographs, symposium volumes, and handbooks have been published to present comprehensive reviews of the advances made in this field. These publications are testament to the growing interest in both bulk and thin-film crystals because of their electronic, optical, mechanical, microstructural, and other properties, and their diverse scientific and technological applications. Indeed, most modern advances in semiconductor and optical devices would not have been possible without the development of many elemental, binary, ternary, and other compound crystals of varying properties and large sizes. The literature devoted to basic understanding of growth mechanisms, defect formation, and growth processes as well as the design of growth systems is therefore vast.

The objective of this Springer Handbook is to present the state of the art of selected topical areas of both bulk and thin-film crystal growth. Our goal is to make readers understand the basics of the commonly employed growth processes, materials produced, and defects generated. To accomplish this, we have selected more than 50 leading scientists, researchers, and engineers, and their many collaborators from 22 different countries, to write chapters on the topics of their expertise. These authors have written 52 chapters on the fundamentals of crystal growth and defect formation; bulk growth from the melt, solution, and vapor; epitaxial growth; modeling of growth processes and defects; and techniques of defect characterization, as well as some contemporary special topics.

This Springer Handbook is divided into seven parts. Part A presents the fundamentals: an overview of the growth and characterization techniques, followed by the state of the art of nucleation at surfaces, morphology of crystals grown from solutions, nucleation of dislocation during growth, and defect formation and morphology.

Part B is devoted to bulk growth from the melt, a method critical to producing large-size crystals. The chapters in this part describe the well-known processes such as Czochralski, Kyropoulos, Bridgman, and floating zone, and focus specifically on recent advances in improving these methodologies such as application of magnetic fields, orientation of the growth axis, introduction of a pedestal, and shaped growth. They also cover a wide range of materials from silicon and III–V compounds to oxides and fluorides.

The third part, Part C of the book, focuses on solution growth. The various aspects of hydrothermal growth are discussed in two chapters, while three other chapters present an overview of the nonlinear and laser crystals, KTP and KDP. The knowledge on the effect of gravity on solution growth is presented through a comparison of growth on Earth versus in a microgravity environment.

The topic of Part D is vapor growth. In addition to presenting an overview of vapor growth, this part also provides details on vapor growth of silicon carbide, gallium nitride, aluminum nitride, and organic semiconductors. This is followed by chapters on epitaxial growth and thin films in Part E. The topics range from chemical vapor deposition to liquid-phase epitaxy to pulsed laser and pulsed electron deposition.

Modeling of both growth processes and defect formation is presented in Part F. These chapters demonstrate the direct correlation between the process parameters and quality of the crystal produced, including the formation of defects. The subsequent Part G presents the techniques that have been developed for crystalline material characterization and analysis. The chapters in Parts F and G demonstrate how well predictive tools and analytical techniques have helped the design and control of growth processes for better-quality crystals of large sizes.

The final Part H is devoted to some selected contemporary topics in this field, such as protein crystal growth, crystallization from gels, in situ structural studies, growth of single-crystal scintillation materials, photovoltaic materials, and wire-saw slicing of large crystals to produce wafers.

We hope this Springer Handbook will be useful to graduate students studying crystal growth and to re-

searchers, scientists, and engineers from academia and industry who are conducting or intend to conduct research in this field as well as those who grow crystals.

We would like to express our sincere thanks to Dr. Claus Acheron and Dr. Werner Skolaut of Springer and Ms Anne Strohbach of le-tex for their extraordinary efforts without which this handbook would not have taken its final shape.

We thank our authors for writing comprehensive chapters and having patience with us during the publication of this Handbook. One of the editors (GD) would like to thank his family members and Dr. Kedar Gupta (CEO of ARC Energy) for their generous support and encouragement during the entire course of editing this handbook. Acknowledgements are also due to Peter Rudolf, David Bliss, Ishwara Bhat, and Partha Dutta for their help in editing Parts A, B, E, and H, respectively.

Nashua, New Hampshire, April 2010 G. Dhanaraj
Mysore, India K. Byrappa
Denton, Texas V. Prasad
Stony Brook, New York M. Dudley

About the Editors

Govindhan Dhanaraj is the Manager of Crystal Growth Technologies at Advanced Renewable Energy Company (ARC Energy) at Nashua, New Hampshire (USA) focusing on the growth of large size sapphire crystals for LED lighting applications, characterization and related crystal growth furnace development. He received his PhD from the Indian Institute of Science, Bangalore and his Master of Science from Anna University (India). Immediately after his doctoral degree, Dr. Dhanaraj joined a National Laboratory, presently known as Rajaramanna Center for Advanced Technology in India, where he established an advanced Crystal Growth Laboratory for the growth of optical and laser crystals. Prior to joining ARC Energy, Dr. Dhanaraj served as a Research Professor at the Department of Materials Science and Engineering, Stony Brook University, NY, and also held a position of Research Assistant Professor at Hampton University, VA. During his 25 years of focused expertise in crystal growth research, he has developed optical, laser and semiconductor bulk crystals and SiC epitaxial films using solution, flux, Czochralski, Bridgeman, gel and vapor methods, and characterized them using x-ray topography, synchrotron topography, chemical etching and optical and atomic force microscopic techniques. He co-organized a symposium on Industrial Crystal Growth under the 17th American Conference on Crystal Growth and Epitaxy in conjunction with the 14th US Biennial Workshop on Organometallic Vapor Phase Epitaxy held at Lake Geneva, WI in 2009. Dr. Dhanaraj has delivered invited lectures and also served as session chairman in many crystal growth and materials science meetings. He has published over 100 papers and his research articles have attracted over 250 rich citations.

Kullaiah Byrappa received his Doctor's degree in Crystal Growth from the Moscow State University, Moscow in 1981. He is Professor of Materials Science, Head of the Crystal Growth Laboratory, and Director of the Internal Quality Assurance Cell of the University of Mysore, India. His current research is in crystal engineering of polyscale materials through novel solution processing routes, particularly covering hydrothermal, solvothermal and supercritical methods. Professor Byrappa has co-authored the Handbook of Hydrothermal Technology, and edited 4 books as well as two special editions of Journal of Materials Science, and published 180 research papers including 26 invited reviews and book chapters on various aspects of novel routes of solution processing. Professor Byrappa has delivered over 60 keynote and invited lectures at International Conferences, and several hundreds of colloquia and seminars at various institutions around the world. He has also served as chair and co-chair for numerous international conferences. He is a Fellow of the World Academy of Ceramics. Professor Byrappa is serving in several international committees and commissions related to crystallography, crystal growth, and materials science. He is the Founder Secretary of the International Solvothermal and Hydrothermal Association. Professor Byrappa is a recipient of several awards such as the Sir C.V. Raman Award, Materials Research Society of India Medal, and the Golden Jubilee Award of the University of Mysore.

Vishwanath "Vish" Prasad is the Vice President for Research and Economic Development and Professor of Mechanical and Energy Engineering at the University of North Texas (UNT), one of the largest university in the state of Texas. He received his PhD from the University of Delaware (USA), his Masters of Technology from the Indian Institute of Technology, Kanpur, and his bachelor's from Patna University in India all in Mechanical Engineering. Prior to joining UNT in 2007, Dr. Prasad served as the Dean at Florida International University (FIU) in Miami, where he also held the position of Distinguished Professor of Engineering. Previously, he has served as a Leading Professor of Mechanical Engineering at Stony Brook University, New York, as an Associate Professor and Assistant Professor at Columbia University. He has received many special recognitions for his contributions to engineering education. Dr. Prasad's research interests include thermo-fluid sciences, energy systems, electronic materials, and computational materials processing. He has published over 200 articles, edited/co-edited several books and organized numerous conferences, symposia, and workshops. He serves as the lead editor of the Annual Review of Heat Transfer. In the past, he has served as an Associate Editor of the ASME Journal of Heat. Dr. Prasad is an elected Fellow of the American Society of Mechanical Engineers (ASME), and has served as a member of the USRA Microgravity Research Council. Dr. Prasad's research has focused on bulk growth of silicon, III-V compounds, and silicon carbide; growth of large diameter Si tube; design of crystal growth systems; and sputtering and chemical vapor deposition of thin films. He is also credited to initiate research on wire saw cutting of large crystals to produce wafers with much reduced material loss. Dr. Prasad's research has been well funded by US National Science Foundation (NSF), US Department of Defense, US Department of Energy, and industry.

Michael Dudley received his Doctoral Degree in Engineering from Warwick University, UK, in 1982. He is Professor and Chair of the Materials Science and Engineering Department at Stony Brook University, New York, USA. He is director of the Stony Brook Synchrotron Topography Facility at the National Synchrotron Light Source at Brookhaven National Laboratory, Upton New York. His current research focuses on crystal growth and characterization of defect structures in single crystals with a view to determining their origins. The primary technique used is synchrotron topography which enables analysis of defects and generalized strain fields in single crystals in general, with particular emphasis on semiconductor, optoelectronic, and optical crystals. Establishing the relationship between crystal growth conditions and resulting defect distributions is a particular thrust area of interest to Dudley, as is the correlation between electronic/optoelectronic device performance and defect distribution. Other techniques routinely used in such analysis include transmission electron microscopy, high resolution triple-axis x-ray diffraction, atomic force microscopy, scanning electron microscopy, Nomarski optical microscopy, conventional optical microscopy, IR microscopy and fluorescent laser scanning confocal microscopy. Dudley's group has played a prominent role in the development of SiC and AlN growth, characterizing crystals grown by many of the academic and commercial entities involved enabling optimization of crystal quality. He has co-authored some 315 refereed articles and 12 book chapters, and has edited 5 books. He is currently a member of the Editorial Board of Journal of Applied Physics and Applied Physics Letters and has served as Chair or Co-Chair for numerous international conferences.

List of Authors

Francesco Abbona
Università degli Studi di Torino
Dipartimento di Scienze Mineralogiche
e Petrologiche
via Valperga Caluso 35
10125 Torino, Italy
e-mail: *francesco.abbona@unito.it*

Mohan D. Aggarwal
Alabama A&M University
Department of Physics
Normal, AL 35762, USA
e-mail: *mohan.aggarwal@aamu.edu*

Marcello R.B. Andreeta
University of São Paulo
Crystal Growth and Ceramic Materials Laboratory,
Institute of Physics of São Carlos
Av. Trabalhador Sãocarlense, 400
São Carlos, SP 13560-970, Brazil
e-mail: *marcello@if.sc.usp.br*

Dino Aquilano
Università degli Studi di Torino
Facoltà di Scienze Matematiche, Fisiche e Naturali
via P. Giuria, 15
Torino, 10126, Italy
e-mail: *dino.aquilano@unito.it*

Roberto Arreguín-Espinosa
Universidad Nacional Autónoma de México
Instituto de Química
Circuito Exterior, C.U. s/n
Mexico City, 04510, Mexico
e-mail: *arrespin@unam.mx*

Jie Bai
Intel Corporation
RA3-402, 5200 NE Elam Young Parkway
Hillsboro, OR 97124-6497, USA
e-mail: *jie.bai@intel.com*

Stefan Balint
West University of Timisoara
Department of Computer Science
Blvd. V. Parvan 4
Timisoara, 300223, Romania
e-mail: *balint@math.uvt.ro*

Ashok K. Batra
Alabama A&M University
Department of Physics
4900 Meridian Street
Normal, AL 35762, USA
e-mail: *ashok.batra@aamu.edu*

Handady L. Bhat
Indian Institute of Science
Department of Physics
CV Raman Avenue
Bangalore, 560012, India
e-mail: *hlbhat@physics.iisc.ernet.in*

Ishwara B. Bhat
Rensselaer Polytechnic Institute
Electrical Computer
and Systems Engineering Department
110 8th Street, JEC 6031
Troy, NY 12180, USA
e-mail: *bhati@rpi.edu*

David F. Bliss
US Air Force Research Laboratory
Sensors Directorate Optoelectronic Technology
Branch
80 Scott Drive
Hanscom AFB, MA 01731, USA
e-mail: *david.bliss@hanscom.af.mil*

Mikhail A. Borik
Russian Academy of Sciences
Laser Materials and Technology Research Center,
A.M. Prokhorov General Physics Institute
Vavilov 38
Moscow, 119991, Russia
e-mail: *borik@lst.gpi.ru*

Liliana Braescu
West University of Timisoara
Department of Computer Science
Blvd. V. Parvan 4
Timisoara, 300223, Romania
e-mail: *lilianabraescu@balint1.math.uvt.ro*

Kullaiah Byrappa
University of Mysore
Department of Geology
Manasagangotri
Mysore, 570 006, India
e-mail: *kbyrappa@gmail.com*

Dang Cai
CVD Equipment Corporation
1860 Smithtown Ave.
Ronkonkoma, NY 11779, USA
e-mail: *dcai@cvdequipment.com*

Michael J. Callahan
GreenTech Solutions
92 Old Pine Drive
Hanson, MA 02341, USA
e-mail: *mjcal37@yahoo.com*

Joan J. Carvajal
Universitat Rovira i Virgili (URV)
Department of Physics and Crystallography
of Materials and Nanomaterials (FiCMA-FiCNA)
Campus Sescelades, C/ Marcel·lí Domingo, s/n
Tarragona 43007, Spain
e-mail: *joanjosep.carvajal@urv.cat*

Aaron J. Celestian
Western Kentucky University
Department of Geography and Geology
1906 College Heights Blvd.
Bowling Green, KY 42101, USA
e-mail: *aaron.celestian@wku.edu*

Qi-Sheng Chen
Chinese Academy of Sciences
Institute of Mechanics
15 Bei Si Huan Xi Road
Beijing, 100190, China
e-mail: *qschen@imech.ac.cn*

Chunhui Chung
Stony Brook University
Department of Mechanical Engineering
Stony Brook, NY 11794-2300, USA
e-mail: *chuchung@ic.sunysb.edu*

Ted Ciszek
Geolite/Siliconsultant
31843 Miwok Trl.
Evergreen, CO 80437, USA
e-mail: *ted_ciszek@siliconsultant.com*

Abraham Clearfield
Texas A&M University
Distinguished Professor of Chemistry
College Station, TX 77843-3255, USA
e-mail: *clearfield@chem.tamu.edu*

Hanna A. Dabkowska
Brockhouse Institute for Materials Research
Department of Physics and Astronomy
1280 Main Str W.
Hamilton, Ontario L8S 4M1, Canada
e-mail: *dabkoh@mcmaster.ca*

Antoni B. Dabkowski
McMaster University, BIMR
Brockhouse Institute for Materials Research,
Department of Physics and Astronomy
1280 Main Str W.
Hamilton, Ontario L8S 4M1, Canada
e-mail: *dabko@mcmaster.ca*

Rafael Dalmau
HexaTech Inc.
991 Aviation Pkwy Ste 800
Morrisville, NC 27560, USA
e-mail: *rdalmau@hexatechinc.com*

Govindhan Dhanaraj
ARC Energy
18 Celina Avenue, Unit 77
Nashua, NH 03063, USA
e-mail: *dhanaraj@arc-energy.com*

Ramasamy Dhanasekaran
Anna University Chennai
Crystal Growth Centre
Chennai, 600 025, India
e-mail: *rdhanasekaran@annauniv.edu;*
rdcgc@yahoo.com

Ernesto Diéguez
Universidad Autónoma de Madrid
Department Física de Materiales
Madrid 28049, Spain
e-mail: *ernesto.dieguez@uam.es*

Vijay K. Dixit
Raja Ramanna Center for Advance Technology
Semiconductor Laser Section,
Solid State Laser Division
Rajendra Nagar, RRCAT.
Indore, 452013, India
e-mail: *dixit@rrcat.gov.in*

Sadik Dost
University of Victoria
Crystal Growth Laboratory
Victoria, BC V8W 3P6, Canada
e-mail: *sdost@me.uvic.ca*

Michael Dudley
Stony Brook University
Department of Materials Science and Engineering
Stony Brook, NY 11794-2275, USA
e-mail: *mdudley@notes.cc.sunysb.edu*

Partha S. Dutta
Rensselaer Polytechnic Institute
Department of Electrical, Computer
and Systems Engineering
110 Eighth Street
Troy, NY 12180, USA
e-mail: *duttap@rpi.edu*

Francesc Díaz
Universitat Rovira i Virgili (URV)
Department of Physics and Crystallography
of Materials and Nanomaterials (FiCMA-FiCNA)
Campus Sescelades, C/ Marcel·lí Domingo, s/n
Tarragona 43007, Spain
e-mail: *f.diaz@urv.cat*

Paul F. Fewster
PANalytical Research Centre,
The Sussex Innovation Centre
Research Department
Falmer
Brighton, BN1 9SB, UK
e-mail: *paul.fewster@panalytical.com*

Donald O. Frazier
NASA Marshall Space Flight Center
Engineering Technology Management Office
Huntsville, AL 35812, USA
e-mail: *donald.o.frazier@nasa.gov*

James W. Garland
EPIR Technologies, Inc.
509 Territorial Drive, Ste. B
Bolingbrook, IL 60440, USA
e-mail: *jgarland@epir.com*

Thomas F. George
University of Missouri-St. Louis
Center for Nanoscience,
Department of Chemistry and Biochemistry,
Department of Physics and Astronomy
One University Boulevard
St. Louis, MO 63121, USA
e-mail: *tfgeorge@umsl.edu*

Andrea E. Gutiérrez-Quezada
Universidad Nacional Autónoma de México
Instituto de Química
Circuito Exterior, C.U. s/n
Mexico City, 04510, Mexico
e-mail: *30111390@escolar.unam.mx*

Carl Hemmingsson
Linköping University
Department of Physics, Chemistry
and Biology (IFM)
581 83 Linköping, Sweden
e-mail: *cah@ifm.liu.se*

Antonio Carlos Hernandes
University of São Paulo
Crystal Growth and Ceramic Materials Laboratory,
Institute of Physics of São Carlos
Av. Trabalhador Sãocarlense
São Carlos, SP 13560-970, Brazil
e-mail: *hernandes@if.sc.usp.br*

Koichi Kakimoto
Kyushu University
Research Institute for Applied Mechanics
6-1 Kasuga-kouen, Kasuga
816-8580 Fukuoka, Japan
e-mail: *kakimoto@riam.kyushu-u.ac.jp*

Imin Kao
State University of New York at Stony Brook
Department of Mechanical Engineering
Stony Brook, NY 11794-2300, USA
e-mail: *imin.kao@stonybrook.edu*

John J. Kelly
Utrecht University,
Debye Institute for Nanomaterials Science
Department of Chemistry
Princetonplein 5
3584 CC, Utrecht, The Netherlands
e-mail: *j.j.kelly@uu.nl*

Jeonggoo Kim
Neocera, LLC
10000 Virginia Manor Road #300
Beltsville, MD, USA
e-mail: *kim@neocera.com*

Helmut Klapper
Institut für Kristallographie
RWTH Aachen University
Aachen, Germany
e-mail: *klapper@xtal.rwth-aachen.de; helmut-klapper@web.de*

Christine F. Klemenz Rivenbark
Krystal Engineering LLC
General Manager and Technical Director
1429 Chaffee Drive
Titusville, FL 32780, USA
e-mail: *ckr@krystalengineering.com*

Christian Kloc
Nanyang Technological University
School of Materials Science and Engineering
50 Nanyang Avenue
639798 Singapore
e-mail: *ckloc@ntu.edu.sg*

Solomon H. Kolagani
Neocera LLC
10000 Virginia Manor Road
Beltsville, MD 20705, USA
e-mail: *harsh@neocera.com*

Akinori Koukitu
Tokyo University of Agriculture and Technology (TUAT)
Department of Applied Chemistry
2-24-16 Naka-cho, Koganei
184-8588 Tokyo, Japan
e-mail: *koukitu@cc.tuat.ac.jp*

Milind S. Kulkarni
MEMC Electronic Materials
Polysilicon and Quantitative Silicon Research
501 Pearl Drive
St. Peters, MO 63376, USA
e-mail: *mkulkarni@memc.com*

Yoshinao Kumagai
Tokyo University of Agriculture and Technology
Department of Applied Chemistry
2-24-16 Naka-cho, Koganei
184-8588 Tokyo, Japan
e-mail: *4470kuma@cc.tuat.ac.jp*

Valentin V. Laguta
Institute of Physics of the ASCR
Department of Optical Materials
Cukrovarnicka 10
Prague, 162 53, Czech Republic
e-mail: *laguta@fzu.cz*

Ravindra B. Lal
Alabama Agricultural and Mechanical University
Physics Department
4900 Meridian Street
Normal, AL 35763, USA
e-mail: *rblal@comcast.net*

Chung-Wen Lan
National Taiwan University
Department of Chemical Engineering
No. 1, Sec. 4, Roosevelt Rd.
Taipei, 106, Taiwan
e-mail: *cwlan@ntu.edu.tw*

Hongjun Li
Chinese Academy of Sciences
R & D Center of Synthetic Crystals,
Shanghai Institute of Ceramics
215 Chengbei Rd., Jiading District
Shanghai, 201800, China
e-mail: *lh_li@mail.sic.ac.cn*

Elena E. Lomonova
Russian Academy of Sciences
Laser Materials and Technology Research Center,
A.M. Prokhorov General Physics Institute
Vavilov 38
Moscow, 119991, Russia
e-mail: *lomonova@lst.gpi.ru*

Ivan V. Markov
Bulgarian Academy of Sciences
Institute of Physical Chemistry
Sofia, 1113, Bulgaria
e-mail: *imarkov@ipc.bas.bg*

Bo Monemar
Linköping University
Department of Physics, Chemistry and Biology
58183 Linköping, Sweden
e-mail: *bom@ifm.liu.se*

Abel Moreno
Universidad Nacional Autónoma de México
Instituto de Química
Circuito Exterior, C.U. s/n
Mexico City, 04510, Mexico
e-mail: *carcamo@unam.mx*

Roosevelt Moreno Rodriguez
State University of New York at Stony Brook
Department of Mechanical Engineering
Stony Brook, NY 11794-2300, USA
e-mail: *roosevelt@dove.eng.sunysb.edu*

S. Narayana Kalkura
Anna University Chennai
Crystal Growth Centre
Sardar Patel Road
Chennai, 600025, India
e-mail: *kalkura@annauniv.edu*

Mohan Narayanan
Reliance Industries Limited
1, Rich Branch court
Gaithersburg, MD 20878, USA
e-mail: *mohan.narayanan@ril.com*

Subramanian Natarajan
Madurai Kamaraj University
School of Physics
Palkalai Nagar
Madurai, India
e-mail: *s_natarajan50@yahoo.com*

Martin Nikl
Academy of Sciences of the Czech Republic (ASCR)
Department of Optical Crystals, Institute of Physics
Cukrovarnicka 10
Prague, 162 53, Czech Republic
e-mail: *nikl@fzu.cz*

Vyacheslav V. Osiko
Russian Academy of Sciences
Laser Materials and Technology Research Center,
A.M. Prokhorov General Physics Institute
Vavilov 38
Moscow, 119991, Russia
e-mail: *osiko@lst.gpi.ru*

John B. Parise
Stony Brook University
Chemistry Department
and Department of Geosciences
ESS Building
Stony Brook, NY 11794-2100, USA
e-mail: *john.parise@stonybrook.edu*

Srinivas Pendurti
ASE Technologies Inc.
11499, Chester Road
Cincinnati, OH 45246, USA
e-mail: *spendurti@asetech.com*

Benjamin G. Penn
NASA/George C. Marshall Space Flight Center
ISHM and Sensors Branch
Huntsville, AL 35812, USA
e-mail: *benjamin.g.penndr@nasa.gov*

Jens Pflaum
Julius-Maximilians Universität Würzburg
Institute of Experimental Physics VI
Am Hubland
97078 Würzburg, Germany
e-mail: *jpflaum@physik.uni-wuerzburg.de*

Jose Luis Plaza
Universidad Autónoma de Madrid
Facultad de Ciencias,
Departamento de Física de Materiales
Madrid 28049, Spain
e-mail: *joseluis.plaza@uam.es*

Udo W. Pohl
Technische Universität Berlin
Institut für Festkörperphysik EW5-1
Hardenbergstr. 36
10623 Berlin, Germany
e-mail: *pohl@physik.tu-berlin.de*

Vishwanath (Vish) Prasad
University of North Texas
1155 Union Circle
Denton, TX 76203-5017, USA
e-mail: *vish.prasad@unt.edu*

Maria Cinta Pujol
Universitat Rovira i Virgili
Department of Physics and Crystallography
of Materials and Nanomaterials (FiCMA-FiCNA)
Campus Sescelades, C/ Marcel·lí Domingo
Tarragona 43007, Spain
e-mail: *mariacinta.pujol@urv.cat*

Balaji Raghothamachar
Stony Brook University
Department of Materials Science and Engineering
310 Engineering Building
Stony Brook, NY 11794-2275, USA
e-mail: *braghoth@notes.cc.sunysb.edu*

Michael Roth
The Hebrew University of Jerusalem
Department of Applied Physics
Bergman Bld., Rm 206, Givat Ram Campus
Jerusalem 91904, Israel
e-mail: *mroth@vms.huji.ac.il*

Peter Rudolph
Leibniz Institute for Crystal Growth
Technology Development
Max-Born-Str. 2
Berlin, 12489, Germany
e-mail: *rudolph@ikz-berlin.de*

Akira Sakai
Osaka University
Department of Systems Innovation
1-3 Machikaneyama-cho, Toyonaka-shi
560-8531 Osaka, Japan
e-mail: *sakai@ee.es.osaka-u.ac.jp*

Yasuhiro Shiraki
Tokyo City University
Advanced Research Laboratories,
Musashi Institute of Technology
8-15-1 Todoroki, Setagaya-ku
158-0082 Tokyo, Japan
e-mail: *yshiraki@tcu.ac.jp*

Theo Siegrist
Florida State University
Department of Chemical
and Biomedical Engineering
2525 Pottsdamer Street
Tallahassee, FL 32310, USA
e-mail: *siegrist@eng.fsu.edu*

Zlatko Sitar
North Carolina State University
Materials Science and Engineering
1001 Capability Dr.
Raleigh, NC 27695, USA
e-mail: *sitar@ncsu.edu*

Sivalingam Sivananthan
University of Illinois at Chicago
Department of Physics
845 W. Taylor St. M/C 273
Chicago, IL 60607-7059, USA
e-mail: *siva@uic.edu; siva@epir.com*

Mikhail D. Strikovski
Neocera LLC
10000 Virginia Manor Road, suite 300
Beltsville, MD 20705, USA
e-mail: *strikovski@neocera.com*

Xun Sun
Shandong University
Institute of Crystal Materials
Shanda Road
Jinan, 250100, China
e-mail: *sunxun@icm.sdu.edu.cn*

Ichiro Sunagawa
University Tohoku University (Emeritus)
Kashiwa-cho 3-54-2, Tachikawa
Tokyo, 190-0004, Japan
e-mail: *i.sunagawa@nifty.com*

Xu-Tang Tao
Shandong University
State Key Laboratory of Crystal Materials
Shanda Nanlu 27, 250100
Jinan, China
e-mail: *txt@sdu.edu.cn*

Vitali A. Tatartchenko
Saint – Gobain, 23 Rue Louis Pouey
92800 Puteaux, France
e-mail: *vitali.tatartchenko@orange.fr*

Filip Tuomisto
Helsinki University of Technology
Department of Applied Physics
Otakaari 1 M
Espoo TKK 02015, Finland
e-mail: *filip.tuomisto@tkk.fi*

Anna Vedda
University of Milano-Bicocca
Department of Materials Science
Via Cozzi 53
20125 Milano, Italy
e-mail: *anna.vedda@unimib.it*

Lu-Min Wang
University of Michigan
Department of Nuclear Engineering
and Radiological Sciences
2355 Bonisteel Blvd.
Ann Arbor, MI 48109-2104, USA
e-mail: *lmwang@umich.edu*

Sheng-Lai Wang
Shandong University
Institute of Crystal Materials,
State Key Laboratory of Crystal Materials
Shanda Road No. 27
Jinan, Shandong, 250100, China
e-mail: *slwang@icm.sdu.edu.cn*

Shixin Wang
Micron Technology Inc.
TEM Laboratory
8000 S. Federal Way
Boise, ID 83707, USA
e-mail: *shixinwang@micron.com*

Jan L. Weyher
Polish Academy of Sciences Warsaw
Institute of High Pressure Physics
ul. Sokolowska 29/37
01/142 Warsaw, Poland
e-mail: *weyher@unipress.waw.pl*

Jun Xu
Chinese Academy of Sciences
Shanghai Institute of Ceramics
Shanghai, 201800, China
e-mail: *xujun@mail.shcnc.ac.cn*

Hui Zhang
Tsinghua University
Department of Engineering Physics
Beijing, 100084, China
e-mail: *zhhui@tsinghua.edu.cn*

Lili Zheng
Tsinghua University
School of Aerospace
Beijing, 100084, China
e-mail: *zhenglili@tsinghua.edu.cn*

Mary E. Zvanut
University of Alabama at Birmingham
Department of Physics
1530 3rd Ave S
Birmingham, AL 35294-1170, USA
e-mail: *mezvanut@uab.edu*

Zbigniew R. Zytkiewicz
Polish Academy of Sciences
Institute of Physics
Al. Lotnikow 32/46
02668 Warszawa, Poland
e-mail: *zytkie@ifpan.edu.pl*

Contents

List of Abbreviations XXXI

Part A Fundamentals of Crystal Growth and Defect Formation

1 **Crystal Growth Techniques and Characterization: An Overview**
Govindhan Dhanaraj, Kullaiah Byrappa, Vishwanath (Vish) Prasad, Michael Dudley 3
1.1 Historical Developments 3
1.2 Theories of Crystal Growth 4
1.3 Crystal Growth Techniques 6
1.4 Crystal Defects and Characterization 11
References 15

2 **Nucleation at Surfaces**
Ivan V. Markov 17
2.1 Equilibrium Crystal–Ambient Phase 18
2.2 Work for Nucleus Formation 24
2.3 Rate of Nucleation 28
2.4 Saturation Nucleus Density 35
2.5 Second-Layer Nucleation in Homoepitaxy 38
2.6 Mechanism of Clustering in Heteroepitaxy 43
2.7 Effect of Surfactants on Nucleation 45
2.8 Conclusions and Outlook 48
References 48

3 **Morphology of Crystals Grown from Solutions**
Francesco Abbona, Dino Aquilano 53
3.1 Equilibrium Shape 55
3.2 The Theoretical Growth Shape 64
3.3 Factors Influencing the Crystal Habit 71
3.4 Surface Structure 72
3.5 Crystal Defects 73
3.6 Supersaturation – Growth Kinetics 73
3.7 Solvent 75
3.8 Impurities 78
3.9 Other Factors 84
3.10 Evolution of Crystal Habit 85
3.11 A Short Conclusion 86
3.A Appendix 86
References 87

4 **Generation and Propagation of Defects During Crystal Growth**
Helmut Klapper ... 93
4.1 Overview ... 94
4.2 Inclusions ... 95
4.3 Striations and Growth Sectors ... 101
4.4 Dislocations ... 107
4.5 Twinning ... 120
4.6 Perfection of Crystals Grown Rapidly from Solution ... 125
References ... 127

5 **Single Crystals Grown Under Unconstrained Conditions**
Ichiro Sunagawa ... 133
5.1 Background ... 134
5.2 Smooth and Rough Interfaces: Growth Mechanism and Morphology 136
5.3 Surface Microtopography ... 139
5.4 Growth Forms of Polyhedral Crystals ... 143
5.5 Internal Morphology ... 146
5.6 Perfection of Single Crystals ... 152
References ... 156

6 **Defect Formation During Crystal Growth from the Melt**
Peter Rudolph ... 159
6.1 Overview ... 159
6.2 Point Defects ... 163
6.3 Dislocations ... 176
6.4 Second-Phase Particles ... 188
6.5 Faceting ... 191
6.6 Twinning ... 193
6.7 Summary ... 194
References ... 195

Part B Crystal Growth from Melt Techniques

7 **Indium Phosphide: Crystal Growth and Defect Control by Applying Steady Magnetic Fields**
David F. Bliss ... 205
7.1 Historical Overview ... 205
7.2 Magnetic Liquid-Encapsulated Growth ... 206
7.3 Magnetic Field Interactions with the Melt ... 209
7.4 Dislocation Density ... 216
7.5 Magnetic Field Effects on Impurity Segregation ... 220
7.6 Optical Characterization of InP:Fe ... 224
7.7 Summary ... 226
References ... 227

8 **Czochralski Silicon Single Crystals for Semiconductor and Solar Cell Applications**
Koichi Kakimoto ... 231
8.1 Silicon Single Crystals for LSIs and Solar Applications ... 232
8.2 Control of Crystal Defects in Czochralski Silicon ... 237
8.3 Growth and Characterization of Silicon Multicrystal for Solar Cell Applications ... 239
8.4 Summary ... 240
References ... 241

9 **Czochralski Growth of Oxide Photorefractive Crystals**
Ernesto Diéguez, Jose Luis Plaza, Mohan D. Aggarwal, Ashok K. Batra ... 245
9.1 Background ... 246
9.2 Crystal Growth ... 246
9.3 Design and Development of Czochralski Growth System ... 247
9.4 Growth of Lithium Niobate Crystals and Its Characteristics ... 252
9.5 Other Oxide Photorefractive Crystals ... 262
9.6 Growth of Sillenite Crystals and Its Characteristics ... 264
9.7 Conclusions ... 273
References ... 273

10 **Bulk Crystal Growth of Ternary III–V Semiconductors**
Partha S. Dutta ... 281
10.1 III–V Ternary Semiconductors ... 282
10.2 Need for Ternary Substrates ... 283
10.3 Criteria for Device-Grade Ternary Substrates ... 284
10.4 Introduction to Bridgman Crystal Growth Techniques ... 286
10.5 Overview of III–V Binary Crystal Growth Technologies ... 292
10.6 Phase Equilibria for Ternary Compounds ... 300
10.7 Alloy Segregation in Ternary Semiconductors ... 302
10.8 Crack Formation in Ternary Crystals ... 304
10.9 Single-Crystalline Ternary Seed Generation Processes ... 308
10.10 Solute Feeding Processes for Homogeneous Alloy Growth ... 311
10.11 Role of Melt–Solid Interface Shapes ... 318
10.12 Conclusion ... 321
References ... 321

11 **Growth and Characterization of Antimony-Based Narrow-Bandgap III–V Semiconductor Crystals for Infrared Detector Applications**
Vijay K. Dixit, Handady L. Bhat ... 327
11.1 Importance of Antimony-Based Semiconductors ... 329
11.2 Phase Diagrams ... 330
11.3 Crystal Structure and Bonding ... 331
11.4 Material Synthesis and Purification ... 333

11.5 Bulk Growth of InSb ... 334
11.6 Structural Properties of InSb, $InAs_xSb_{1-x}$, and $InBi_xSb_{1-x}$ ... 340
11.7 Physical Properties of InSb, $InAs_xSb_{1-x}$, and $InBi_xSb_{1-x}$ ... 346
11.8 Applications ... 357
11.9 Concluding Remarks and Future Outlook ... 359
References ... 360

12 **Crystal Growth of Oxides by Optical Floating Zone Technique**
Hanna A. Dabkowska, Antoni B. Dabkowski ... 367
12.1 Historical Notes ... 367
12.2 Optical Floating Zone Technique – Application for Oxides ... 368
12.3 Optical Floating Zone and Traveling Solvent Crystal Growth Techniques ... 369
12.4 Advantages and Limitations of the Floating Zone Techniques ... 370
12.5 Optical Floating Zone Furnaces ... 371
12.6 Experimental Details of Ceramics and Rod Preparation for OFZT ... 372
12.7 Stable Growth of Congruently and Incongruently Melting Oxides ... 373
12.8 Constitutional Supercooling and Crystallization Front Stability ... 375
12.9 Crystal Growth Termination and Cooling ... 377
12.10 Characterization of Crystals Grown by the OFZ Technique ... 377
12.11 Determination of Defects in Crystals – The Experimental Approach .. 380
12.12 Details of Conditions for Growth of Selected Oxide Single Crystals by OFZ and TSFZ Methods ... 383
12.13 Conclusions ... 386
References ... 386

13 **Laser-Heated Pedestal Growth of Oxide Fibers**
Marcello R.B. Andreeta, Antonio Carlos Hernandes ... 393
13.1 Fiber-Pulling Research ... 394
13.2 The Laser-Heated Pedestal Growth Technique ... 399
13.3 Fundamentals ... 402
13.4 Fiber Growth Aspects ... 409
13.5 Conclusions ... 418
References ... 419

14 **Synthesis of Refractory Materials by Skull Melting Technique**
Vyacheslav V. Osiko, Mikhail A. Borik, Elena E. Lomonova ... 433
14.1 Overview ... 433
14.2 Techniques for Growth of Single Crystals in a Cold Crucible ... 435
14.3 Growth of Single Crystals Based on Zirconium Dioxide ... 443
14.4 Glass Synthesis by Skull Melting in a Cold Crucible ... 465
14.5 Conclusion ... 469
References ... 469

15 **Crystal Growth of Laser Host Fluorides and Oxides**
Hongjun Li, Jun Xu 479
15.1 Crystal Growth of Laser Fluorides and Oxides from Melt 479
15.2 Laser Crystal Defects 487
15.3 Crystal Growth Techniques Characterization 501
References 503

16 **Shaped Crystal Growth**
Vitali A. Tatartchenko 509
16.1 Definitions and Scope of Discussion: SCG by CST 510
16.2 DSC – Basis of SCG by CST 512
16.3 SA and SCG by CZT 517
16.4 SA and SCG by VT 519
16.5 SA and SCG by FZT 522
16.6 TPS Capillary Shaping 522
16.7 TPS Sapphire Growth 539
16.8 TPS Silicon Growth 546
16.9 TPS Metals Growth 551
16.10 TPS Peculiarities 552
References 552

Part C Solution Growth of Crystals

17 **Bulk Single Crystals Grown from Solution on Earth and in Microgravity**
Mohan D. Aggarwal, Ashok K. Batra, Ravindra B. Lal, Benjamin G. Penn, Donald O. Frazier 559
17.1 Crystallization: Nucleation and Growth Kinetics 561
17.2 Low-Temperature Solution Growth 566
17.3 Solution Growth by Temperature Lowering 567
17.4 Triglycine Sulfate Crystal Growth: A Case Study 574
17.5 Solution Growth of Triglycine Sulfate Crystals in Microgravity 582
17.6 Protein Crystal Growth 592
17.7 Concluding Remarks 594
References 594

18 **Hydrothermal Growth of Polyscale Crystals**
Kullaiah Byrappa 599
18.1 History of Hydrothermal Growth of Crystals 603
18.2 Thermodynamic Basis of the Hydrothermal Growth of Crystals 606
18.3 Apparatus Used in the Hydrothermal Growth of Crystals 615
18.4 Hydrothermal Growth of Some Selected Crystals 620
18.5 Hydrothermal Growth of Fine Crystals 634

18.6 Hydrothermal Growth of Nanocrystals 637
18.7 Concluding Remarks 640
18.A Appendix 641
References 646

19 **Hydrothermal and Ammonothermal Growth of ZnO and GaN**
Michael J. Callahan, Qi-Sheng Chen 655
19.1 Overview of Hydrothermal and Ammonothermal Growth of Large Crystals 657
19.2 Requirements for Growth of Large, Low-Defect Crystals 661
19.3 Physical and Mathematical Models 666
19.4 Process Simulations 669
19.5 Hydrothermal Growth of ZnO Crystals 674
19.6 Ammonothermal GaN 681
19.7 Conclusion 685
References 685

20 **Stoichiometry and Domain Structure of KTP-Type Nonlinear Optical Crystals**
Michael Roth 691
20.1 Background 691
20.2 Stoichiometry and Ferroelectric Phase Transitions 697
20.3 Growth-Induced Ferroelectric Domains 703
20.4 Artificial Domain Structures 708
20.5 Nonlinear Optical Crystals 713
References 716

21 **High-Temperature Solution Growth: Application to Laser and Nonlinear Optical Crystals**
Joan J. Carvajal, Maria Cinta Pujol, Francesc Díaz 725
21.1 Basics 726
21.2 High-Temperature Solution Growth 731
21.3 Growth of Bulk Laser and NLO Single Crystals by the TSSG Method 736
21.4 Liquid-Phase Epitaxy: Growth of Epitaxial Films of Laser and NLO Materials 746
References 752

22 **Growth and Characterization of KDP and Its Analogs**
Sheng-Lai Wang, Xun Sun, Xu-Tang Tao 759
22.1 Background 759
22.2 Mechanism and Kinetics of Crystallization 761
22.3 Growth Techniques for Single Crystals 769
22.4 Effect of Growth Conditions on Defects of Crystals 776
22.5 Investigations on Crystal Quality 783
References 789

Part D Crystal Growth from Vapor

23 **Growth and Characterization of Silicon Carbide Crystals**
Govindhan Dhanaraj, Balaji Raghothamachar, Michael Dudley 797
23.1 Silicon Carbide – Background and History 797
23.2 Vapor Growth 799
23.3 High-Temperature Solution Growth 801
23.4 Industrial Bulk Growth by Seed Sublimation 802
23.5 Structural Defects and Their Configurations 805
23.6 Concluding Remarks 816
References 817

24 **AlN Bulk Crystal Growth by Physical Vapor Transport**
Rafael Dalmau, Zlatko Sitar 821
24.1 PVT Crystal Growth 822
24.2 High-Temperature Materials Compatibility 825
24.3 Self-Seeded Growth of AlN Bulk Crystals 827
24.4 Seeded Growth of AlN Bulk Crystals 829
24.5 Characterization of High-Quality Bulk Crystals 832
24.6 Conclusions and Outlook 839
References 839

25 **Growth of Single-Crystal Organic Semiconductors**
Christian Kloc, Theo Siegrist, Jens Pflaum 845
25.1 Basics 845
25.2 Theory of Nucleation and Crystal Growth 847
25.3 Organic Materials of Interest for Semiconducting Single Crystals 848
25.4 Pregrowth Purification 850
25.5 Crystal Growth 854
25.6 Quality of Organic Semiconducting Single Crystals 862
25.7 Organic Single-Crystalline Field-Effect Transistors 863
25.8 Conclusions 864
References 865

26 **Growth of III-Nitrides with Halide Vapor Phase Epitaxy (HVPE)**
Carl Hemmingsson, Bo Monemar, Yoshinao Kumagai, Akinori Koukitu 869
26.1 Growth Chemistry and Thermodynamics 869
26.2 HVPE Growth Equipment 872
26.3 Substrates and Templates for Bulk GaN Growth 875
26.4 Substrate Removal Techniques 879
26.5 Doping Techniques for GaN in HVPE 882
26.6 Defect Densities, Dislocations, and Residual Impurities 883
26.7 Some Important Properties of HVPE-Grown Bulk GaN Material 887
26.8 Growth of AlN by HVPE: Some Preliminary Results 888
26.9 Growth of InN by HVPE: Some Preliminary Results 890
References 891

27 **Growth of Semiconductor Single Crystals from Vapor Phase**
Ramasamy Dhanasekaran ... 897
27.1 Classifications of Vapor Growth ... 899
27.2 Chemical Vapor Transport – Transport Kinetics ... 901
27.3 Thermodynamic Considerations ... 905
27.4 Growth of II–VI Compound Semiconductors by CVT ... 912
27.5 Growth of Nanomaterial from Vapor Phase ... 916
27.6 Growth of I–III–VI_2 Compounds ... 917
27.7 Growth of GaN by VPE ... 925
27.8 Conclusion ... 929
References ... 930

Part E Epitaxial Growth and Thin Films

28 **Epitaxial Growth of Silicon Carbide by Chemical Vapor Deposition**
Ishwara B. Bhat ... 939
28.1 Polytypes of Silicon Carbide ... 941
28.2 Defects in SiC ... 942
28.3 Epitaxial Growth of Silicon Carbide ... 944
28.4 Epitaxial Growth on Patterned Substrates ... 952
28.5 Conclusions ... 961
References ... 961

29 **Liquid-Phase Electroepitaxy of Semiconductors**
Sadik Dost ... 967
29.1 Background ... 967
29.2 Early Theoretical and Modeling Studies ... 971
29.3 Two-Dimensional Continuum Models ... 977
29.4 LPEE Growth Under a Stationary Magnetic Field ... 978
29.5 Three-Dimensional Simulations ... 981
29.6 High Growth Rates in LPEE: Electromagnetic Mobility ... 992
References ... 996

30 **Epitaxial Lateral Overgrowth of Semiconductors**
Zbigniew R. Zytkiewicz ... 999
30.1 Overview ... 1000
30.2 Mechanism of Epitaxial Lateral Overgrowth from the Liquid Phase ... 1002
30.3 Dislocations in ELO Layers ... 1011
30.4 Strain in ELO Layers ... 1016
30.5 Recent Progress in Lateral Overgrowth of Semiconductor Structures ... 1026
30.6 Concluding Remarks ... 1034
References ... 1035

31 **Liquid-Phase Epitaxy of Advanced Materials**
Christine F. Klemenz Rivenbark 1041
31.1 Historical Development of LPE 1042
31.2 Fundamentals of LPE and Solution Growth 1042
31.3 Requirements for Liquid-Phase Epitaxy 1044
31.4 Developing New Materials: On the Choice of the Epitaxial Deposition Method 1044
31.5 LPE of High-Temperature Superconductors 1046
31.6 LPE of Calcium Gallium Germanates 1055
31.7 Liquid-Phase Epitaxy of Nitrides 1059
31.8 Conclusions 1063
References 1064

32 **Molecular-Beam Epitaxial Growth of HgCdTe**
James W. Garland, Sivalingam Sivananthan 1069
32.1 Overview 1070
32.2 Theory of MBE Growth 1073
32.3 Substrate Materials 1076
32.4 Design of the Growth Hardware 1088
32.5 In situ Characterization Tools for Monitoring and Controlling the Growth 1090
32.6 Nucleation and Growth Procedure 1101
32.7 Dopants and Dopant Activation 1104
32.8 Properties of HgCdTe Epilayers Grown by MBE 1107
32.9 HgTe/CdTe Superlattices 1112
32.10 Architectures of Advanced IR Detectors 1115
32.11 IR Focal-Plane Arrays (FPAs) 1118
32.12 Conclusions 1119
References 1121

33 **Metalorganic Vapor-Phase Epitaxy of Diluted Nitrides and Arsenide Quantum Dots**
Udo W. Pohl 1133
33.1 Principle of MOVPE 1133
33.2 Diluted Nitride InGaAsN Quantum Wells 1137
33.3 InAs/GaAs Quantum Dots 1142
33.4 Concluding Remarks 1148
References 1148

34 **Formation of SiGe Heterostructures and Their Properties**
Yasuhiro Shiraki, Akira Sakai 1153
34.1 Background 1153
34.2 Band Structures of Si/Ge Heterostructures 1154
34.3 Growth Technologies 1156
34.4 Surface Segregation 1157
34.5 Critical Thickness 1161
34.6 Mechanism of Strain Relaxation 1163

34.7 Formation of Relaxed SiGe Layers ... 1165
34.8 Formation of Quantum Wells, Superlattices, and Quantum Wires ... 1173
34.9 Dot Formation ... 1177
34.10 Concluding Remarks and Future Prospects ... 1184
References ... 1184

35 **Plasma Energetics in Pulsed Laser and Pulsed Electron Deposition**
Mikhail D. Strikovski, Jeonggoo Kim, Solomon H. Kolagani ... 1193
35.1 Energetic Condensation in Thin Film Deposition ... 1193
35.2 PLD and PED Techniques ... 1194
35.3 Transformations of Atomic Energy in PLD and PED ... 1195
35.4 Optimization of Plasma Flux for Film Growth ... 1204
35.5 Conclusions ... 1208
References ... 1209

Part F Modeling in Crystal Growth and Defects

36 **Convection and Control in Melt Growth of Bulk Crystals**
Chung-Wen Lan ... 1215
36.1 Physical Laws for Transport Processes ... 1217
36.2 Flow Structures in the Melt ... 1219
36.3 Flow Control by External Forces ... 1228
36.4 Outlook ... 1238
References ... 1238

37 **Vapor Growth of III Nitrides**
Dang Cai, Lili Zheng, Hui Zhang ... 1243
37.1 Overview of Vapor Growth of III Nitrides ... 1244
37.2 Mathematical Models for AlN/GaN Vapor Deposition ... 1248
37.3 Characteristics of AlN/GaN Vapor Deposition ... 1251
37.4 Modeling of GaN IVPE Growth – A Case Study ... 1258
37.5 Surface Evolution of GaN/AlN Film Growth from Vapor ... 1274
37.6 Concluding Remarks ... 1275
References ... 1276

38 **Continuum-Scale Quantitative Defect Dynamics in Growing Czochralski Silicon Crystals**
Milind S. Kulkarni ... 1281
38.1 The Discovery of Microdefects ... 1283
38.2 Defect Dynamics in the Absence of Impurities ... 1284
38.3 Czochralski Defect Dynamics in the Presence of Oxygen ... 1304
38.4 Czochralski Defect Dynamics in the Presence of Nitrogen ... 1313
38.5 The Lateral Incorporation of Vacancies in Czochralski Silicon Crystals 1321
38.6 Conclusions ... 1328
References ... 1332

39 **Models for Stress and Dislocation Generation in Melt Based Compound Crystal Growth**
Vishwanath (Vish) Prasad, Srinivas Pendurti 1335
39.1 Overview 1335
39.2 Crystal Growth Processes 1336
39.3 Dislocations in Semiconductors Materials 1337
39.4 Models for Dislocation Generation 1339
39.5 Diamond Structure of the Crystal 1343
39.6 Deformation Behavior of Semiconductors 1346
39.7 Application of the Haasen Model to Crystal Growth 1350
39.8 An Alternative Model 1351
39.9 Model Summary and Numerical Implementation 1360
39.10 Numerical Results 1362
39.11 Summary 1374
References 1375

40 **Mass and Heat Transport in BS and EFG Systems**
Thomas F. George, Stefan Balint, Liliana Braescu 1379
40.1 Model-Based Prediction of the Impurity Distribution – Vertical BS System 1380
40.2 Model-Based Prediction of the Impurity Distribution – EFG System 1389
References 1400

Part G Defects Characterization and Techniques

41 **Crystalline Layer Structures with X-Ray Diffractometry**
Paul F. Fewster 1405
41.1 X-Ray Diffractometry 1406
41.2 Basic Direct X-Ray Diffraction Analysis from Layered Structures 1407
41.3 Instrumental and Theoretical Considerations 1412
41.4 Examples of Analysis from Low to High Complexity 1413
41.5 Rapid Analysis 1419
41.6 Wafer Micromapping 1420
41.7 The Future 1421
References 1422

42 **X-Ray Topography Techniques for Defect Characterization of Crystals**
Balaji Raghothamachar, Michael Dudley, Govindhan Dhanaraj 1425
42.1 Basic Principles of X-Ray Topography 1426
42.2 Historical Development of the X-Ray Topography Technique 1428
42.3 X-Ray Topography Techniques and Geometry 1430
42.4 Theoretical Background for X-Ray Topography 1435
42.5 Mechanisms for Contrast on X-Ray Topographs 1440

42.6 Analysis of Defects on X-Ray Topographs 1445
42.7 Current Application Status and Development 1449
References 1450

43 **Defect-Selective Etching of Semiconductors**
Jan L. Weyher, John J. Kelly 1453
43.1 Wet Etching of Semiconductors: Mechanisms 1454
43.2 Wet Etching of Semiconductors: Morphology and Defect Selectivity .. 1459
43.3 Defect-Selective Etching Methods 1461
References 1473

44 **Transmission Electron Microscopy Characterization of Crystals**
Jie Bai, Shixin Wang, Lu-Min Wang, Michael Dudley 1477
44.1 Theoretical Basis of TEM Characterization of Defects 1477
44.2 Selected Examples of Application of TEM to Semiconductor Systems . 1493
44.3 Concluding Remarks: Current Application Status and Development .. 1514
References 1515

45 **Electron Paramagnetic Resonance Characterization of Point Defects**
Mary E. Zvanut 1521
45.1 Electronic Paramagnetic Resonance 1522
45.2 EPR Analysis 1524
45.3 Scope of EPR Technique 1534
45.4 Supplementary Instrumentation and Supportive Techniques 1538
45.5 Summary and Final Thoughts 1545
References 1546

46 **Defect Characterization in Semiconductors with Positron Annihilation Spectroscopy**
Filip Tuomisto 1551
46.1 Positron Annihilation Spectroscopy 1552
46.2 Identification of Point Defects and Their Charge States 1560
46.3 Defects, Doping, and Electrical Compensation 1565
46.4 Point Defects and Growth Conditions 1569
46.5 Summary 1576
References 1576

Part H Special Topics in Crystal Growth

47 **Protein Crystal Growth Methods**
Andrea E. Gutiérrez-Quezada, Roberto Arreguín-Espinosa, Abel Moreno 1583
47.1 Properties of Biomacromolecular Solutions 1584
47.2 Transport Phenomena and Crystallization 1587
47.3 Classic Methods of Crystal Growth 1587
47.4 Protein Crystallization by Diffusion-Controlled Methods 1588

47.5 New Trends in Crystal Growth (Crystal Quality Enhancement) 1591
47.6 2-D Characterization via Atomic Force Microscopy (Case Study)......... 1595
47.7 3-D Characterization via X-Ray Diffraction and Related Methods 1598
References 1599

48 **Crystallization from Gels**
S. Narayana Kalkura, Subramanian Natarajan 1607
48.1 Gel Growth in Crystal Deposition Diseases 1608
48.2 Experimental Methods 1609
48.3 Pattern Formation in Gel Systems 1610
48.4 Crystals Grown Using Gel Technique 1611
48.5 Application in Crystal Deposition Diseases 1614
48.6 Crystal-Deposition-Related Diseases 1616
48.7 Calcium Oxalate 1617
48.8 Calcium Phosphates 1619
48.9 Hydroxyapatite (HAP) 1620
48.10 Dicalcium Phosphate Dihydrate (DCPD) 1620
48.11 Calcium Sulfate 1623
48.12 Uric Acid and Monosodium Urate Monohydrate 1623
48.13 L-Cystine 1624
48.14 L-Tyrosine, Hippuric Acid, and Ciprofloxacin 1625
48.15 Atherosclerosis and Gallstones 1625
48.16 Crystallization of Hormones: Progesterone and Testosterone 1628
48.17 Pancreatitis 1628
48.18 Conclusions 1629
References 1630

49 **Crystal Growth and Ion Exchange in Titanium Silicates**
Aaron J. Celestian, John B. Parise, Abraham Clearfield 1637
49.1 X-Ray Methods 1637
49.2 Equipment for Time-Resolved Experiments 1642
49.3 Detectors 1642
49.4 Software 1644
49.5 Types of In Situ Cells 1645
49.6 In-Situ Studies of Titanium Silicates (Na-TS) with Sitinakite Topology 1649
49.7 Discussion of In Situ Studies 1658
49.8 Summary 1660
References 1660

50 **Single-Crystal Scintillation Materials**
Martin Nikl, Anna Vedda, Valentin V. Laguta 1663
50.1 Background 1663
50.2 Scintillation Materials 1670
50.3 Future Prospects 1689
50.4 Conclusions 1691
References 1691

51 **Silicon Solar Cells: Materials, Devices, and Manufacturing**
Mohan Narayanan, Ted Ciszek 1701
51.1 Silicon Photovoltaics 1701
51.2 Crystal Growth Technologies for Silicon Photovoltaics 1704
51.3 Cell Fabrication Technologies 1711
51.4 Summary and Discussion 1715
References 1716

52 **Wafer Manufacturing and Slicing Using Wiresaw**
Imin Kao, Chunhui Chung, Roosevelt Moreno Rodriguez 1719
52.1 From Crystal Ingots to Prime Wafers 1721
52.2 Slicing: The First Postgrowth Process in Wafer Manufacturing 1726
52.3 Modern Wiresaw in Wafer Slicing 1730
52.4 Conclusions and Further Reading 1733
References 1733

Acknowledgements 1737
About the Authors 1741
Detailed Contents 1759
Subject Index 1791

List of Abbreviations

μ-PD micro-pulling-down
1S-ELO one-step ELO structure
2-D two-dimensional
2-DNG two-dimensional nucleation growth
2S-ELO double layer ELO
3-D three-dimensional
4T quaterthiophene
6T sexithienyl
8MR eight-membered ring
8T hexathiophene

A

a-Si amorphous silicon
A/D analogue-to-digital
AA additional absorption
AANP 2-adamantylamino-5-nitropyridine
AAS atomic absorption spectroscopy
AB Abrahams and Burocchi
ABES absorption-edge spectroscopy
AC alternate current
ACC annular capillary channel
ACRT accelerated crucible rotation technique
ADC analog-to-digital converter
ADC automatic diameter control
ADF annular dark field
ADP ammonium dihydrogen phosphate
AES Auger electron spectroscopy
AFM atomic force microscopy
ALE arbitrary Lagrangian Eulerian
ALE atomic layer epitaxy
ALUM aluminum potassium sulfate
ANN artificial neural network
AO acoustooptic
AP atmospheric pressure
APB antiphase boundaries
APCF advanced protein crystallization facility
APD avalanche photodiode
APPLN aperiodic poled LN
APS Advanced Photon Source
AR antireflection
AR aspect ratio
ART aspect ratio trapping
ATGSP alanine doped triglycine sulfo-phosphate
AVT angular vibration technique

B

BA Born approximation
BAC band anticrossing
BBO BaB_2O_4
BCF Burton–Cabrera–Frank
BCT $Ba_{0.77}Ca_{0.23}TiO_3$
BCTi $Ba_{1-x}Ca_xTiO_3$
BE bound exciton
BF bright field
BFDH Bravais–Friedel–Donnay–Harker
BGO $Bi_{12}GeO_{20}$
BIBO BiB_3O_6
BLIP background-limited performance
BMO $Bi_{12}MO_{20}$
BN boron nitride
BOE buffered oxide etch
BPD basal-plane dislocation
BPS Burton–Prim–Slichter
BPT bipolar transistor
BS Bridgman–Stockbarger
BSCCO Bi−Sr−Ca−Cu−O
BSF bounding stacking fault
BSO $Bi_{20}SiO_{20}$
BTO $Bi_{12}TiO_{20}$
BU building unit
BaREF barium rare-earth fluoride
BiSCCO $Bi_2Sr_2CaCu_2O_n$

C

C–V capacitance–voltage
CALPHAD calculation of phase diagram
CBED convergent-beam electron diffraction
CC cold crucible
CCC central capillary channel
CCD charge-coupled device
CCVT contactless chemical vapor transport
CD convection diffusion
CE counterelectrode
CFD computational fluid dynamics
CFD cumulative failure distribution
CFMO Ca_2FeMoO_6
CFS continuous filtration system
CGG calcium gallium germanate
CIS copper indium diselenide
CL cathode-ray luminescence
CL cathodoluminescence
CMM coordinate measuring machine
CMO $CaMoO_4$
CMOS complementary metal–oxide–semiconductor
CMP chemical–mechanical polishing
CMP chemomechanical polishing

COD	calcium oxalate dihydrate
COM	calcium oxalate-monohydrate
COP	crystal-originated particle
CP	critical point
CPU	central processing unit
CRSS	critical-resolved shear stress
CSMO	$Ca_{1-x}Sr_xMoO_3$
CST	capillary shaping technique
CST	crystalline silico titanate
CT	computer tomography
CTA	$CsTiOAsO_4$
CTE	coefficient of thermal expansion
CTF	contrast transfer function
CTR	crystal truncation rod
CV	Cabrera–Vermilyea
CVD	chemical vapor deposition
CVT	chemical vapor transport
CW	continuous wave
CZ	Czochralski
CZT	Czochralski technique

D

D/A	digital to analog
DBR	distributed Bragg reflector
DC	direct current
DCAM	diffusion-controlled crystallization apparatus for microgravity
DCCZ	double crucible CZ
DCPD	dicalcium-phosphate dihydrate
DCT	dichlorotetracene
DD	dislocation dynamics
DESY	Deutsches Elektronen Synchrotron
DF	dark field
DFT	density function theory
DFW	defect free width
DGS	diglycine sulfate
DI	deionized
DIA	diamond growth
DIC	differential interference contrast
DICM	differential interference contrast microscopy
DKDP	deuterated potassium dihydrogen phosphate
DLATGS	deuterated L-alanine-doped triglycine sulfate
DLTS	deep-level transient spectroscopy
DMS	discharge mass spectroscopy
DNA	deoxyribonucleic acid
DOE	Department of Energy
DOS	density of states
DPH-BDS	2,6-diphenylbenzo[1,2-*b*:4,5-*b*']diselenophene
DPPH	2,2-diphenyl-1-picrylhydrazyl
DRS	dynamic reflectance spectroscopy
DS	directional solidification
DSC	differential scanning calorimetry
DSE	defect-selective etching
DSL	diluted Sirtl with light
DTA	differential thermal analysis
DTGS	deuterated triglycine sulfate
DVD	digital versatile disk
DWBA	distorted-wave Born approximation
DWELL	dot-in-a-well

E

EADM	extended atomic distance mismatch
EALFZ	electrical-assisted laser floating zone
EB	electron beam
EBIC	electron-beam-induced current
ECE	end chain energy
ECR	electron cyclotron resonance
EDAX	energy-dispersive x-ray analysis
EDMR	electrically detected magnetic resonance
EDS	energy-dispersive x-ray spectroscopy
EDT	ethylene dithiotetrathiafulvalene
EDTA	ethylene diamine tetraacetic acid
EELS	electron energy-loss spectroscopy
EFG	edge-defined film-fed growth
EFTEM	energy-filtered transmission electron microscopy
ELNES	energy-loss near-edge structure
ELO	epitaxial lateral overgrowth
EM	electromagnetic
EMA	effective medium theory
EMC	electromagnetic casting
EMCZ	electromagnetic Czochralski
EMF	electromotive force
ENDOR	electron nuclear double resonance
EO	electrooptic
EP	EaglePicher
EPD	etch pit density
EPMA	electron microprobe analysis
EPR	electron paramagnetic resonance
erfc	error function
ES	equilibrium shape
ESP	edge-supported pulling
ESR	electron spin resonance
EVA	ethyl vinyl acetate

F

F	flat
FAM	free abrasive machining
FAP	$Ca_5(PO_4)_3F$
FCA	free carrier absorption
fcc	face-centered cubic
FEC	full encapsulation Czochralski

FEM finite element method
FES fluid experiment system
FET field-effect transistor
FFT fast Fourier transform
FIB focused ion beam
FOM figure of merit
FPA focal-plane array
FPE Fokker–Planck equation
FSLI femtosecond laser irradiation
FT flux technique
FTIR Fourier-transform infrared
FWHM full width at half-maximum
FZ floating zone
FZT floating zone technique

G

GAME gel acupuncture method
GDMS glow-discharge mass spectrometry
GE General Electric
GGG gadolinium gallium garnet
GNB geometrically necessary boundary
GPIB general purpose interface bus
GPMD geometric partial misfit dislocation
GRI growth interruption
GRIIRA green-radiation-induced infrared absorption
GS growth sector
GSAS general structure analysis software
GSGG $Gd_3Sc_2Ga_3O_{12}$
GSMBE gas-source molecular-beam epitaxy
GSO Gd_2SiO_5
GU growth unit

H

HA hydroxyapatite
HAADF high-angle annular dark field
HAADF-STEM high-angle annular dark field in scanning transmission electron microscope
HAP hydroxyapatite
HB horizontal Bridgman
HBM Hottinger Baldwin Messtechnik GmbH
HBT heterostructure bipolar transistor
HBT horizontal Bridgman technique
HDPCG high-density protein crystal growth
HE high energy
HEM heat-exchanger method
HEMT high-electron-mobility transistor
HF hydrofluoric acid
HGF horizontal gradient freezing
HH heavy-hole
HH-PCAM handheld protein crystallization apparatus for microgravity
HIV human immunodeficiency virus
HIV-AIDS human immunodeficiency virus–acquired immunodeficiency syndrome
HK high potassium content
HLA half-loop array
HLW high-level waste
HMDS hexamethyldisilane
HMT hexamethylene tetramine
HNP high nitrogen pressure
HOE holographic optical element
HOLZ higher-order Laue zone
HOMO highest occupied molecular orbital
HOPG highly oriented pyrolytic graphite
HOT high operating temperature
HP Hartman–Perdok
HPAT high-pressure ammonothermal technique
HPHT high-pressure high-temperature
HRTEM high-resolution transmission electron microscopy
HRXRD high-resolution x-ray diffraction
HSXPD hemispherically scanned x-ray photoelectron diffraction
HT hydrothermal
HTS high-temperature solution
HTSC high-temperature superconductor
HVPE halide vapor-phase epitaxy
HVPE hydride vapor-phase epitaxy
HWC hot-wall Czochralski
HZM horizontal ZM

I

IBAD ion-beam-assisted deposition
IBE ion beam etching
IC integrated circuit
IC ion chamber
ICF inertial confinement fusion
ID inner diameter
ID inversion domain
IDB incidental dislocation boundary
IDB inversion domain boundary
IF identification flat
IG inert gas
IK intermediate potassium content
ILHPG indirect laser-heated pedestal growth
IML-1 International Microgravity Laboratory
IMPATT impact ionization avalanche transit-time
IP image plate
IPA isopropyl alcohol
IR infrared
IRFPA infrared focal plane array
IS interfacial structure
ISS ion-scattering spectroscopy
ITO indium-tin oxide
ITTFA iterative target transform factor analysis
IVPE iodine vapor-phase epitaxy

J

JDS	joint density of states
JFET	junction FET

K

K	kinked
KAP	potassium hydrogen phthalate
KDP	potassium dihydrogen phosphate
KGW	$KY(WO_4)_2$
KGdP	$KGd(PO_3)_4$
KLYF	$KLiYF_5$
KM	Kubota–Mullin
KMC	kinetic Monte Carlo
KN	$KNbO_3$
KNP	$KNd(PO_3)_4$
KPZ	Kardar–Parisi–Zhang
KREW	$KRE(WO_4)_2$
KTA	potassium titanyl arsenate
KTN	potassium niobium tantalate
KTP	potassium titanyl phosphate
KTa	$KTaO_3$
KTaN	$KTa_{1-x}Nb_xO_3$
KYF	KYF_4
KYW	$KY(WO_4)_2$

L

LACBED	large-angle convergent-beam diffraction
LAFB	L-arginine tetrafluoroborate
LAGB	low-angle grain boundary
LAO	$LiAlO_2$
LAP	L-arginine phosphate
LBIC	light-beam induced current
LBIV	light-beam induced voltage
LBO	LiB_3O_5
LBO	$LiBO_3$
LBS	laser-beam scanning
LBSM	laser-beam scanning microscope
LBT	laser-beam tomography
LCD	liquid-crystal display
LD	laser diode
LDT	laser-induced damage threshold
LEC	liquid encapsulation Czochralski
LED	light-emitting diode
LEEBI	low-energy electron-beam irradiation
LEM	laser emission microanalysis
LEO	lateral epitaxial overgrowth
LES	large-eddy simulation
LG	$LiGaO_2$
LGN	$La_3Ga_{5.5}Nb_{0.5}O_{14}$
LGO	$LaGaO_3$
LGS	$La_3Ga_5SiO_{14}$
LGT	$La_3Ga_{5.5}Ta_{0.5}O_{14}$
LH	light hole
LHFB	L-histidine tetrafluoroborate
LHPG	laser-heated pedestal growth
LID	laser-induced damage
LK	low potassium content
LLNL	Lawrence Livermore National Laboratory
LLO	laser lift-off
LLW	low-level waste
LN	$LiNbO_3$
LP	low pressure
LPD	liquid-phase diffusion
LPE	liquid-phase epitaxy
LPEE	liquid-phase electroepitaxy
LPS	$Lu_2Si_2O_7$
LSO	Lu_2SiO_5
LST	laser scattering tomography
LST	local shaping technique
LT	low-temperature
LTa	$LiTaO_3$
LUMO	lowest unoccupied molecular orbital
LVM	local vibrational mode
LWIR	long-wavelength IR
LY	light yield
LiCAF	$LiCaAlF_6$
LiSAF	lithium strontium aluminum fluoride

M

M–S	melt–solid
MAP	magnesium ammonium phosphate
MASTRAPP	multizone adaptive scheme for transport and phase change processes
MBE	molecular-beam epitaxy
MBI	multiple-beam interferometry
MC	multicrystalline
MCD	magnetic circular dichroism
MCT	HgCdTe
MCZ	magnetic Czochralski
MD	misfit dislocation
MD	molecular dynamics
ME	melt epitaxy
ME	microelectronics
MEMS	microelectromechanical system
MESFET	metal-semiconductor field effect transistor
MHP	magnesium hydrogen phosphate-trihydrate
MI	morphological importance
MIT	Massachusetts Institute of Technology
ML	monolayer
MLEC	magnetic liquid-encapsulated Czochralski

MLEK magnetically stabilized liquid-encapsulated Kyropoulos
MMIC monolithic microwave integrated circuit
MNA 2-methyl-4-nitroaniline
MNSM modified nonstationary model
MOCVD metalorganic chemical vapor deposition
MOCVD molecular chemical vapor deposition
MODFET modulation-doped field-effect transistor
MOMBE metalorganic MBE
MOS metal–oxide–semiconductor
MOSFET metal–oxide–semiconductor field-effect transistor
MOVPE metalorganic vapor-phase epitaxy
mp melting point
MPMS mold-pushing melt-supplying
MQSSM modified quasi-steady-state model
MQW multiple quantum well
MR melt replenishment
MRAM magnetoresistive random-access memory
MRM melt replenishment model
MSUM monosodium urate monohydrate
MTDATA metallurgical thermochemistry database
MTS methyltrichlorosilane
MUX multiplexor
MWIR mid-wavelength infrared
MWRM melt without replenishment model
MXRF micro-area x-ray fluorescence

N

N nucleus
N nutrient
NASA National Aeronautics and Space Administration
NBE near-band-edge
NBE near-bandgap emission
NCPM noncritically phase matched
NCS neighboring confinement structure
NGO $NdGaO_3$
NIF National Ignition Facility
NIR near-infrared
NIST National Institute of Standards and Technology
NLO nonlinear optic
NMR nuclear magnetic resonance
NP no-phonon
NPL National Physical Laboratory
NREL National Renewable Energy Laboratory
NS Navier–Stokes
NSF National Science Foundation
nSLN nearly stoichiometric lithium niobate
NSLS National Synchrotron Light Source
NSM nonstationary model
NTRS National Technology Roadmap for Semiconductors
NdBCO $NdBa_2Cu_3O_{7-x}$

O

OCP octacalcium phosphate
ODE ordinary differential equation
ODLN opposite domain LN
ODMR optically detected magnetic resonance
OEIC optoelectronic integrated circuit
OF orientation flat
OFZ optical floating zone
OLED organic light-emitting diode
OMVPE organometallic vapor-phase epitaxy
OPO optical parametric oscillation
OSF oxidation-induced stacking fault

P

PAMBE photo-assisted MBE
PB proportional band
PBC periodic bond chain
pBN pyrolytic boron nitride
PC photoconductivity
PCAM protein crystallization apparatus for microgravity
PCF primary crystallization field
PCF protein crystal growth facility
PCM phase-contrast microscopy
PD Peltier interface demarcation
PD photodiode
PDE partial differential equation
PDP programmed data processor
PDS periodic domain structure
PE pendeo-epitaxy
PEBS pulsed electron beam source
PEC polyimide environmental cell
PECVD plasma-enhanced chemical vapor deposition
PED pulsed electron deposition
PEO polyethylene oxide
PET positron emission tomography
PID proportional–integral–differential
PIN positive intrinsic negative diode
PL photoluminescence
PLD pulsed laser deposition
PMNT $Pb(Mg, Nb)_{1-x}Ti_xO_3$
PPKTP periodically poled KTP
PPLN periodic poled LN
PPLN periodic poling lithium niobate
ppy polypyrrole
PR photorefractive
PSD position-sensitive detector
PSF prismatic stacking fault

PSI phase-shifting interferometry
PSM phase-shifting microscopy
PSP pancreatic stone protein
PSSM pseudo-steady-state model
PSZ partly stabilized zirconium dioxide
PT pressure–temperature
PV photovoltaic
PVA polyvinyl alcohol
PVD physical vapor deposition
PVE photovoltaic efficiency
PVT physical vapor transport
PWO $PbWO_4$
PZNT $Pb(Zn, Nb)_{1-x}Ti_xO_3$
PZT lead zirconium titanate

Q

QD quantum dot
QDT quantum dielectric theory
QE quantum efficiency
QPM quasi-phase-matched
QPMSHG quasi-phase-matched second-harmonic generation
QSSM quasi-steady-state model
QW quantum well
QWIP quantum-well infrared photodetector

R

RAE rotating analyzer ellipsometer
RBM rotatory Bridgman method
RC reverse current
RCE rotating compensator ellipsometer
RE rare earth
RE reference electrode
REDG recombination enhanced dislocation glide
RELF rare-earth lithium fluoride
RF radiofrequency
RGS ribbon growth on substrate
RHEED reflection high-energy electron diffraction
RI refractive index
RIE reactive ion etching
RMS root-mean-square
RNA ribonucleic acid
ROIC readout integrated circuit
RP reduced pressure
RPI Rensselaer Polytechnic Institute
RSM reciprocal space map
RSS resolved shear stress
RT room temperature
RTA $RbTiOAsO_4$
RTA rapid thermal annealing
RTCVD rapid-thermal chemical vapor deposition
RTP $RbTiOPO_4$
RTPL room-temperature photoluminescence
RTR ribbon-to-ribbon
RTV room temperature vulcanizing
R&D research and development

S

S stepped
SAD selected area diffraction
SAM scanning Auger microprobe
SAW surface acoustical wave
SBN strontium barium niobate
SC slow cooling
SCBG slow-cooling bottom growth
SCC source-current-controlled
SCF single-crystal fiber
SCF supercritical fluid technology
SCN succinonitrile
SCW supercritical water
SD screw dislocation
SE spectroscopic ellipsometry
SECeRTS small environmental cell for real-time studies
SEG selective epitaxial growth
SEM scanning electron microscope
SEM scanning electron microscopy
SEMATECH Semiconductor Manufacturing Technology
SF stacking fault
SFM scanning force microscopy
SGOI SiGe-on-insulator
SH second harmonic
SHG second-harmonic generation
SHM submerged heater method
SI semi-insulating
SIA Semiconductor Industry Association
SIMS secondary-ion mass spectrometry
SIOM Shanghai Institute of Optics and Fine Mechanics
SL superlattice
SL-3 Spacelab-3
SLI solid–liquid interface
SLN stoichiometric LN
SM skull melting
SMB stacking mismatch boundary
SMG surfactant-mediated growth
SMT surface-mount technology
SNR signal-to-noise ratio
SNT sodium nonatitanate
SOI silicon-on-insulator
SP sputtering
sPC scanning photocurrent
SPC Scientific Production Company
SPC statistical process control
SR spreading resistance
SRH Shockley–Read–Hall
SRL strain-reducing layer
SRS stimulated Raman scattering

SRXRD	spatially resolved XRD
SS	solution-stirring
SSL	solid-state laser
SSM	sublimation sandwich method
ST	synchrotron topography
STC	standard testing condition
STE	self-trapped exciton
STEM	scanning transmission electron microscopy
STM	scanning tunneling microscopy
STOS	sodium titanium oxide silicate
STP	stationary temperature profile
STS	space transportation system
SWBXT	synchrotron white beam x-ray topography
SWIR	short-wavelength IR
SXRT	synchrotron x-ray topography

T

TCE	trichloroethylene
TCNQ	tetracyanoquinodimethane
TCO	thin-film conducting oxide
TCP	tricalcium phosphate
TD	Tokyo Denpa
TD	threading dislocation
TDD	threading dislocation density
TDH	temperature-dependent Hall
TDMA	tridiagonal matrix algorithm
TED	threading edge dislocation
TEM	transmission electron microscopy
TFT-LCD	thin-film transistor liquid-crystal display
TGS	triglycine sulfate
TGT	temperature gradient technique
TGW	Thomson–Gibbs–Wulff
TGZM	temperature gradient zone melting
THM	traveling heater method
TMCZ	transverse magnetic-field-applied Czochralski
TMOS	tetramethoxysilane
TO	transverse optic
TPB	three-phase boundary
TPRE	twin-plane reentrant-edge effect
TPS	technique of pulling from shaper
TQM	total quality management
TRAPATT	trapped plasma avalanche-triggered transit
TRM	temperature-reduction method
TS	titanium silicate
TSC	thermally stimulated conductivity
TSD	threading screw dislocation
TSET	two shaping elements technique
TSFZ	traveling solvent floating zone
TSL	thermally stimulated luminescence
TSSG	top-seeded solution growth
TSSM	Tatarchenko steady-state model
TSZ	traveling solvent zone
TTV	total thickness variation
TV	television
TVM	three-vessel solution circulating method
TVTP	time-varying temperature profile
TWF	transmitted wavefront
TZM	titanium zirconium molybdenum
TZP	tetragonal phase

U

UC	universal compliant
UDLM	uniform-diffusion-layer model
UHPHT	ultrahigh-pressure high-temperature
UHV	ultrahigh-vacuum
ULSI	ultralarge-scale integrated circuit
UV	ultraviolet
UV-vis	ultraviolet–visible
UVB	ultraviolet B

V

VAS	void-assisted separation
VB	valence band
VB	vertical Bridgman
VBT	vertical Bridgman technique
VCA	virtual-crystal approximation
VCSEL	vertical-cavity surface-emitting laser
VCZ	vapor pressure controlled Czochralski
VDA	vapor diffusion apparatus
VGF	vertical gradient freeze
VLS	vapor–liquid–solid
VLSI	very large-scale integrated circuit
VLWIR	very long-wavelength infrared
VMCZ	vertical magnetic-field-applied Czochralski
VP	vapor phase
VPE	vapor-phase epitaxy
VST	variable shaping technique
VT	Verneuil technique
VTGT	vertical temperature gradient technique
VUV	vacuum ultraviolet

W

WBDF	weak-beam dark-field
WE	working electrode

X

XP	x-ray photoemission
XPS	x-ray photoelectron spectroscopy
XPS	x-ray photoemission spectroscopy
XRD	x-ray diffraction
XRPD	x-ray powder diffraction
XRT	x-ray topography

Y

YAB	$YAl_3(BO_3)_4$
YAG	yttrium aluminum garnet
YAP	yttrium aluminum perovskite
YBCO	$YBa_2Cu_3O_{7-x}$
YIG	yttrium iron garnet
YL	yellow luminescence
YLF	$LiYF_4$
YOF	yttrium oxyfluoride
YPS	$(Y_2)Si_2O_7$
YSO	Y_2SiO_5

Z

ZA	Al_2O_3-$ZrO_2(Y_2O_3)$
ZLP	zero-loss peak
ZM	zone-melting
ZNT	ZN-Technologies
ZOLZ	zero-order Laue zone

Part A

Fundame

Part A Fundamentals of Crystal Growth and Defect Formation

1 Crystal Growth Techniques and Characterization: An Overview
Govindhan Dhanaraj, Nashua, USA
Kullaiah Byrappa, Mysore, India
Vishwanath (Vish) Prasad, Denton, USA
Michael Dudley, Stony Brook, USA

2 Nucleation at Surfaces
Ivan V. Markov, Sofia, Bulgaria

3 Morphology of Crystals Grown from Solutions
Francesco Abbona, Torino, Italy
Dino Aquilano, Torino, Italy

4 Generation and Propagation of Defects During Crystal Growth
Helmut Klapper, Aachen, Germany

5 Single Crystals Grown Under Unconstrained Conditions
Ichiro Sunagawa, Tokyo, Japan

6 Defect Formation During Crystal Growth from the Melt
Peter Rudolph, Berlin, Germany

1. Crystal Growth Techniques and Characterization: An Overview

Govindhan Dhanaraj, Kullaiah Byrappa, Vishwanath (Vish) Prasad, Michael Dudley

A brief overview of crystal growth techniques and crystal analysis and characterization methods is presented here. This is a prelude to the details in subsequent chapters on fundamentals of growth phenomena, details of growth processes, types of defects, mechanisms of defect formation and distribution, and modeling and characterization tools that are being employed to study as-grown crystals and bring about process improvements for better-quality and large-size crystals.

1.1 **Historical Developments** 3

1.2 **Theories of Crystal Growth** 4
1.2.1 Surface Energy Theory 5
1.2.2 Diffusion Theory 5
1.2.3 Adsorption Layer Theory 6
1.2.4 Screw Dislocation Theory 6

1.3 **Crystal Growth Techniques** 6
1.3.1 Solid Growth 7
1.3.2 Solution Growth 8
1.3.3 Crystal Growth from Melt 9
1.3.4 Vapor-Phase Growth 10

1.4 **Crystal Defects and Characterization** 11
1.4.1 Defects in Crystals 11
1.4.2 Observation of Crystal Defects 12

References 15

1.1 Historical Developments

Crystals are the unacknowledged pillars of the world of modern technology. They have attracted human civilization from prehistoric times owing to their beauty and rarity, but their large-scale applications for devices have been realized only in the last six decades. For a long time, crystal growth has been one of the most fascinating areas of research. Although systematic understanding of the subject of crystal growth began during the last quarter of the 19th century with Gibbs' phase equilibrium concept based on a thermodynamical treatment, man practiced crystal growth and or crystallization processes as early as 1500 BC in the form of salt and sugar crystallization. Thus, crystal growth can be treated as an ancient scientific activity. However, the scientific approach to the field of crystal growth started in 1611 when Kepler correlated crystal morphology and structure, followed by Nicolous Steno, who explained the origin of a variety of external forms. Since then crystal growth has evolved steadily to attain its present status. Several theories were proposed from the 1920s onwards. The current impetus in crystal growth started during World War II. Prior to that, applications of crystals and crystal growth technology did not catch the attention of technologists. The growth of small or fine crystals in the early days, which involved uncontrolled or poorly controlled crystal growth parameters without much sophistication in instrumentation or crystal growth equipment, slowly led to the growth of large bulk crystals during World War II. With advancement in instrumentation technology, the attention of crystal growers focused on the quality of the grown crystals and understanding of their formation. Also, tailoring of crystal shape or morphology, size, and properties plays a key role in crystal growth science. In this context it is appropriate to mention nanocrystals, which exhibit desirable physicochemical characteristics. Similarly, the growth of thin films has emerged as a fascinating technology. Further crystal growth research is being carried out in microgravity or space conditions. There are various methods of evaluating the quality of grown crystals. Thus the growth of crystals with tailored physics and chemistry, characterization of crystals

with more advanced instrumentation, and their conversion into useful devices play vital roles in science and technology [1.1, 2].

Crystal growth is a highly interdisciplinary subject that demands the collaboration of physicists, chemists, biologists, engineers, crystallographers, process engineers, materials scientists, and materials engineers. The significance of the beauty and rarity of crystals is now well knitted with their symmetry, molecular structure, and purity, and the physicochemical environment of their formation. These characteristics endow crystals with unique physical and chemical properties, which have transformed electronic industries for the benefit of human society. Prior to commercial growth or production of crystals, man depended only on the availability of natural crystals for both jewelery and devices. Today the list of uses of artificially grown crystals is growing exponentially for a variety of applications, such as electronics, electrooptics, crystal bubble memories, spintronics, magnetic devices, optics, nonlinear devices, oscillators, polarizers, transducers, radiation detectors, lasers, etc. Besides inorganic crystal growth, the world of organic, semiorganic, biological crystal growth is expanding greatly to make crystal growth activity more cost-effective. Today, the quality, purity, and defect-free nature of crystals is a prerequisite for their technological application. A reader can get useful information on the history of crystal growth from the works of *Scheel* [1.3, 4].

Crystal growth is basically a process of arranging atoms, ions, molecules or molecular assemblies into regular three-dimensional periodic arrays. However, real crystals are never perfect, mainly due to the presence of different kinds of local disorder and long-range imperfections such as dislocations. Moreover, they are often polycrystalline in nature. Hence, the ultimate aim of a crystal grower is to produce perfect single crystals of desired shape and size, and to characterize them in order to understand their purity and quality and perfection for end users. Accordingly, crystal growth techniques and characterization tools have advanced greatly in recent years. This has facilitated the growth and characterization of a large variety of technologically important single crystals. Crystal growth can be treated as an important branch of materials science leading to the formation of technologically important materials of different sizes. Hence, it covers crystals from bulk to small and even to fine, ultrafine, and nanoscale sizes. In this respect, crystal growth has a close relationship with crystal engineering, and also polyscale crystal growth is relevant. This concept becomes even more relevant with progress achieved in nanotechnology, wherein the size effect explains changes in the physical properties of crystalline materials with size.

1.2 Theories of Crystal Growth

Growth of single crystals can be regarded as a phase transformation into the solid state from the solid, liquid or vapor state. Solid–solid phase transformations are rarely employed to grow single crystals, except for certain metals and metal alloys, whereas liquid to solid and vapor to solid transformations are most important in crystal growth and have resulted in a great variety of experimental techniques. When a crystal is in dynamic equilibrium with its mother phase, the free energy is at a minimum and no growth can occur. This equilibrium has to be disturbed suitably for growth to occur. This may be done by an appropriate change in temperature, pressure, pH, chemical potential, electrochemical potential, strain, etc. The three basic steps involved in the formation of a crystal from an initially disordered phase are:

1. Achievement of supersaturation or supercooling
2. Nucleation
3. Growth of the nuclei into single crystals of distinct phases

The driving force for crystallization actually derives from supersaturation, supercooling of liquid or gas phase with respect to the component whose growth is required. Therefore steady-state supersaturation/supercooling needs to be maintained during crystal growth to obtain higher-quality results. Nucleation or crystallization centers are an important feature of crystal growth. Nucleation may occur either spontaneously due to the conditions prevailing in the parent phase or it may be induced artificially. Therefore, the study of nucleation forms an integral part of crystal growth process. Several theories to explain nucleation have been proposed from time to time. Perhaps Gibbs was the first to comprehend that the formation of small embryonic clusters of some critical size is a prerequisite for the development of a macroscopic crystal. The

Gibbs–Thomson equation is fundamental for nucleation events [1.5], expressed for a cluster inside a supercooled phase under equilibrium conditions inside a supersaturated/supercooled phase as

$$k_B T \ln\left(\frac{p}{p^*}\right) = \frac{2\sigma V}{r} , \quad (1.1)$$

where r is the radius of the cluster formed inside a vapor at temperature T, k_B is the Boltzmann constant, p is the vapor pressure outside the cluster, p^* is the saturated vapor pressure over a plane liquid surface, σ is the surface energy per unit area, and V is the volume of the growth units.

For nucleation from solution,

$$k_B T \ln\left(\frac{c}{c^*}\right) = \frac{2\sigma V}{r} . \quad (1.2)$$

Here, c is the actual concentration and c^* is the concentration of the solution with a crystal of infinite radius. The condition for nucleation from the melt is

$$\Delta H_m \left(\frac{T_m - T_r}{T_m}\right) = \frac{2\sigma V}{r} . \quad (1.3)$$

Here, T_r is the melting point of a crystal of radius r and T_m is the melting point of a large crystal. ΔH_m is the latent heat of fusion per molecule.

The Gibbs–Thomson equation, which gives the free energy change per unit volume for solution growth, is given by

$$\Delta G_v = \frac{2\sigma}{r} = -k_B T \ln\left(\frac{c}{c^*}\right) = -\frac{k_B}{V} \ln S , \quad (1.4)$$

where S is the degree of supersaturation and V is the molecular volume.

There are several theories to explain crystal growth, involving the mechanism and the rate of growth of crystals. The important crystal growth theories are the surface energy theory, diffusion theory, adsorption layer theory, and screw dislocation theory. Gibbs proposed the first theory of crystal growth, in which he assumed growth of crystals to be analogous to the growth of a water droplet from mist. Later *Kossel* and others explained the role of step and kink sites on the growth surface in promoting the growth process [1.6].

1.2.1 Surface Energy Theory

The surface energy theory is based on the thermodynamic treatment of equilibrium states put forward by Gibbs. He pointed out that the growing surface would assume that shape for which the surface energy is lowest. Many researchers later applied this idea. *Curie* [1.7] worked out the shapes and morphologies of crystals in equilibrium with solution or vapor. Later, *Wulff* [1.8] deduced expressions for the growth rate at different faces and the surface free energies. According to him, the equilibrium is such that excess surface free energy $\sigma_{hkl} dA_{hkl}$ is minimum for crystal with its $\{hkl\}$ faces exposed. The value of σ_{hkl} determines the shape of a small crystal; for example, if σ is isotropic, the form of the crystal is spherical, provided the effect of gravity is negligible. *Marc* and *Ritzel* [1.9] considered the effect of surface tension and solution pressure (solubility) on the growth rate. In their opinion, different faces have different values of solubility. When the difference in solubility is small, growth is mainly under the influence of surface energy, and the change in the surface of one form takes place at the expense of the other. *Bravais* [1.10] proposed that the velocities of growth of the different faces of a crystal depend on the reticular density.

1.2.2 Diffusion Theory

The diffusion theory proposed by *Nernst* [1.11], *Noyes*, and *Whitney* [1.12] is based on the following two basic assumptions:

1. There is a concentration gradient in the neighborhood of the growing surface;
2. Crystal growth is the reverse process of dissolution.

Consequently, the amount of solute that will get deposited on a crystal growing in a supersaturated solution is given by

$$\frac{dm}{dt} = \left(\frac{D}{\delta}\right) A(c - c_0) , \quad (1.5)$$

where dm is the mass of solute deposited in a small time interval dt over an area A of the crystal surface, D is the diffusion coefficient of the solute, c and c_0 are the actual and equilibrium concentrations of the solute, and δ is the thickness of the torpid layer adjacent to the solid surface.

The importance of surface discontinuities in providing nucleation sites during crystal growth was the main consideration of *Kossel* [1.6], *Stranski* [1.13], and *Volmer* [1.14]. Volmer suggested a growth mechanism by assuming the existence of an adsorbed layer of atoms or molecules of the growth units on crystal faces. Later, *Brandes* [1.15], Stranski, and Kossel modified this concept. Volmer's theory was based on thermodynamical reasoning. The units reaching a crystal face are not immediately attached to the lattice but migrate over the

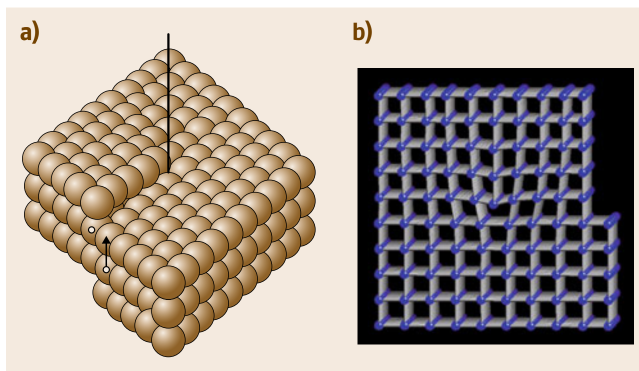

Fig. 1.1a,b Screw dislocation in a crystal (**a**); edge dislocation (**b**)

crystal face to find a suitable site for attachment. They form a loosely adsorbed layer at the interface, and soon a dynamic equilibrium is established between the layer and the bulk solution.

1.2.3 Adsorption Layer Theory

Kossel viewed crystal growth based on atomistic considerations. He assumed that crystal is in equilibrium with its solution when it is just saturated. Also, the attachment energy unit on growing surface is a simple function of distance only. The attachment energy is due to van der Waals forces if the crystal is homopolar, while it is due to electrostatic forces if the crystal is heteropolar (ionic). A growth unit arriving at a crystal surface finds attachment sites such as terraces, ledges, and kinks. The attachment energy of a growth unit can be considered to be the resultant of three mutually perpendicular components. The binding energy or attachment energy of an atom is maximum when it is incorporated into a kink site in a surface ledge, whilst at any point on the ledge it is greater than that for an atom attached to the flat surface (terrace). Hence, a growth unit reaching a crystal surface is not integrated into the lattice immediately. Instead it migrates to a step and moves along it to a kink site, where it is finally incorporated. Based on this consideration of attachment, Kossel was able to determine the most favorable face for growth. According to the Kossel model, growth of a crystal is a discrete process and not continuous. Also, a new layer on a preferably flat face of a homopolar crystal will start growing from the interior of the face. For heteropolar crystals, the corners are the most favorable for growth, while mid-face is least favored. According to Stranski, the critical quantity that determines the growth process is the work necessary to detach a growth unit from its position on the crystal surface. Growth units with the greatest detachment energy are most favored for growth, and vice versa. The greatest attraction of atoms to the corners of ionic and metallic crystals often leads to more rapid growth along these directions, with the result that the crystal grows with many branches called dendrites radiating from a common core.

1.2.4 Screw Dislocation Theory

However, the Kossel, Stranski, and Volmer theory could not explain the moderately high growth rates observed in many cases at relatively low supersaturation, far below those needed to induce surface nucleation. *Frank* [1.16] proposed that a screw dislocation emerging at a point on the crystal surface could act as a continuous source of steps (surface ledges) which can propagate across the surface of the crystal and promote crystal growth. Growth takes place by rotation of the steps around the dislocation point (Fig. 1.1). *Burton* et al. [1.17] proposed the famous screw dislocation theory based on the relative supersaturation as the Burton–Cabrera–Frank (BCF) model determining the absolute value of growth rate depending upon the concentration. Frank's model could explain the experimental observations on the growth rate and spiral pattern mechanism.

1.3 Crystal Growth Techniques

Crystal growth is a heterogeneous or homogeneous chemical process involving solid or liquid or gas, whether individually or together, to form a homogeneous solid substance having three-dimensional atomic arrangement. Various techniques have been employed, depending upon the chemical process involved. All crystal growth processes can be broadly classified according to the scheme presented in Table 1.1. The subject of crystal growth has therefore developed as an interdisciplinary subject covering various branches of science, and it is extremely difficult to discuss the entire subject in this overview chapter. However, the

Table 1.1 Classification of crystal growth processes [1.18]

Process	Starting phase	Condition	Result / Techniques
1. Solid–Solid	Solid	$\xrightarrow{T}$	Solid Devitrification Strain annealing Polymorphic phase change Precipitation from solid solution
2. Liquid–Solid			
i) Melt growth	Molten material	$\xrightarrow{\text{Dec. } T}$	Crystal Bridgman–Stockbarger Kyropoulos Czochralski Zoning Verneuil
ii) Flux growth	Solid(s) + Flux agent(s)	$\xrightarrow{\text{Dec. } T}$	Crystal(s)
iii) Solution growth	Solid(s) + Solvent	$\xrightarrow{\text{Low } T}$	Crystal(s) Evaporation Slow cooling Boiling solutions
iv) Hydrothermal growth	Solid(s) + Solvent	$\xrightarrow[\text{High } p]{\text{High } T}$	Crystal(s) Hydrothermal sintering Hydrothermal reactions Normal temperature gradient Reversed temperature gradient
v) Gel growth	Solution + Gel medium	$\xrightarrow{\text{Low } T}$	Crystal Reaction Complex decomplex Chemical reduction Solubility reduction Counter-flow diffusion
	Solution	$\longrightarrow$	Crystal(s) + products
3. Gas–Solid	Vapor(s)	$\longrightarrow$	Solid Sublimation–condensation Sputtering Epitaxial processes Ion-implantation

present Handbook covers most important techniques adopted in modern crystal growth through the chapters authored by world authorities in their respective fields.

1.3.1 Solid Growth

The solid-state growth technique is basically controlled by atomic diffusion, which is usually very slow except in the case of fast ionic conductors or superionic conductors. The commonly used solid-state growth techniques are annealing or sintering, strain annealing, heat treatment, deformation growth, polymorphic phase transitions, quenching, etc., and most of these are popularly used in metallurgical processes for tailoring material properties. In fact, gel growth is also considered as solid growth by some researchers. Solid growth is not covered in this Handbook.

1.3.2 Solution Growth

This is one of the oldest and most widely used crystal growth techniques compared with vapor-phase melt growth. Solution growth is used not only for growth of technologically important crystals but also for a variety of crystalline products for daily life such as the growth of foods, medicines, fertilizers, pesticides, dye stuffs, etc. Most crystallization processes of ionic salts are conducted in aqueous solutions or in some cases in solvents which are a mixture of miscible and organic solvents. Solution growth is used for substances that melt incongruently, decompose below the melting point, or have several high-temperature polymorphic modifications, and is also often efficient in the absence of such restrictions. The important advantage of solution growth is the control that it provides over the growth temperature, control of viscosity, simplicity of equipment, and the high degree of crystal perfection since the crystals grow at temperatures well below their melting point. We can divide solution growth into three types depending upon the temperature, the nature of the solvent, solute, and the pressure: low-temperature aqueous solution growth, superheated aqueous solution growth, and high-temperature solution growth. Aqueous solution growth has produced the largest crystals known to mankind, such as potassium dihydrogen phosphate (KDP), deuterated potassium dihydrogen phosphate (DKDP), etc. produced at the Lawrence Livermore Laboratory, USA.

For successful growth of a crystal from solution, it is essential to understand certain basic properties (physicochemical features) of the solution. The behavior of water with temperature and pressure; the critical, subcritical, and supercritical conditions; its structure, the variation in pH; viscosity; density; conductivity; dielectric constant; and coefficient of expansion are critical for successful crystal growth. Recently, a rational approach to the growth of a given crystal was carried out in order to: compute the thermodynamic equilibrium as a function of the processing variables, generate equilibrium (yield) diagrams to map the processing variable space for the phases of interest, design experiments to test and validate the computed diagrams, and utilize the results for mass production [1.19]. The change in ionic strength of the solution during crystal growth results in formation of defects, and variation in the crystal habit and even the phases, and therefore has to be maintained constant, often with the help of swamping-electrolyte solutions. Similarly, chelating agents are frequently used to sequester ions and form respective complexes, which are later thermodynamically broken to release their cations very slowly into the solution, which helps in controlling the growth rate and crystal habit.

In the last decade crystal growth from solution under microgravity conditions has been studied extensively to grow a wide variety of crystals such as zeolites, compound semiconductors (InP, GaAs, GaP, AlP, etc.), triglycine sulfate, etc.

Crystal Growth from Low-Temperature Aqueous Solutions

The greatest advantages of crystal growth from low-temperature aqueous solutions are the proximity to ambient temperature, which helps to retain a high degree of control over the growth conditions, especially with reference to thermal shocks, and reduction of both equilibrium and nonequilibrium defects to a minimum (even close to zero). Solution growth can be classified into several groups according to the method by which supersaturation is achieved:

1. Crystallization by changing the solution temperature
2. Crystallization by changing the composition of the solution (solvent evaporation)
3. Crystallization by chemical reaction

Crystal Growth from Superheated Aqueous Solutions

This method is commonly known as the hydrothermal method and is highly suitable for crystal growth of compounds with very low solubility and phase transitions. When nonaqueous solvents are used in the system, it is called the solvothermal method. The largest known single crystal formed in nature (beryl crystal of > 1000 kg) is of hydrothermal origin, and similarly some of the largest quantities of single crystals produced in one experimental run (quartz single crystals of > 1000 kg) are based on the hydrothermal technique. The term "hydrothermal" refers to any heterogenous (usually for bulk crystal growth) or homogeneous (for fine to nanocrystals) chemical reaction in the presence of aqueous solvents or mineralizers under high-pressure and high-temperature conditions to dissolve and recrystallize (recover) materials that are relatively insoluble under ordinary conditions [1.20]. The last decade has witnessed growing popularity of this technique, and a large variety of crystals and crystalline materials starting from native elements to the most complex coordinated compounds such as rare-earth silicates, germinates, phosphates, tungstates, etc. have been obtained. Also,

the method is becoming very popular among organic chemists dealing with synthesis of life-forming compounds and problems related to the origin of life. The method is discussed in great detail in Chap. 18.

Crystal Growth from High-Temperature Solutions

This is popularly known as flux growth and gained its importance for growing single crystals of a wide range of materials, especially complex multicomponent systems. In fact, this was one of the earliest methods employed for growing technologically important crystals, for example, single crystals of corundum at the end of the 19th century. The main advantage of this method is that crystals are grown below their melting temperature. If the material melts incongruently, i. e., decomposes before melting or exhibits a phase transition below the melting point or has very high vapor pressure at the melting point, one has indeed to look for growth temperatures lower than these phase transitions. The method is highly versatile for growth of single crystals as well as layers on single-crystal substrates (so-called liquid-phase epitaxy, LPE). The main disadvantages are that the growth rates are smaller than for melt growth or rapid aqueous solution growth, and the unavoidable presence of flux ions as impurities in the final crystals. Some of the important properties to be considered for successful flux growth of crystals are stability and solubility of the crystal to be grown, low melting point and lower vapor pressure of the flux, the lower viscosity of the melt (which should not attack the crucible), and also ease of separation [1.4,21]. The most commonly used fluxes are the basic oxides or fluorides: PbO, PbF_2, BaO, BaF, Bi_2O_3, Li_2O, Na_2O, K_2O, KF, B_2O_3, P_2O_5, V_2O_5, MoO_3, and in most cases a mixture consisting of two or three of them. The prime advantage of this method is that growth can be carried out either through spontaneous nucleation or crystallization on a seed. Supersaturation can be achieved through slow cooling, flux evaporation, and vertical temperature gradient transport methods. Also, during the growth, one can introduce rotation of the seed or crucible, or pulling of the seed, and so on. Accordingly, several versions of flux growth have been developed: slow cooling (SC), slow cooling bottom growth (SCBG), top-seeded solution growth (TSSG), the top-seeded vertical temperature gradient technique (VTGT), bottom growth with a nutrient, growth by traveling solvent zone (TSZ), flux evaporation, LPE, and so on.

The flux method has been popularly used especially for the growth of a large variety of garnets, and recently for a wide range of laser crystals such as rare-earth borates, potassium titanyl phosphates, and so on. The reader can get valuable information from several interesting reviews on flux growth [1.22–24].

1.3.3 Crystal Growth from Melt

Melt growth of crystals is undoubtedly the most popular method of growing large single crystals at relatively high growth rates. In fact, more than half of technological crystals are currently obtained by this technique. The method has been popularly used for growth of elemental semiconductors and metals, oxides, halides, chalcogenides, etc. Melt growth requires that the material melts without decomposition, has no polymorphic transitions, and exhibits low chemical activity (or manageable vapor pressure at its melting point). The thermal decomposition of a substance and also chemical reactions in the melt can disturb the stoichiometry of the crystal and promote formation of physical or chemical defects. Similarly, the interaction between the melt and crucible, or the presence of a third component derived from the crystallization atmosphere, can affect melt growth. Usually, an oxygen-containing atmosphere is used for oxides, a fluorine-containing atmosphere for fluorides, a sulfur-containing atmosphere for sulfides, and so on. In melt growth, crystallization can be carried out in a vacuum, in a neutral atmosphere (helium, argon, nitrogen), or in a reducing atmosphere (air, oxygen). In a large melt volume, convective flows caused by the temperature gradient within the melt lead to several physical and chemical defects. In a small melt volume, transport is affected by diffusion.

Selection of a particular melt growth technique is done on the basis of the physical and chemical characteristics of the crystal to be grown. Metal single crystals with melting point $< 1800\,°C$ are grown by Stockbarger method, and those with melting point $> 1800\,°C$ by zone melting. Semiconducting crystals are grown chiefly by Czochralski method, and by zone melting. Single crystals of dielectrics with melting point $< 1800\,°C$ are usually grown by the Stockbarger or Czochralski methods, while higher-melting materials are produced by flame fusion (Verneuil method). If the physicochemical processes involved in crystallization are taken into account, it is possible to establish optimum growth conditions.

One of the earliest melt techniques used to grow large quantity of high-melting materials was the Verneuil method (flame fusion technique), first described by *Verneuil* in 1902 [1.25]. This marks the

beginning of commercial production of large quantities of high-melting crystals, which were essentially used as gems or for various mechanical applications. Today, the technique is popular for growth of a variety of high-quality crystals for laser devices and precision instruments, as well as substrates. The essential features are a seed crystal, the top of which is molten and is fed with molten drops of source material, usually as a powder through a flame or plasma. Following this, the Czochralski method, developed in 1917 and later modified by several researchers, became the most popular technique to grow large-size single crystals which were impossible to obtain by any other techniques in such large quantity. This technique has several advantages over the other related melt-growth technique, viz. the Kyropoulos method, which involves a gradual reduction in the melt temperature. In the Czochralski technique the melt temperature is kept constant and the crystal is slowly pulled out of the melt as it grows. This provides a virtually constant growth rate for the crystal. Several versions of Czochralski crystal pullers are commercially available. A large variety of semiconductor crystals such as Si, Ge, and several III–V compounds are being commercially produced using this technique. Besides, several other crystals of oxides, spinel, garnets, niobates, tantalates, and rare-earth gallates have been obtained by this method. The reader can find more valuable information on this method from the works of *Hurle* and *Cockyane* [1.26].

There are several other popularly used melt growth techniques that are feasible for commercial production of various crystals. Amongst them, the Bridgman–Stockbarger, zone melting, and floating zone methods are the most popular. The Bridgman technique is characterized by the relative translation of the crucible containing the melt to the axial temperature gradient in a vertical furnace. The Stockbarger method is a more sophisticated modification of the Bridgman method. There is a high-temperature zone, an adiabatic loss zone, and a low-temperature zone. The upper and lower temperature zones are generally independently controlled, and the loss zone is either unheated or poorly insulated.

1.3.4 Vapor-Phase Growth

Vapor-phase growth is particularly employed in mass production of crystals for electronic devices because of its proven low cost and high throughput, in addition to its capability to produce advanced epitaxial structures. The technique is especially suitable for growth of semiconductors, despite the rather complex chemistry of the vapor-phase process. The fundamental reason for their success is the ease of dealing with low- and high-vapor-pressure elements. This is achieved by using specific chemical precursors in the form of vapor containing the desired elements. These precursors are introduced into the reactor by a suitable carrier gas and normally mix shortly before reaching the substrate, giving rise to the nutrient phase of the crystal growth process. The release of the elements necessary for construction of the crystalline layer may occur at the solid–gas interface or directly in the gas phase, depending on the type of precursors and on the thermodynamic conditions.

The advantage of vapor growth technique is that crystals tend to have a low concentration of point defects and low dislocation densities compared with crystals grown from the melt, as the temperatures employed are usually considerably lower than the melting temperature. Moreover, if the material undergoes a phase transformation or melts incongruently, vapor growth may be the only choice for the growth of single crystals. Although the method was initially used to grow bulk crystals, with the enormous importance of thin films in electronic and metallurgical applications, vapor growth is now widely used to grow thin films, epitaxial layers, and substrates in the field of semiconductor technology [1.27, 28].

Vapor-phase growth primarily involves three stages: vaporization, transport, and deposition. The vapor is formed by heating a solid or liquid to high temperatures. Transportation of vapor may occur through vacuum, driven by the kinetic energy of vaporization. Deposition of the vapor may occur by condensation or chemical reaction.

Various techniques exist in vapor-phase growth, differentiated by the nature of the source material and the means and mechanism by which it is transported to the growing crystal surface. Conceptually, the simplest technique is that of sublimation, where the source material is placed at one end of a sealed tube and heated so that it sublimates and is then transported to the cooler region of the tube, where it crystallizes.

Among vapor-phase growth techniques, vapor-phase epitaxy is the most popularly used, especially for the growth of p- and n-type semiconductor whose dimers and monomers are difficult to achieve by other methods (e.g., physical evaporation) or too stable to be reduced to the necessary atomic form. Furthermore, there are different variants such as metalorganic vapor-phase epitaxy (MOVPE), plasma-assisted mo-

Table 1.2 Main application fields of vapor-phase epitaxy techniques and the relevant classes of materials

Growth technique	Devices and semiconductor family			
	Si, Ge	**II–VI**	**III–V**	**III–nitrides**
Hydride VPE	SiGe alloys		LEDs and photodetectors (GaP, InGaP, GaAsP)	GaN thick layers
Chloride VPE	Bipolar transistors, MOS			
MOVPE		IR sensors (HgCdTe), LEDs and lasers (ZnCdSe, ZnSSe)	Solar cells (GaAs, AlGaAs, InGaP), transistors (AlGaAs, InGaAs), LEDs (AlGaAs), TC and CD lasers (InGaPAs, AlGaAs), photodetectors, LEDs and lasers (InGaPAs)	LEDs and lasers (GaN, InGaN, GaAlN)

lecular beam epitaxy (MBE), etc. to suit the growth of particular compounds. Table 1.2 summarizes the main application fields of the VPE techniques and the relevant classes of materials [1.29].

1.4 Crystal Defects and Characterization

Characterization of crystals has become an integral part of crystal growth and process development. Crystal defects and their distribution together with composition and elemental purity determine most of their properties such as mechanical strength, electrical conductivity, photoconductivity luminescence, and optical absorption, and these properties influence their performance in applications. Therefore, investigating the origin, concentration, and distribution of imperfections in crystals is critical to controlling them and thereby the crystal properties influenced by these imperfections.

1.4.1 Defects in Crystals

Imperfections or defects can be broadly classified based on their dimensionality.

Point Defects

These zero-dimensional defects are vacancies, interstitials, and impurity atoms deliberately added to control the conductivity of the semiconductor, and impurities that are unintentionally incorporated as contaminants during material growth and processing. Electronic defects such as holes and electrons also constitute point defects. In compounds, point defects form disorders such as Frenkel, Schottky, and antistructure disorders.

Line Defects

Line defects consist of purely geometrical faults called dislocations. The concept of dislocations arose from the crystallographic nature of plastic flow in crystalline materials. A dislocation is characterized by its line direction and Burgers vector $\boldsymbol{b}$, which is, as a rule, one of the shortest lattice translations. Dislocation lines may be straight or follow irregular curves or closed loops. Dislocations whose line segments are parallel to $\boldsymbol{b}$ are called screw dislocations. Edge dislocations have their line segments perpendicular to the $\boldsymbol{b}$ direction. In mixed dislocations, the line direction is inclined to $\boldsymbol{b}$ and hence they have both screw and edge components.

Planar Defects

Planar defects include high- and low-angle boundaries, growth striations, growth-sector boundaries, twin boundaries, stacking faults, and antiphase boundaries. Growth striations are lattice perturbations that arise from local variations of the dopant/impurity concentration created by fluctuations in the growth conditions. Stacking faults are formed when there are errors in the normal stacking arrangement of the lattice planes in the crystal structure. These could be caused by plastic deformation or agglomeration of point defects. High- and low-angle boundaries consist of arrays of dislocations, and they separate regions of different orientations. In crystal growth, high-angle boundaries separate grains that have been nucleated independently, and hence misorientations are generally large. Low-angle grain boundaries are formed during cool down by stress-induced glide and climb of dislocations, leading to these energetically favorable configurations. Misorientations

in this case usually do not exceed more than 1°. Twin boundaries are planar defects that separate regions of the crystal whose orientations are related to each other in a definite, symmetrical way.

Volume Defects

Precipitates, inclusions, and voids or bubbles are volume defects, and these are formed when gases dissolved in the melt precipitate out after solidification. For example, in microgravity growth, the absence of buoyancy precludes degassing of the melt, resulting in the formation of voids. While undissolved foreign particles are generally classified as inclusions, a second type of inclusion is formed during growth from nonstoichiometric melt. Compound semiconductors generally sublime incongruently, thereby causing a slight excess of one of the components in a stoichiometric melt. On solidification, the excess component forms inclusions.

1.4.2 Observation of Crystal Defects

Techniques for observing dislocations and their complex structures have been described in detail by *Verma* [1.30] and *Amelincks* [1.31]. The commonly used techniques come under the categories:

1. Optical methods
2. X-ray methods
3. Preferential etching
4. Microscopy techniques
5. Other techniques

All these methods provide almost direct observation of defects. Their merit is limited by the resolution achievable and their versatility. Choice of a suitable technique will depend on several factors, such as:

1. The shape and size of the crystal under investigation
2. Cleaving, cutting, and polishing possibilities
3. Ability to use destructive techniques, and above all
4. The extent of the details required

Optical Methods

A common inspection method for the as-grown optical crystal boule is detailed observation by illuminating the boule using high-intensity white light or a laser beam. Probably, this is the first technique to be applied to assess the quality of as-grown crystal and can reveal bubbles, cavities, growth bands, and seed interfaces which depend on the growth parameters.

The conoscope is a simple optical tool for investigating optical inhomogeneity in very small crystals to large-size boules. Conoscopic patterns are characteristic for every main crystallographic orientation, and this feature is also frequently used for orienting crystals [1.32]. This method shows the overall quality of the crystal. If the whole crystal has low dislocation density without any grain boundaries and block structures, a nice symmetrical circular pattern of dark and bright fringes with four segments and a cross at the center is observed. Figure 1.2a shows the conoscopic pattern of a sapphire ingot with dislocation density $10^2–10^3\,/\mathrm{cm}^2$ and without any low-angle grain boundaries. Figure 1.2b shows the pattern for a sapphire ingot of the same size but with a dislocation density of the order of $10^3–10^4\,/\mathrm{cm}^2$ and a few low-angle grain boundaries. The presence of a few grain boundaries alters the birefringence and distorts the fringes. The fringe thickness and spacing depend on the length of the crystal along the direction of inspection. Even though this technique does not reveal the dislocation density very precisely, it can reveal the presence of grain boundaries and higher-order, complex defects. The crystals are normally sliced perpendicular to the *c*-axis, polished, and inspected under a polarizer and analyzer. As-cut surfaces without polishing can also be observed with the application of suitable refractive-index-matched fluid. In general, this technique can reveal the misorientations, grain boundaries, block structures, and also the stress levels. Conoscopy can be used under a polarizing microscope to study thinner samples. A custom-made polarizer and analyzer with rotation features for the analyzer and sample support can be used to study large crystal boules. Alternatively, conoscopic fringes can be projected onto a screen using a laser beam, polarizer and analyzer, and beam diffuser. These fringes are more influenced by the birefringence inhomogeneity induced by defect structures than by variation in the thickness distribution of the boule itself.

X-Ray Methods

X-ray methods can be classified into:

1. High-resolution x-ray diffraction
2. X-ray topography
3. Synchrotron x-ray topography

High-Resolution X-Ray Diffraction. Diffraction for a given plane and wavelength takes place over a finite angular range about the exact Bragg condition, known as the rocking-curve width [1.33]. In x-ray diffractometry, the intensity of the diffracted beam and the angle in the vicinity of a Bragg peak are measured and repre-

sented as a full-width at half-maxima (FWHM) rocking curve. The double-axis rocking curve is obtained by scanning the specimen in small steps through the exact Bragg condition and recording the diffracted intensity. The peak width of a rocking curve can be affected by tilts and dilations in the sample, and by curvature. Tilts are regions in the sample where grains or subgrains are tilted with respect to each other, although the lattice parameter is the same in each region. Dilations are regions where the lattice planes are still parallel but the spacing is slightly different due to strain. Changes in lattice parameter also occur in alloyed crystals with nonhomogeneous composition distribution. The experimentally obtained rocking-curve width (FWHM) value is a measure of the crystalline quality of the sample, and it can be compared with a theoretically calculated value. It is possible to obtain a rocking-curve width less than 10 arcsec for a good crystalline sample. Additional information that can be obtained from double-axis rocking curves are substrate–epilayer mismatch, epilayer composition, substrate offcut and/or layer tilt, and layer thickness.

A limitation of double-axis diffraction is that it cannot distinguish between tilts and dilations. In triple-axis diffraction, a third axis is introduced in the form of an analyzer crystal, and tilts and strain can be separated; the rocking-curve width is still narrow. Double-axis rocking curve analysis is sufficient for studying substrates and epitaxial films. Triple-axis x-ray diffraction is used for obtaining finer details of the defect structure of the sample.

X-Ray Topography. Localized variations in intensity within any individual diffracted spot arise from structural nonuniformity in the lattice planes causing the spot, and this forms the basis for the x-ray topographic technique. This topographic contrast arises from differences in the intensity of the diffracted beam as a function of position inside the crystal. The difference between the intensities diffracted from one region of the crystal which diffracts kinematically to another which diffracts dynamically is one of the ways that dislocations can be rendered visible in topography [1.34].

Even though the first topographic image of a single crystal was recorded as early as 1931 [1.35], the real potential of the technique was understood only in 1958 when Lang [1.36] demonstrated imaging of individual dislocations in a silicon crystal. In general, there are three main types of x-ray topographic geometries for studying defects:

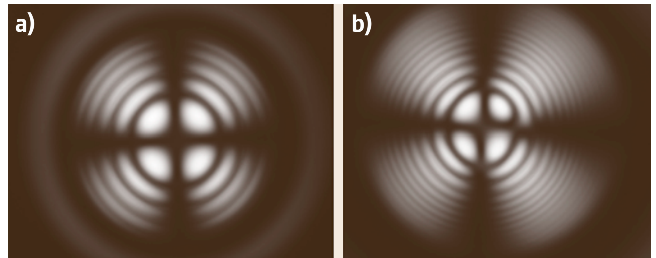

Fig. 1.2 **(a)** Conoscopic pattern of high-quality sapphire ingot. **(b)** Conoscopic pattern of sapphire ingot that has a few low-angle boundaries

1. The Berg–Barrett reflection technique [1.37]
2. The double-crystal technique [1.38]
3. The Lang technique [1.36] and its variant – the scanning oscillator technique [1.39]

Following *Lang*'s work [1.36, 40] in imaging of individual dislocations, x-ray topography has become an important quality-control tool for assessment of semiconductor wafers both before and after device fabrication. Using the scanning oscillator technique developed by *Schwuttke* [1.39], it is possible to record transmission topographs of large-size wafers up to 150 mm in diameter, containing appreciable amounts of elastic and/or frozen-in strain.

Synchrotron X-Ray Topography. The advent of dedicated synchrotron radiation sources has enabled the development of a new field of x-ray topography known as synchrotron topography. Synchrotron radiation is especially suitable for x-ray topography because of the high brightness and low divergence of the x-ray beam. Due to the small source dimensions, low divergence angle, as well as the long source–specimen distance, extremely high resolution can be achieved using synchrotron radiation compared with conventional x-ray topography. For example, based on the geometrical factor, the theoretical resolution obtained can be as low as 0.06 μm. Also, it has numerous advantages over laboratory x-ray topography. One of the most important synchrotron topographic techniques developed is white-radiation topography [1.41]. In APS, the white beam is monochromatized by two cooled parallel Si(111) crystals, and the x-ray energy is tunable in the range 2.4–40 keV.

Crystals as large as 150 mm or even 300 mm in diameter can be imaged by using precision translation stages similar to those used in the Lang technique, and the exposure times are much shorter. If a single crystal is oriented in the beam, and the diffracted beams are

recorded on a photographic detector, each diffraction spot on the resultant Laue pattern will constitute a map of the diffracting power from a particular set of planes as a function of position in the crystal, with excellent point-to-point resolution. There are three common geometries for synchrotron x-ray topography [1.42]:

1. Transmission geometry, also called Laue geometry: In this mode, the x-ray beam passes through the sample and the topographs recorded reveal the bulk defect information of the crystal. Figure 1.3a shows typical transmission synchrotron topography of a 2 inch LED-grade wafer with a very low dislocation density of 10^2–10^3 /cm^2. The topograph shows the dislocation structure in the entire wafer, which shows the presence of basal dislocations.
2. Gazing-incidence reflection geometry: In this configuration, very small incident angle is used [in the case of SiC, typically 2° used and the $(11\bar{2}8)$ or $(11\bar{2}.12)$ are recorded]. Grazing incidence is used because of the low penetration depth of the x-ray beam, which is more suitable for studying epilayers.
3. Back-reflection geometry: In this mode, a large Bragg angle is used for basal plane reflection $(000l)$ (typically 80° for SiC). Screw dislocations along the c-axis and basal plane dislocations within the x-ray penetration depth can be clearly recorded. The wavelength satisfying Bragg condition is automatically selected in white-beam x-ray topography, while in monochromatic synchrotron x-ray topography (XRT), the energy of the x-ray beam has to be preset to satisfy the diffraction condition. Figure 1.3b shows individual screw dislocations and edge dislocation running almost perpendicular to the wafer.

X-ray topographs are typically recorded on Agfa Structurix D3-SC, Ilford L4 nuclear plate, or VRP-M holographic films, depending on the resolution needed. Exposure time depends on the actual geometry and recording media and varies between a few seconds and 2 h.

Selective Etching

Selective etching is a simple and very sensitive tool for the characterization of single crystals. The usefulness of the etching technique lies in the formation of visible, sharp contrasting etch pits at dislocation sites. The power of etching has been reviewed by several workers [1.31, 43, 44]. The formation of etch pit can be explained as follows. The lattice is distorted for a distance of a few atoms around dislocations. As a result of the stress field generated by the deformation, the lattice elements dissolve more easily at the dislocation sites than in stress-free, undeformed areas. The etch pits are usually straight pyramids with polygonal bases, but other types of pyramids may also be found with various bases and heights. Etch pits can be formed only if certain conditions are satisfied, the most important of these being that the dissolution rate along the surface (V_t) must not greatly exceed the rate of dissolution perpendicular to the surfaces (V_n). The ratio (V_t/V_n) can be increased:

1. By increasing V_n, as has been done in the etchants of several metals
2. By decreasing V_t by adding an inhibitor such as in LiF
3. By varying the temperature to alter the activation energies of V_n and V_t

The etch pits are formed at the dislocation sites, which essentially reveal the emergent point of the dislocations in the surface; they therefore give a direct measure of dislocation density. Since they have certain depths, they also give information on the kind [1.45], configuration, and inclination of dislocations. Etching has also been used to study the stress–velocity rela-

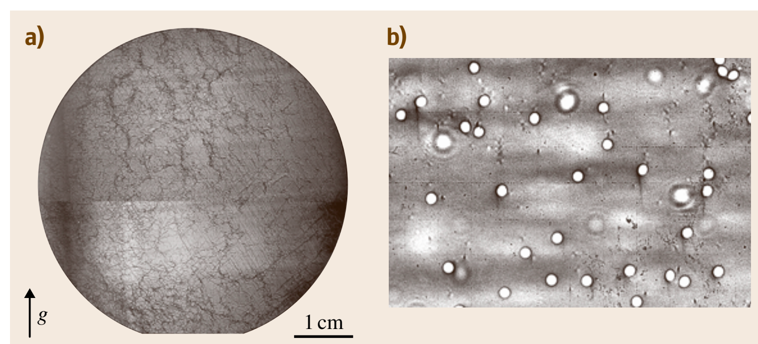

Fig. 1.3 **(a)** Transmission topograph of high-quality sapphire wafer. **(b)** Reflection topograph of SiC revealing individual threading screw dislocations running almost perpendicular to the wafer

tions for individual dislocations [1.46]. Movement of dislocations, deformation patterns like pile-up, origin of dislocations in as-grown crystals, polarity of the crystals, grain boundaries, and distribution of dislocations in crystals can be studied [1.44, 45] (Chap. 43). The greatest advantage of this technique is its simplicity and resolution ($0–10^{12}$ /cm^2). This technique shows the defect density on small areas and hence requires averaging of values taken at a large number of locations. Also, this technique is not a nondestructive method and cannot show the basal plane dislocation when the sample is sliced exactly parallel to the c-axis. Figure 1.4 shows the presence of various defects such as threading edge dislocations, threading screw dislocations, and basal plane dislocations. During the development of SiC crystals, this technique has seen tremendous development and could reveal almost every type of dislocation [1.47].

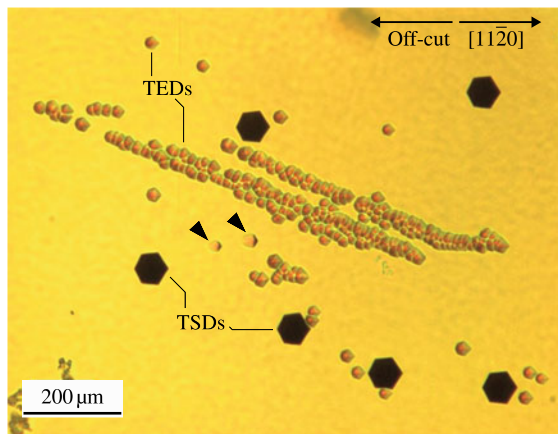

Fig. 1.4 Etch pit pattern of SiC wafer revealing threading edge dislocations (TEDs), threading screw dislocations (TSDs), and basal plane dislocations

Microscopy Techniques

Transmission electron microscopy (TEM) (Chap. 44) is a powerful tool to study dislocations when the sample has higher defect density. It is more commonly used for epitaxial films, where large numbers of dislocations originate due to the lattice misfit between the film and the substrate. This method requires tedious sample preparation and is not considered nondestructive.

Decoration is another important technique, where impurity atoms segregate and settle down along dislocation lines during annealing. The decorated dislocations can be observed easily under an optical microscope in transmission mode [1.31].

Growth spirals, which are true manifestations of screw dislocations, can be observed under optical microscopy, scanning electron microscopy (SEM), and atomic force microscopy (AFM). The presence of growth spirals helps to understand the growth mechanism [1.30].

Infrared (IR) microscopy is similar to optical microscopy except for the fact that IR light is used for illumination, with a wavelength comparable to the bandgap of semiconductor materials. This technique is used to study inclusions, cavities, and even dislocations present in the sample [1.48, 49].

Other Techniques

Photoluminescence (PL) [1.50], electron paramagnetic resonance (EPR) (Chap. 45), positron annihilation (Chap. 46), and micro Raman spectroscopy [1.50] are also used to study semiconductor materials and show electronic defect states and the presence of impurities very successfully.

References

1.1 J. Kepler: *Strena seu de nive sexangula* (Tampach, Frankfurt 1611)

1.2 N. Steno: *De solido intra solidum naturaliter contento dissertationis prodromus* (Stella, Florence 1669), English translation by J.G. Winter (Hafner, New York 1968

1.3 H.J. Scheel: Historical introduction. In: *Handbook of Crystal Growth*, Vol. 1a, ed. by D.T.J. Hurle (Elsevier, Amsterdam 1993) pp. 1–41, Chap. 1

1.4 D. Elwell, H.J. Scheel: *Crystal Growth from High Temperature Solution* (Academic, London 1975)

1.5 J.W. Gibbs: *On the Equilibrium of Heterogeneous Substances*, Collected Works (Longmans Green, New York 1928)

1.6 W. Kossel: Zur Theorie des Kristallwachstums, Nachr. Ges. Wiss. Göttingen **135**, 135–143 (1927)

1.7 P. Curie: Sur la formation des criteaux et sur les constantes capillaires de leurs differentes faces, Bull. Soc. Franc. Mineral. **8**, 145–150 (1885)

1.8 G. Wulff: Zur Frage der Geschwindigkeit des Wachstums und der Auflösung von Krystallflächen, Z. Kristallogr. **34**, 449 (1901)

1.9 R. Marc, A. Ritzel: Über die Faktoren, die den Kristallhabitus bedingen, Z. Phys. Chem. **76**, 584 (1911)

1.10 A. Bravais, A. Etudes: *Crystallographiques* (Gauthier Villers, Paris 1866)

1.11 W. Nernst: Theorie der Reaktionsgeschwindigkeit in heterogenen Systemen, Z. Phys. Chem. **47**(1), 52–55 (1904)
1.12 A.A. Noyes, W.R. Whitney: Über die Auflösungsgeschwindigkeit von festen Stoffen in ihren eigenen Lösungen, Z. Phys. Chem. **23**, 689–692 (1897)
1.13 I.N. Stranski: Zur Theorie des Kristallwachstums, Z. Phys. Chem. **136**, 259–278 (1928)
1.14 M. Volmer, A. Weber: Keimbildung in übersättigten Gebilden, Z. Phys. Chem. **119**, 277–301 (1926)
1.15 E.A. Brandes: *Smithells Reference Book* (Butterworths, London 1983)
1.16 F.C. Frank: The influence of dislocations on crystal growth, Discuss. Faraday Soc. **5**, 48–54 (1949)
1.17 W.K. Burton, N. Cabrera, F.C. Frank: The growth of crystals and the equilibrium structure of their surfaces, Philos. Trans. R. Soc. London A **243**, 299–358 (1951)
1.18 K. Byrappa, D.Y. Pushcharovsky: Crystal chemistry and its significance on the growth of technological materials, Prog. Cryst. Growth Charact. Mater. **24**, 269–350 (1992)
1.19 M.M. Lencka, R.E. Riman: Thermodynamics of the hydrothermal synthesis of calcium titanate with reference to other alkaline-earth titanates, Chem. Mater. **7**(1), 18–25 (1995)
1.20 K. Byrappa, M. Yoshimura: *Handbook of Hydrothermal Technology* (William Andrew Noyes, Norwich 2001)
1.21 W. Tolksdorf: Flux growth. In: *Handbook of Crystal Growth-Bulk Crystal Growth*, Vol. 2, ed. by D.T.J. Hurle (North-Holland, Amsterdam 1994) p. 563, Chap. 10
1.22 R.A. Laudise: *The Growth of Single Crystals* (Prentice Hall, Englewood Cliffs 1970)
1.23 B.M.R. Wanklyn: Practical aspects of flux growth by spontaneous nucleation. In: *Crystal Growth*, Vol. 1, ed. by B.R. Pamplin (Pergamon, Oxford 1974) pp. 217–288
1.24 V.V. Timofeeva: *Growth of Crystals from High Temperature Solutions* (Nauka, Moscow 1975)
1.25 A. Verneuil: Production artificielle du rubis par fusion, C. R. Paris **135**, 791–794 (1902)
1.26 D.T.J. Hurle, B. Cockyane: Czochralski growth. In: *Handbook of Crystal Growth*, Vol. 2a, ed. by D.T.J. Hurle (North Holland, Amsterdam 1994) pp. 99–212, Chap. 3
1.27 D.T.J. Hurle (Ed.): *Handbook of Crystal Growth* (North Holland, Amsterdam 1994)
1.28 G. Stringfellow: *Organometallic Vapor-Phase Epitaxy: Theory and Practice*, 2nd edn. (Academic, New York 1998)
1.29 R. Fornari: Vapor phase epitaxial growth and properties of III-Nitride materials. In: *Crystal Growth of Technologically Important Electronic Materials*, ed. by K. Byrappa, T. Ohachi, H. Klapper, R. Fornari (Allied Publishers, New Delhi 2003)
1.30 A.R. Verma: *Crystal Growth and Dislocations* (Butterworths, London 1953)
1.31 S. Amelinckx: The direct observation of dislocations. In: *Solid State Physics*, ed. by F. Seitz, D. Turnbull (Academic, New York 1964), Suppl. 6
1.32 E.A. Wood: *Crystals and Light* (Dover, New York 1977)
1.33 B.K. Tanne: High resolution x-ray diffraction and topography for crystal characterization, J. Cryst. Growth **99**, 1315 (1990)
1.34 B.K. Tanner: *X-ray Diffraction Topography* (Pergamon, Oxford 1976)
1.35 V.W. Berg: Über eine röntgenographische Methode zur Untersuchung von Gitterstörung an Kristallen, Naturwissenschaften **19**, 391–396 (1931)
1.36 A.R. Lang: Direct observation of individual dislocations, J. Appl. Phys. **29**, 597–598 (1958)
1.37 C.S. Barrett: A new microscopy and its potentialities, Trans. AIME **161**, 15–65 (1945)
1.38 W.L. Bond, J. Andrus: Structural imperfections in quartz crystals, Am. Mineral. **37**, 622–632 (1952)
1.39 G.H. Schwuttke: New x-ray diffraction microscopy technique for study of imperfections in semiconductor crystals, J. Appl. Phys. **36**, 2712–2714 (1965)
1.40 A.R. Lang: Point-by-point x-ray diffraction studies of imperfections in melt-grown crystals, Acta Cryst. **10**, 839 (1957)
1.41 J. Miltat: White beam synchrotron radiation. In: *Characterization of Crystal Growth Defects by X-ray Methods*, NATO ASI Ser. B, Vol. 63, ed. by B.K. Tanner, D.K. Bowen (Plenum, New York 1980) pp. 401–420
1.42 B. Ragothamachar, G. Dhanaraj, M. Dudley: Direct analysis in crystals using x-ray topography, Microsc. Res. Tech. **69**, 343 (2006)
1.43 A.J. Forty: Direct observations of dislocations in crystals, Adv. Phys. **3**, 1–25 (1954)
1.44 W.G. Johnson: Dislocations etchpits in nonmetallic crystals. In: *Progress in Ceramics*, Vol. 2, ed. by J.E. Burke (Pergamon, Oxford 1962) p. 1
1.45 K. Sangawal: *Etching of Crystals* (North-Holland, Amsterdam 1987)
1.46 J.J. Gilman, W.G. Johnston: Behaviour of individual dislocations in strain-hardened LiF crystals, J. Appl. Phys. **31**, 687–692 (1960)
1.47 W.J. Choyke, H. Matsunami, G. Pensl (Eds.): *Silicon Carbide: Recent Major Advances* (Springer, Berlin, Heidelberg 2004)
1.48 A. Hossain, A.E. Bolotnikov, G.S. Camarda, Y. Cui, G. Yang, K-H. Kim, R. Gul, L. Xu, R.B. James: Extended defects in CdZnTe crystals: Effects on device performance, J. Cryst. Growth (2010) in press (doi:10.1016/j.jcrysgro.2010.03.005)
1.49 U.N. Roy, S. Weler, J. Stein, A. Gueorguiev: Unseeded growth of CdZnTe:In by THM technique, Proc. SPIE **7449**, 74490U (2009)
1.50 J. Jimenez (Ed.): *Microprobe Characterization of Optoelectronic Materials* (Taylor Francis, New York 2003)

2. Nucleation at Surfaces

Ivan V. Markov

This chapter deals with the thermodynamics and kinetics of nucleation on surfaces, which is essential to the growth of single crystals and thin epitaxial films. The starting point is the equilibrium of an *infinitely* large crystal and a crystal with a finite size with their ambient phase. When the system deviates from equilibrium density fluctuations or aggregates acquire the tendency to unlimited growth beyond some critical size – the nucleus of the new phase. The Gibbs free energy change of formation of the nuclei is calculated within the framework of the macroscopic thermodynamics and in terms of dangling bonds in the case of small clusters. In the case of nucleation from vapor the nuclei consist as a rule of very small number of atoms. That is why the rate of nucleation is also considered in the limit of high supersaturations. The effect of defect sites and overlapping of nucleation exclusion zones with reduced supersaturation formed around the growing nuclei is accounted for in determining the saturation nucleus density. The latter scales with the ratio of the surface diffusion coefficient and the atom arrival rate. The scaling exponent is a function of the critical nucleus size and depends on the process which controls the frequency of attachment of atoms to the critical nuclei to produce stable clusters, either the surface diffusion or the incorporation of atoms to the critical nuclei. The nucleation on top of two-dimensional (2-D) islands is considered as a reason for roughening in homoepitaxial growth. The mechanism of formation of three-dimensional (3-D) islands in heteroepitaxial growth is also addressed. The effect of surface-active species on the rate of nucleation is explored.

2.1 **Equilibrium Crystal–Ambient Phase** 18
- 2.1.1 Equilibrium of Infinitely Large Phases 18
- 2.1.2 Equilibrium of Small Crystal with the Ambient Phase............... 20
- 2.1.3 Equilibrium Shape of Crystals......... 22

2.2 **Work for Nucleus Formation** 24
- 2.2.1 General Definition........................ 24
- 2.2.2 Formation of 3-D Nuclei on Unlike Substrates..................... 25
- 2.2.3 Work of Formation of 2-D Crystalline Nuclei on Unlike and Like Substrates........ 27

2.3 **Rate of Nucleation**............................... 28
- 2.3.1 General Formulation 28
- 2.3.2 Rate of Nucleation on Single-Crystal Surfaces 30
- 2.3.3 Equilibrium Size Distribution of Clusters 31
- 2.3.4 Rate of Nucleation....................... 32

2.4 **Saturation Nucleus Density**.................... 35

2.5 **Second-Layer Nucleation in Homoepitaxy**.................................. 38

2.6 **Mechanism of Clustering in Heteroepitaxy** 43

2.7 **Effect of Surfactants on Nucleation** 45

2.8 **Conclusions and Outlook** 48

References 48

Nucleation at surfaces plays a crucial role in the growth of crystals and epitaxial overlayers for the preparation of advanced materials with potential for technological applications. In homoepitaxy of metal or semiconductor films the instability of planar growth against roughening depends on the kinetics of two-dimensional

nucleation [2.1]. The interplay of wetting and strain leads to clustering in overlayers growing under elastic stress in heteroepitaxy and determines the mechanism of growth and in turn the film morphology [2.2–4]. Smooth quantum wells or self-assembled quantum dots can be grown by varying the conditions of growth (temperature or growth rate) or by use of third species which change both the thermodynamics and kinetics of the processes involved [2.5]. The growth of thin epitaxial films in particular by molecular-beam epitaxy (MBE) usually occurs far from equilibrium. Thus, in addition to thermodynamics, one has to account for the kinetic processes taking place on the crystal surface [2.6]. The latter are responsible for the remarkable richness of patterns which are observed during growth [2.7].

This chapter gives the essential physics of the thermodynamics and kinetics of nucleation, both three- and two-dimensional, on like and unlike substrates as well as some later developments such as the Ehrlich–Schwoebel effect on second-layer nucleation and the effect of surface-active species on nucleation rate. The presentation is oriented more to the needs of experimentalists rather than going deeply into theoretical problems. The chapter is organized as follows. We start with problems of equilibrium of crystals and epitaxial overlayers with the parent phase (vapor, solution) in Sect. 2.1 and consider the equilibrium vapor pressure of infinitely large and finite-size crystals, the thermodynamic driving force for nucleation to occur, and the equilibrium shape of three-dimensional (3-D) crystals on unlike surfaces. In Sect. 2.2 we define the work for nucleus formation in the most general way and consider the limiting cases of the classical (capillary) theory of nucleation at low or intermediate values of supersaturation and the atomistic approach at high supersaturations. We derive expressions for the work of formation of three-dimensional nuclei on unlike substrates and two-dimensional nuclei on like and unlike substrates. In Sect. 2.3 we give a general formulation of the nucleation rate and again derive expressions valid for high and low supersaturations. We consider further in Sect. 2.4 the saturation nucleus density accounting for the influence of defect (active) sites stimulating nucleation events and the overlapping of undersaturated nucleation exclusion zones around growing clusters. Making use of the rate equation approach we derive expressions for the saturation nucleus density in thin epitaxial films in diffusion and kinetic regimes of growth. In Sect. 2.5 we consider the effect of the step-edge Ehrlich–Schwoebel barrier on second-layer nucleation as a reason for the formation of mounds and thus roughening of surfaces in homoepitaxy. The mechanism of transformation of monolayer-high two-dimensional (2-D) islands into three-dimensional crystallites in Volmer–Weber and Stranski–Krastanov growth is addressed in Sect. 2.6. In Sect. 2.7 we explore the effect of surface-active species on the kinetics of nucleation. Some conclusions and outlook are given in Sect. 2.8.

2.1 Equilibrium Crystal–Ambient Phase

In treating the title problem we use the atomistic approach developed by *Kaischew* and *Stranski* [2.8]. It is based on the assumption of additivity of bond energies and accounts for the elementary processes taking place during growth and dissolution of the particles of the new phase. Although apparently old fashioned this approach is extremely instructive and informative for understanding the essential physics of the equilibrium of infinitely large phases and phases with finite size as well as of the deviation from equilibrium leading to transitions from one phase to another. Numerical studies of the stability of small clusters performed by making use of modern quantum-mechanical methods lead to the same conclusion that the closed atomic structures are most stable [2.9].

2.1.1 Equilibrium of Infinitely Large Phases

We consider for simplicity one-component system. The equilibrium between infinitely large phases (crystal, liquid or vapor) is determined by the equality of the respective chemical potentials. In 1927 *Kossel* and *Stranski* simultaneously developed an atomistic approach which is in fact identical to the definition of the macroscopic thermodynamics [2.10–12]. They considered the different sites that atoms can occupy on the crystal surface and found that there exists one particular site which plays a crucial role in crystal nucleation and growth. They introduced the concept of the *half-crystal position*, which turned out to be intimately connected with the chemical potential of an infinitely large crystal.

Consider the cubic face of a crystal with a simple cubic lattice (a Kossel crystal) containing a monatomic step (Fig. 2.1). Atoms can be located at different sites on the crystal surface. They can be built in the uppermost lattice plane or into the step edge, be adsorbed at the step edge or on the terrace, or can occupy the corner site (3) which has very peculiar properties. An atom in this position is connected with a half-atomic row, a half-crystal plane, and a half-crystal block. This is the reason the term half-crystal position (*Halbkristalllage* or kink position) was coined for this particular site. Therefore, the work of separation of an atom from this position is exactly equal to the lattice energy of the crystal per building particle. Hence, the work of detachment of an atom from this position is given by

$$\varphi_{1/2} = \tfrac{1}{2}(Z_1\psi_1 + Z_2\psi_2 + Z_3\psi_3 \ldots) ,$$

where Z_i are the numbers of neighbors of the consecutive coordination spheres and ψ_i are the respective bond energies.

Whereas atoms in other positions have different numbers of saturated and unsaturated (dangling) bonds, the atom in the kink position (3) has an equal number of saturated and dangling bonds. Therefore, the separation work from a half-crystal position serves as a specific reference with which the probabilities for elementary processes at other sites to take place can be compared. The detachment of an atom from the half-crystal position gives rise to the same position. It follows that, when an atom is detached from this position, the number of dangling bonds remains unchanged and in turn the surface energy does not change. Hence, the whole crystal (if it is large enough to avoid finite-size effects) can be built up or disintegrated into single atoms by repetitive attachment or detachment of atoms to and from this position.

In equilibrium with its vapor the probability of attachment of atoms to this position must be equal to the probability of their detachment. Hence the work of detachment of atoms from this position will determine the equilibrium vapor pressure and in turn its chemical potential. For simple crystals with monatomic vapor the latter will be given at zero temperature (the change of entropy is equal to zero) by

$$\mu_c^\infty = -\varphi_{1/2} , \qquad (2.1)$$

where the superscript ∞ indicates an infinitely large crystal.

As seen the chemical potential of an infinitely large crystal is equal to the work of detachment of atoms from the half-crystal position taken with a negative sign. It is this property which makes this position unique in the theory of crystal nucleation and growth [2.13].

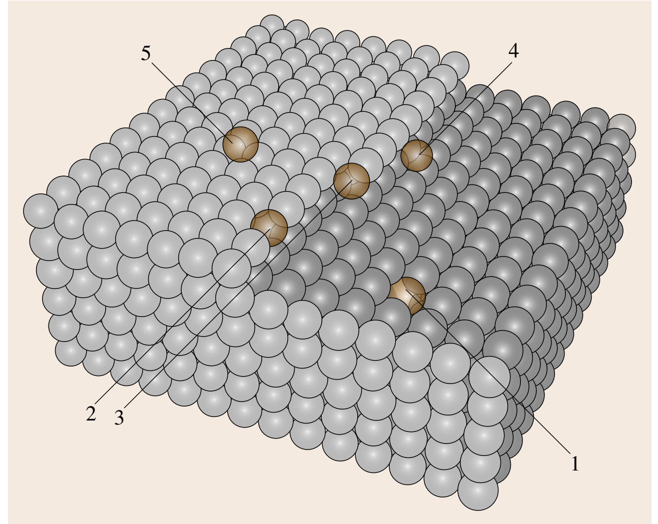

Fig. 2.1 The most important sites an atom can occupy on a crystal surface: 1 – atom embedded into the uppermost crystal plane, 2 – atom embedded into the step edge, 3 – atom in a half-crystal (kink) position, 4 – atom adsorbed at the step, 5 – atom adsorbed on the terrace

There is one more very important property of the half-crystal position. We can divide $\varphi_{1/2}$ into two parts: lateral interaction with the half-atomic row and the half-crystal plane, and the normal interaction with the half-crystal block underneath. If we replace the underlying crystal block by another block of different material and crystal lattice the lateral bonding will remain more or less unchanged if we assume additivity of bond energies. However, the normal bonding will change substantially owing to the difference in both chemical bonding and lattice strain. It is easy to show that the separation work from a kink position in this particular case can be written as

$$\varphi'_{1/2} = \varphi_{1/2} - (\psi - \psi') , \qquad (2.2)$$

where ψ' is the energy of a bond between unlike atoms.

Having in mind (2.1), (2.2) can be written as

$$\mu'_c = \mu_c^\infty + (\psi - \psi') . \qquad (2.3)$$

We now define the surface energy of a crystal by the following imaginary process. We cleave isothermally and reversibly the crystal into two halves and produce two surfaces with area S. We count the bonds we break

and divide the energy spent by $2S$. If we confine ourselves to nearest-neighbor bonds in the case of Kossel crystal we break one bond per atom and obtain ($S = a^2$)

$$\sigma = \frac{\psi}{2a^2} , \tag{2.4}$$

where a is the atomic diameter.

Using the above definition and the relation of *Dupré* [2.14]

$$\sigma_i = \sigma_A + \sigma_B - \beta , \tag{2.5}$$

which connects the specific interfacial energy σ_i between the unlike crystals A and B with the specific adhesion energy $\beta = \psi'/a^2$, (2.3) can be written as

$$\mu'_c = \mu_c^\infty + a^2(\sigma + \sigma_i - \sigma_s) . \tag{2.6}$$

It is immediately seen that the term in the brackets $\Delta\sigma = \sigma + \sigma_i - \sigma_s$ is in fact the parameter that accounts for the wetting of the substrate (the half-crystal block underneath) by the overlayer in epitaxy of one material on the surface of another [2.15]. Thus, when $\Delta\sigma < 0$, or what is the same, $\psi < \psi'$ (complete wetting), the equilibrium vapor pressure of the first monolayer on the unlike substrate will be smaller than the equilibrium vapor pressure of the bulk crystal ($\mu = \mu_0 + k_B T \ln P$), i.e., $P'_\infty < P_\infty$. This means that at least the first monolayer can be deposited at a vapor pressure smaller than the equilibrium vapor pressure of the bulk crystal, or in other words, at undersaturation, $P'_\infty < P < P_\infty$ [2.16]. If the two crystals have different lattice parameters the growth should continue by formation of three-dimensional (3-D) islands. This is the famous Stranski–Krastanov mechanism of growth [2.17], in which the accumulation of strain energy with film thickness makes the planar film unstable against clustering. Obviously, if the lattice misfit is equal to zero the growth will continue layer by layer in the so-called Frank–van der Merwe mechanism of growth [2.18, 19]. In the opposite case of incomplete wetting ($\Delta\sigma > 0$), 3-D islanding will take place from the very beginning of deposition or Volmer–Weber growth, which requires supersaturation, $P > P_\infty$ [2.20]. We thus see that the separation work from a half-crystal position plays a fundamental role in determining the mechanism of epitaxial growth.

The lattice misfit increases the tendency for 3-D islanding by increasing the interfacial energy in (2.6) with the energy per unit area of misfit dislocations or elastic strain. Thus for heteroepitaxial growth the interfacial energy reads [2.21]

$$\sigma_i^* = \sigma_i + \varepsilon_m ,$$

where ε_m is either the misfit dislocation energy or the energy of the homogeneous strain.

Thus the interfacial energy between misfitting crystals consists of two parts: a chemical part σ_i accounting for the difference in chemistry and strength of bonding, and a geometrical part ε_m accounting for the difference of lattices and lattice parameters. If the misfit in heteroepitaxy is accidentally or intentionally tailored to be equal to zero (particularly in binary or ternary alloys) $\varepsilon_m = 0$, but the chemical part σ_i remains different from zero and affects the mechanism of growth.

It should be noted that the misfit plays a decisive role for clustering only in Stranski–Krastanov growth, where it changes the sign of $\Delta\sigma$ from negative to positive beyond the so-called wetting layer. In Volmer–Weber growth $\Delta\sigma$ is positive and the strain energy makes a minor contribution with the same sign to it. Frank–van der Merwe growth takes place only in systems with zero misfit [2.22], which is why we will not take into consideration the effect of lattice misfit in nucleation.

2.1.2 Equilibrium of Small Crystal with the Ambient Phase

The separation work from the half-crystal position cannot determine the equilibrium of a crystal with finite size with its surrounding because the role of the crystal edges and corners cannot be ignored. The kink position is no longer a repetitive step for dissolution of the crystal. That is why Stranski and Kaischew suggested that the condition for a small crystal to be in equilibrium with the ambient phase is for the probability of building up a whole crystal plane to be equal to the probability of its dissolution. In this way the effect of the edge and corner atoms are accounted for in addition to the atoms in half-crystal positions. Obviously, the smaller the crystal, the greater will be the role of the corner and edge atoms, and vice versa. Thus they defined the *mean separation work* as the work per atom to disintegrate a whole crystal plane into single atoms. This quantity must have one and the same value for all crystal faces belonging to the equilibrium shape.

Consider for simplicity a small Kossel crystal with a shape of a cube with edge length $l_3 = an_3$, where n_3 is the number of atoms in the edge of the cube. Confining ourselves to nearest-neighbor bond energy ψ the energy for dissolution of a whole lattice plane into single atoms (by counting the bonds we break in the process of disintegration, Fig. 2.2) is $3n_3^2\psi - 2n_3\psi$. Dividing by the number of atoms n_3^2 the mean separation work

reads [2.8]

$$\bar{\varphi}_3 = 3\psi - \frac{2\psi}{n_3} , \qquad (2.7)$$

or, bearing in mind that for a simple cubic lattice $3\psi = \varphi_{1/2}$,

$$\bar{\varphi}_3 = \varphi_{1/2} - \frac{2\psi}{n_3} .$$

It follows that the mean work of separation tends asymptotically to the work of separation from a half-crystal position as the crystal size is increased. We conclude that a crystal can be considered as small if $n_3 < 70$, or $l_3 < 2\times10^{-6}$ cm assuming $a \approx 3$ Å.

As $\bar{\varphi}_3$ determines the equilibrium vapor pressure of the small crystal and in turn its chemical potential we can write in analogy with (2.1) for $T = 0$

$$\mu_c = \mu_v = -\bar{\varphi}_3 .$$

Then

$$\Delta\mu = \mu_v(P) - \mu_c^{\infty}(P) = \varphi_{1/2} - \bar{\varphi}_3 = \frac{2\psi}{n_3} \qquad (2.8)$$

is the difference of the chemical potentials of the *infinitely large* vapor and crystal phases which represents the thermodynamic driving force for nucleation to occur, or the *supersaturation*.

The equilibrium of the vapor and the crystal takes place at some vapor pressure P_∞ (to stress the fact that the crystal is infinitely large) so that $\mu_v(P_\infty) = \mu_c(P_\infty)$. Then we can write (2.8) as

$$\Delta\mu = [\mu_v(P) - \mu_v(P_\infty)] - [\mu_c(P) - \mu_c(P_\infty)] .$$

For small deviations from equilibrium the differences in the above equation can be replaced by derivatives and

$$\Delta\mu = \int_{P_\infty}^{P} \frac{\partial\mu_v}{\partial P}\,dP - \int_{P_\infty}^{P} \frac{\partial\mu_c}{\partial P}\,dP = \int_{P_\infty}^{P} (v_v - v_c)\,dP ,$$

where v_v and v_c are the molecular volumes of the vapor and the crystal. As $v_v \gg v_c$ the above equation simplifies to

$$\Delta\mu = \int_{P_\infty}^{P} v_v\,dP .$$

Considering the vapor as an ideal gas ($v_v = k_B T/P$) gives upon integration

$$\Delta\mu = k_B T \ln\left(\frac{P}{P_\infty}\right) . \qquad (2.9)$$

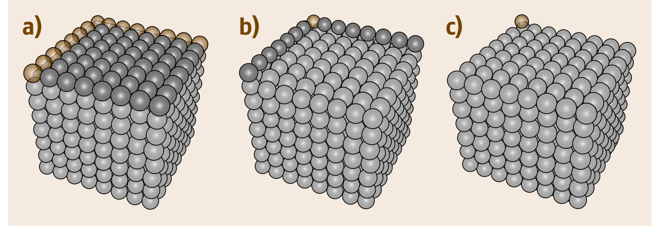

Fig. 2.2a–c Schematic for the evaluation of the mean separation work which determines the equilibrium of a small three-dimensional crystal with the supersaturated vapor phase. In stage **(a)** we detach $(n-1)^2$ atoms, breaking three bonds per atom, in stage **(b)** we detach $2(n-1)$ atoms, breaking two bonds per atom, and finally in **(c)** we detach the last atom, breaking a single bond

The supersaturation $\Delta\mu$ is usually very large in the case of nucleation from vapor, particularly in methods such as MBE. Let us evaluate it for the case of nucleation in MBE growth of Si(111). The supersaturation is given in terms of the ratio of the fluxes R/R_∞, where $R = P/\sqrt{2\pi m k_B T}$, rather than in vapor pressures as in (2.9). Typical growth conditions are $T = 600$ K and $R = 1\times10^{13}$ atom/cm^2 s [2.23]. The equilibrium vapor pressure of Si at 600 K is $P_\infty = 1.3\times10^{-27}$ N/m^2. Then, $R_\infty \cong 6.5\times10^{-8}$ atom/cm^2 s and $\Delta\mu \cong 2.5$ eV. This means that the supersaturation is of the order of the enthalpy of evaporation of Si (≈ 4.5 eV). As we will see below this is why nuclei consist of a number of atoms of the order of unity.

Note that, with the approximation made, (2.9) is valid for very small deviations from equilibrium. If we repeat the above calculations at much higher temperature, say 1300 K, we find $\Delta\mu \cong 0.05$ eV. We can believe this value to be close to the real figure, but for low temperatures we can be sure only of the sign of the supersaturation (growth or evaporation) but not its numerical value.

Equation (2.8) represents the famous Thomson–Gibbs equation which gives the dependence of the equilibrium vapor pressure of a small crystal on its linear size. Using the definition of the specific surface energy (2.4) we obtain the Thomson–Gibbs equation in its form which is well known in the literature

$$\Delta\mu = \frac{4\sigma v_c}{l_3} . \qquad (2.10)$$

We consider further the equilibrium with the vapor phase (and in turn with the dilute adlayer) of a small two-dimensional crystal with a monolayer height formed on the surface of a large three-dimensional crystal. Such an island grows or dissolves by attach-

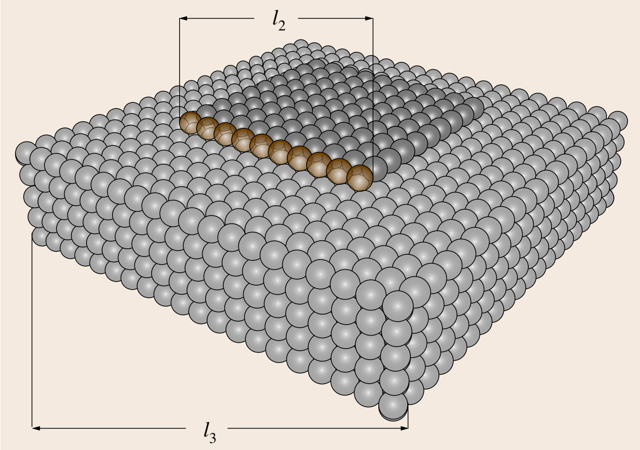

Fig. 2.3 Schematic for the evaluation of the mean separation work which determines the equilibrium of a small two-dimensional crystal with the supersaturated vapor phase. In equilibrium the probabilities of evaporation and building of a whole row of atoms (*black spheres*) are equal

ment or detachment of whole atomic rows. That is why *Kaischew* and *Stranski* suggested that the probability of building of a whole atomic row with length $l_2 = n_2 a$ is equal to the probability of its disintegration into single atoms [2.8]. The equilibrium 2-D island–vapor phase is now determined by the mean separation work $\bar{\varphi}_2$, which is equal to the energy per atom for evaporation of a whole edge row of atoms (Fig. 2.3). Assuming a square-shaped island with n_2 atoms in the edge the mean separation work reads

$$\bar{\varphi}_2 = 3\psi - \frac{\psi}{n_2} = \varphi_{1/2} - \frac{\psi}{n_2} .$$

The supersaturation necessary for the formation of a two-dimensional island with linear size l_2 then reads

$$\Delta\mu = \frac{\psi}{n_2} . \tag{2.11}$$

Note that in nucleation on surfaces the supersaturation can be expressed as a ratio of the real and the equilibrium adatom concentrations (in equilibrium the chemical potential of the vapor is equal to the chemical potential of the adlayer, which in turn depends on the adatom concentration)

$$\Delta\mu = k_B T \ln\left(\frac{N_1}{N_1^e}\right) ,$$

where [2.24]

$$N_1^e = N_0 \exp\left(-\frac{\Delta W}{k_B T}\right) , \tag{2.12}$$

the difference $\Delta W = \varphi_{1/2} - E_{des}$ being the work to transfer an atom from a half-crystal position on the surface of a terrace, and N_0 is the atomic density of the crystal surface.

This is particularly true when the adatom concentration is determined by a dynamic adsorption–desorption equilibrium, i. e., when the atom arrival rate R is equal to the re-evaporation rate N_1/τ_s, where $\tau_s = \nu^{-1} \exp(E_{des}/k_B T)$ is the mean residence time of an atom on the surface before desorption.

We define now the specific edge energy in the same way that we defined the specific surface energy (2.4). We cleave an atomic plane into two halves and produce two edges with length L. We break one bond per atom and for the specific edge energy one obtains

$$\varkappa = \frac{\psi}{2a} . \tag{2.13}$$

Combining (2.11) and (2.13) gives the Thomson–Gibbs equation for the two-dimensional case, or the supersaturation required to form an island with edge length l_2, in its more familiar form [2.24]

$$\Delta\mu = \frac{2\varkappa a^2}{l_2} . \tag{2.14}$$

Equations (2.10) and (2.14) can be derived by using the method of thermodynamic potentials introduced by Gibbs (for a review see [2.21]). However, contrary to the pure thermodynamics, the above *molecular-kinetic* or atomistic approach accounts in addition for the elementary processes of growth and dissolution of crystals. The growth of sufficiently large crystal takes place by attachment of building units to the half-crystal position. Once the atom is incorporated at this position we can say that it has joined the crystal lattice. Small three- and two-dimensional crystals grow and dissolve by building and dissolution of whole crystal planes or atomic rows, respectively.

2.1.3 Equilibrium Shape of Crystals

In 1878 *Gibbs* defined thermodynamically the problem of the equilibrium shape of crystals as the shape at which the crystal has a minimum surface energy at given constant volume [2.25]. This definition later acquired a geometric interpretation in the well-known Gibbs–Wulff theorem [2.26], according to which the distances h_n from an arbitrary (Wulff's) point to the different crystal faces are proportional to the corre-

sponding specific surface energies σ_n of these faces

$$\frac{\boldsymbol{\sigma}_n}{\boldsymbol{h}_n} = \text{const.} \quad (2.15)$$

As a result the equilibrium shape represents a closed polyhedron consisting of the faces with the lowest specific surface energies. The areal extents of the crystal faces belonging to the equilibrium shape have one and the same value of chemical potential.

Half a century later *Kaischew* extended this approach to cover the case of a crystal on a foreign substrate and derived a relation known in the literature as the Wulff–Kaischew theorem [2.27]

$$\frac{\sigma_n}{h_n} = \frac{\sigma_i - \beta}{h_i} = \text{const.} \,, \quad (2.16)$$

where σ_i is the specific surface energy of the crystal face that is in contact with the substrate and h_i is the distance from the Wulff point to the plane of the contact (Fig. 2.4).

It is seen that the distance from the Wulff point to the contact plane is proportional to the difference $\sigma_i - \beta$. Therefore, when the catalytic potency of the substrate β is equal to zero, the distance h_i will have its value in the absence of a substrate. In this case we have *complete nonwetting*. At the other extreme $\beta = \sigma_A + \sigma_B = 2\sigma$ ($\sigma_A = \sigma_B = \sigma$) we have *complete wetting* and the three-dimensional crystal is reduced to a monolayer-high island. In the intermediate case $0 < \beta < 2\sigma$ we have *incomplete wetting* and the crystal height is smaller than its lateral extent.

The introduction of the separation work from half-crystal position and the mean separation works enabled Stranski and Kaischew to provide a new atomistic approach for determination of the equilibrium shape of crystals. The latter is necessary for calculation of the work of nucleus formation as it is assumed that the nuclei preserve the equilibrium shape as the lowest-energy shape. Thus the lowest-energy pathway of the crystallization process is ensured.

The basic idea is that atoms bound more weakly than an atom in the half-crystal position cannot belong to the equilibrium shape. We start from a sufficiently large crystal with a simple crystallographic form and remove in succession from its surface all atoms bound more weakly than in a half-crystal position. Precisely at that process all the faces of the equilibrium shape appear. Then the areas of the faces are varied by removal and addition of whole crystal planes up to the moment when the mean separation works of all crystal faces become equal. As the mean separation works are closely

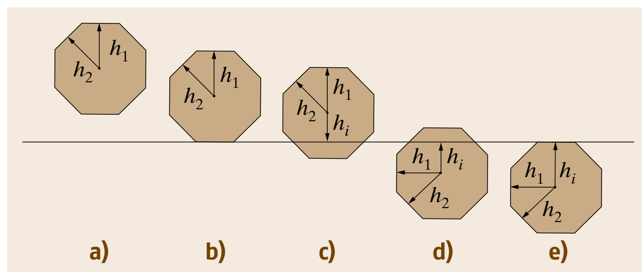

Fig. 2.4a–e Equilibrium shape of a crystal on an unlike substrate. The distances $\boldsymbol{h}_1$ and $\boldsymbol{h}_2$ in the free polyhedron **(a)** are proportional to the specific free energies σ_1 and σ_2 according to the Gibbs–Wulff theorem (2.15). In the presence of unlike substrate the distances to free surfaces remain the same as in the free polyhedron. The distance h_i to the plane of contact is determined by the difference $\sigma_i - \beta$ according to the Wulff–Kaischew theorem (2.16). **(b)** Complete nonwetting ($\beta = 0$); **(c,d)** different degrees of incomplete wetting (note that in the latter case the vector h_i is negative); **(e)** complete wetting ($\beta = 2\sigma$)

related to the chemical potentials the latter condition is equivalent to the definition of Gibbs. Thus, during the last operation of equating the mean separation works of all crystal faces, those which do not belong to the equilibrium shape disappear [2.28].

Therefore, the necessary and sufficient condition for the equilibrium shape of a crystal in the molecular-kinetic approach is equality of the mean separation works, or in other words, of the chemical potentials of all crystal faces. We use this condition to derive the equilibrium aspect ratio of a three-dimensional cubic crystal on the surface of an unlike crystal assuming incomplete wetting ($\Delta\sigma > 0$).

Consider a cubic crystal with a square base with edge length $l = na$ and height $h = n'a$, where n and n' are the number of atoms in the horizontal and vertical edges (Fig. 2.5). The mean separation work calculated

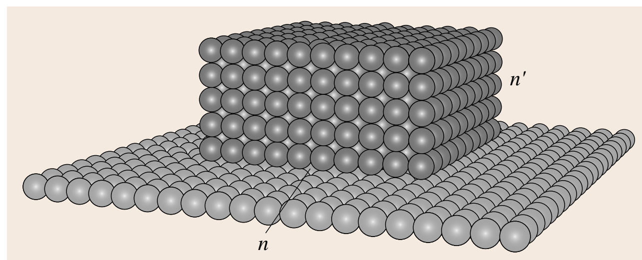

Fig. 2.5 A cubic crystal with n and n' atoms in the base and the height on the surface of an unlike crystal at incomplete wetting

from the side crystal face is

$$\bar{\varphi}_3' = 3\psi - \frac{\psi - \psi'}{n'} - \frac{\psi}{n} ,$$

whereas the same quantity calculated for the upper base is given by (2.7). The condition $\bar{\varphi}_3 = \bar{\varphi}_3'$ gives

$$\frac{h}{l} = \frac{n'}{n} = \phi , \quad (2.17)$$

where

$$\phi = 1 - \frac{\psi'}{\psi} . \quad (2.18)$$

Substituting ψ and ψ' by the specific surface and adhesion energies and making use of the relation of Dupré (2.5) gives ϕ in terms of surface energies

$$\phi = \frac{\sigma + \sigma_\mathrm{i} - \sigma_\mathrm{s}}{2\sigma} . \quad (2.19)$$

As seen, the equilibrium aspect ratio of the crystal is precisely equal to the familiar wetting condition (2.6) relative to 2σ. The parameter ϕ is known in the literature as the *wetting function*; it plays a crucial role in nucleation at surfaces and determines the mechanism of growth of thin epitaxial films [2.15, 29]. It can be shown that (2.19) can be derived by the classical thermodynamic condition of the minimum of the surface energy $\Phi = 4lh\sigma + l^2(\sigma + \sigma_\mathrm{i} - \sigma_\mathrm{s})$ at constant volume $V = l^2 h$ [2.15].

2.2 Work for Nucleus Formation

2.2.1 General Definition

The nuclei of the new phase represent local fluctuations of the density which can be considered as small molecular aggregates. If the phase is stable the density fluctuations increase the thermodynamic potential of the system. In this sense they are thermodynamically unfavorable. Their concentration is small and they cannot reach considerable size as the probability of decay is greater than the probability of growth. Thus they have no tendency to unlimited growth and can be considered as *lifeless*. *Frenkel* coined for them the term *homophase fluctuations* to emphasize the fact that they are well compatible with the stable state of aggregation [2.30]. As one approaches the phase equilibrium determined by the equality of the chemical potentials, their concentration increases and the maximum of the size distribution shifts to larger sizes. Once the chemical potential of the initial bulk phase (vapor or solution) becomes greater than that of the new, denser phase (liquid or crystal) the probability of growth becomes greater than the probability of decay and the tendency for growth of the density fluctuations prevails after exceeding some critical size. Frenkel referred to these as *heterophase fluctuations* to stress the fact that they are no longer compatible with the old, less dense phase. It is just these density fluctuations or clusters with a critical size which are called the *nuclei* of the new phase. In order to form such nuclei a free energy should be expended.

Consider a volume containing i_v molecules of a vapor with chemical potential μ_v at constant temperature T and pressure P. The thermodynamic potential of this initial state is given by $G_1 = i_\mathrm{v}\mu_\mathrm{v}$. A small crystal with bulk chemical potential μ_c^∞ is formed from i molecules of the vapor phase and the thermodynamic potential of the final state reads $G_2 = (i_\mathrm{v} - i)\mu_\mathrm{v} + G(i)$, where $G(i)$ is the thermodynamic potential of a cluster consisting of i molecules. The work of formation of a cluster consisting of i molecules is given by the difference $\Delta G(i) = G_2 - G_1$ and [2.31]

$$\Delta G(i) = G(i) - i\mu_\mathrm{v} . \quad (2.20)$$

As seen, the work of formation of the cluster represents the difference between the thermodynamic potential of the cluster and the thermodynamic potential of the same number of molecules but in the ambient phase (vapor, solution or melt). This is the most general definition of the work for nucleation. Taking different expressions for $G(i)$ we can approach different cases of nucleation, such as liquid or crystal nuclei, large or small clusters, clusters with or without equilibrium shape, nuclei on like and unlike surfaces, nuclei formed on small particles or ions, etc.

Equation (2.20) is usually illustrated with the simplest case, when the nucleus is a liquid droplet with the (equilibrium) shape of a sphere with radius r surrounded by its own vapor. We assume that the nucleus is sufficiently large that it can be described by macroscopic thermodynamic quantities. This is in fact the classical or capillary approach introduced by Gibbs. He considered nuclei as small liquid droplets, vapor bubbles or crystallites which, however, are sufficiently large to be described by their bulk properties. Although oversimplified, this approach was a significant step ahead

because, when phases with small linear sizes are involved, the surface-to-volume ratio is large.

The thermodynamic potential of the spherical droplet reads

$$G(r) = \frac{4\pi r^3}{3v_l}\mu_l^\infty + 4\pi r^2\sigma ,$$

where $i = 4\pi r^3/3v_l$ is the number of atoms in the nucleus.

Writing the expression for $G(r)$ in this way we suppose that a cluster with radius r has the chemical potential μ_l^∞ of the infinitely large liquid phase. The second term accounts for the excess energy owing to the newly formed interface between the liquid droplet and the ambient vapor phase, to which we ascribe a specific energy σ that is characteristic of the bulk liquid phase.

The thermodynamic potential of a crystalline cluster with a cubic shape and lateral extent l in the capillary approximation is given by a similar expression

$$G(l) = -\frac{l^3}{v_c}\mu_c^\infty + 6l^2\sigma . \qquad (2.21)$$

Then for the work of nucleus formation in terms of the size l one obtains

$$\Delta G(l) = \frac{l^3}{v_c}\Delta\mu + 6l^2\sigma , \qquad (2.22)$$

where $i = l^3/v_c$, and $\Delta\mu = \mu_v - \mu_c^\infty$ is the supersaturation.

The dependence of $\Delta G(l)$ on the size l is plotted in Fig. 2.6. (Note that the growing cluster preserves its equilibrium shape of a cube with increasing linear size l.) As seen, $\Delta G(l)$ displays a maximum when the ambient phase is supersaturated ($\mu_c^\infty < \mu_v$) at some critical size

$$l^* = \frac{4\sigma v}{\Delta\mu} . \qquad (2.23)$$

In the opposite case of undersaturated vapor ($\mu_c^\infty > \mu_v$) both terms in (2.22) are positive and the Gibbs free energy change goes to infinity as the density fluctuations are thermodynamically unfavorable.

Equation (2.23) is in fact the familiar equation (2.10) of Thomson–Gibbs. As discussed above the latter represents the condition of equilibrium of a small particle with its ambient phase. It is important to note that *this equilibrium is unstable*. When more atoms join the nucleus, its size increases and its equilibrium vapor pressure becomes smaller than that of the ambient phase. As a result the probability of growth becomes greater than the probability of decay and the nucleus

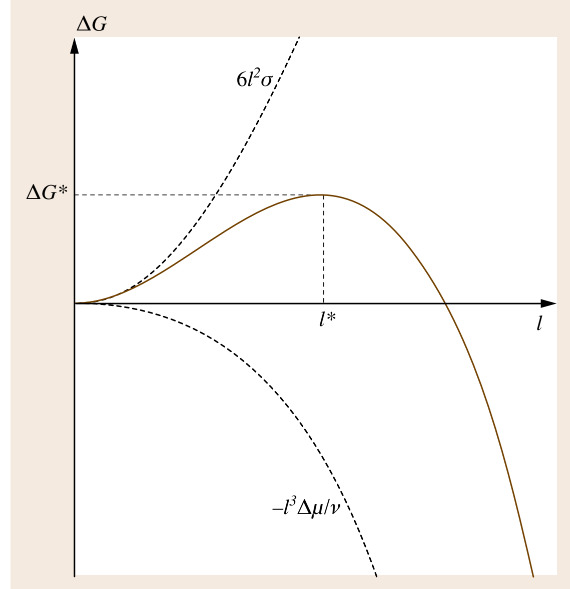

Fig. 2.6 Dependence on the crystal size l (or radius r) of the Gibbs free energy change connected with the formation of a crystalline (liquid) nucleus with a cubic (spherical) shape

will continue to grow. If several atoms detach from the nucleus, its equilibrium vapor pressure will increase and become higher than that of the ambient phase. The probability of decay will become dominant and the nucleus will decay further. In other words, any infinitesimal deviation of the size of the nucleus from the critical one leads to a decrease of the thermodynamical potential of the system.

Substituting l^* into (2.22) gives the value of the maximum, or in other words, the change of the Gibbs free energy to form the nucleus

$$\Delta G^* = \frac{32\sigma^3 v^2}{\Delta\mu^2} . \qquad (2.24)$$

It is inversely proportional to the square of the supersaturation (a result which was obtained for the first time by *Gibbs* in 1878 [2.25]) and increases steeply when approaching the phase equilibrium, thus imposing great difficulties for crystallization to take place.

2.2.2 Formation of 3-D Nuclei on Unlike Substrates

Equation (2.21) gives the thermodynamic potential of a small crystallite with a cubic equilibrium shape whose

properties are described in terms of classical macroscopic thermodynamics. In order to relax this restriction Stranski suggested a new approach which can be used for both large crystals and arbitrarily small clusters with arbitrary shape. The thermodynamic potential is given in the more general form

$$G(i) = i\mu_c^\infty + \Phi \,, \tag{2.25}$$

where Φ plays the role of a surface energy.

The work for nucleus formation then reads

$$\Delta G(i) = -i\Delta\mu + \Phi \,. \tag{2.26}$$

According to the definition of *Stranski* the *surface* term is given by [2.32]

$$\Phi = i\varphi_{1/2} - U_i \,, \tag{2.27}$$

where $U_i > 0$ is the energy of disintegration of the whole crystal (or small cluster) into single atoms. In fact $-U_i$ is the potential (binding) energy of the cluster. In the approximation of additivity of bonds energies, U_i is equal to the number of bonds between the atoms of the cluster multiplied by the work ψ to break a single bond.

Equation (2.27) can be easily understood. The first term on the right-hand side gives the energy of the bonds as if all atoms are in the bulk of the crystal (recall that the separation work from the half-crystal position is equal to the lattice energy per atom). The second term gives the energy of the bonds between the atoms of the cluster. Therefore, the difference represents the number of unsaturated (dangling) bonds multiplied by the energy $\psi/2$ of a dangling bond. Obviously, if the cluster is sufficiently large, Φ can be expressed in terms of surface, edge, and apex energies, but as written above it is applicable to arbitrarily small clusters with arbitrary shape.

Combining (2.26) and (2.27) and substituting for $\Delta\mu$ from the Thomson–Gibbs equation (2.8) in atomistic terms in the resulting equation for the Gibbs free energy change for nucleus formation one obtains

$$\Delta G^* = i^*\bar{\varphi}_3 - U_{i^*} \,. \tag{2.28}$$

We can now calculate the work of formation of a nucleus with equilibrium shape shown in Fig. 2.5. In this case $i = n^2 n'$ and

$$U_i = 3n^2 n'\psi - 2nn'\psi - n^2\psi\phi \,, \tag{2.29}$$

where ϕ is the familiar wetting function (2.17) which determines also the equilibrium shape of a crystal on an unlike substrate.

Combining (2.7), (2.28), and (2.29) gives

$$\Delta G^* = n^{*2}\psi\phi \,, \tag{2.30}$$

where n^* is the number of atoms in the lateral edge of the critical nucleus. Note that $l^* = an^*$ is the length of the edge of the homogeneously formed nucleus in the absence of a substrate or under the condition of complete nonwetting.

We show that (2.30) gives the work of formation of a complete cubic crystallite (2.24) multiplied by the wetting function (2.17), which is positive and smaller than unity in the case of incomplete wetting under study. For this purpose we substitute for n^* and ψ from (2.8) and (2.4), respectively, in (2.30) and obtain ($a^3 = v$)

$$\Delta G^* = \frac{32\sigma^3 v^2}{\Delta\mu^2}\frac{\sigma + \sigma_i - \sigma_s}{2\sigma} \,, \tag{2.31}$$

where the wetting function ϕ is given in terms of surface energies.

It follows that the work for nucleus formation at surfaces (heterogeneous nucleation) is equal to that of the homogeneously formed nuclei in the absence of a surface multiplied by the wetting function. Bearing in mind that

$$\phi = \frac{h}{l} = \frac{l^2 h}{l^3} = \frac{V}{V_0} \,,$$

we conclude that the ratio of the works for heterogeneous and homogeneous nucleation is equal to the ratio of the respective volumes in the presence and absence of a substrate

$$\Delta G^*_{\text{het}} = \Delta G^*_{\text{hom}}\frac{V}{V_0} \,.$$

It is interesting to consider the case when a three-dimensional nucleus is formed in the concave edge of a *hill-and-valley* vicinal surface consisting of alternating low-index facets and which is often formed under the effect of adsorbed impurity atoms [2.33,34]. Assuming for simplicity a right angle of the concave edge we find that the nucleus has a prismatic equilibrium shape, having two edges with length $l' = n'a$ and one edge with a length $l = na$. Using the same procedure as before for ΔG^* one obtains

$$\Delta G^* = n^{*2}\psi\phi^2$$

or

$$\Delta G^* = \frac{32\sigma^3 v^2}{\Delta\mu^2}\left(\frac{\sigma + \sigma_i - \sigma_s}{2\sigma}\right)^2 \,.$$

In the same way we find that the work of formation of a nucleus in a right-angle corner is proportional to the third degree of the wetting function ϕ, etc. As $\phi < 1$ we conclude that a rough surface containing concave edges and corners stimulates nucleation by decreasing the nucleus volume.

2.2.3 Work of Formation of 2-D Crystalline Nuclei on Unlike and Like Substrates

To solve this problem we apply the same procedure, bearing in mind that we have to account for the mean separation work for a two-dimensional square cluster. We consider first the more general case in which the 2-D nucleus is formed on an unlike substrate. Obviously, in order for the 2-D nucleus to be stable the wetting should be complete, although 2-D nuclei can be stable in incomplete wetting but only up to some critical size [2.35]. Beyond this size the monolayer islands become unstable against bilayer islands and should be rearranged into three-dimensional islands as required by the thermodynamics (Sect. 2.6).

The mean separation work calculated for a 2-D square nucleus consisting of $i = n^2$ atoms on unlike substrates reads

$$\bar{\varphi}_2' = 3\psi - \frac{\psi}{n} - \psi\phi$$

and

$$\Delta\mu = \frac{\psi}{n} + \psi\phi \,. \tag{2.32}$$

The binding energy is $U_i = 3n^2\psi - 2n\psi - n^2\psi\phi$ and the Gibbs free energy change reads

$$\Delta G^* = n^*\psi \,. \tag{2.33}$$

Substituting for n^* from (2.32) and ψ from (2.13) in (2.33) gives

$$\Delta G^* = \frac{\psi^2}{\Delta\mu - \psi\phi} = \frac{4\varkappa^2 a^2}{\Delta\mu - a^2(\sigma + \sigma_\mathrm{i} - \sigma_\mathrm{s})} \,. \tag{2.34}$$

In the limiting case of a like substrate (nucleation on the surface of the same crystal) $\Delta\sigma = \sigma + \sigma_\mathrm{i} - \sigma_\mathrm{s} = 0$ and the Gibbs free energy change reads

$$\Delta G^* = \frac{\psi^2}{\Delta\mu} = \frac{4\varkappa^2 a^2}{\Delta\mu} \,. \tag{2.35}$$

Substituting for ψ from the Thomson–Gibbs equation (2.32) in the case of complete wetting, $\phi = 0$, in (2.35) one obtains the very useful result that the work for nucleus formation is precisely equal to the volume part of it

$$\Delta G^* = n^{*2}\Delta\mu = i^*\Delta\mu \,. \tag{2.36}$$

Equations (2.34) and (2.35) lead to some interesting conclusions. In the case of incomplete wetting ($\Delta\sigma > 0$) 2-D nucleation can take place only at supersaturation higher than $\Delta\mu_0 = a^2\Delta\sigma$, because when approaching the latter the work for nucleus formation goes to infinity. In the case of complete wetting ($\Delta\sigma < 0$) both terms in the denominator of (2.34) are positive and 2-D nucleation can take place even at undersaturation. As follows from (2.35) a 2-D nucleation event on the surface of the same crystal ($\Delta\sigma = 0$) can occur only at supersaturations higher than zero.

Equations (2.31) and (2.34) give another critical supersaturation $\Delta\mu_\mathrm{cr} = 2\Delta\mu_0$ at which the 3-D nucleus is reduced to a 2-D nucleus with monolayer height. The reason is that, assuming a constant equilibrium aspect ratio $h/l < 1$, on decreasing the nucleus size with increasing supersaturation a moment comes when the thickness of the 3-D island becomes equal to one monolayer [2.36–38]. As a result three-dimensional nucleation should not take place at supersaturations larger than $\Delta\mu_\mathrm{cr}$. The latter does not contradict the observed layer-by-layer growth of Pb on Ge(001) at 130 K [2.39].

In the end of this subsection we will briefly discuss the very interesting and important question of the existence and formation of one-dimensional nuclei. The latter can be considered as rows of atoms at the edge of a single height step. Using the approach of the mean separation works the equilibrium of a such row of atoms with the ambient phase will be given by the equality of the probabilities of attachment and detachment of atoms to the row's ends. However, the row's ends represent half-crystal positions, so the *mean separation work* reads $\bar{\varphi}_1 = 3\psi = \varphi_{1/2}$ and the supersaturation is $\Delta\mu = \varphi_{1/2} - \bar{\varphi}_1 = 0$. The latter means that a row of atoms has the same chemical potential as the bulk crystal, irrespective of its length. The potential energy of a row consisting of i atoms is $U_i = 3i\psi - \psi$, and the work of formation of a one-dimensional nucleus is $\Delta G_1^* = i\bar{\varphi}_1 - U_i = \psi$. As seen ΔG_1^* does not depend on the row's length, which means that a critical size as in 3-D and 2-D nucleation does not exist. All the above means that one cannot define thermodynamically one-dimensional nuclei. However, as pointed out by several authors, one-dimensional nuclei can be well defined kinetically [2.40–42]. It is in fact the formation of one-dimensional nuclei which allows the propagation of smooth steps, particularly at low temperatures.

We mention here only two cases of great practical importance: the advancement of S_A steps on the surface of Si(001) 2×1 [2.43, 44] and the growth of protein crystals [2.45]. We would like to stress once more that the one-dimensional nucleation is a purely kinetic process and a critical size cannot be defined thermodynamically.

2.3 Rate of Nucleation

As discussed above the equilibrium of a small particle of the new phase with the supersaturated ambient phase is unstable. Accidental detachment of atoms from the critical nucleus can result in a decay of the cluster even to single atoms. Attachment of several atoms could lead to unlimited growth. It is not accidental that the exact solution of the time-dependent problem leads to a diffusion-type equation which reflects the random character of the processes of growth and decay around the critical size [2.30]. We can thus interpret the growth of the clusters as a *diffusion* in the space of the size. We conclude that nucleation is a random process. The steady-state rate of nucleation is a constant quantity which represents an average in time of randomly distributed events.

2.3.1 General Formulation

Becker and *Döring* advanced a purely kinetic approach which allowed them to derive a general expression for the steady-state nucleation rate making the assumptions of: (1) steady-state distribution of the heterophase fluctuations, (2) constant geometrical shape of the growing clusters which coincides with the equilibrium shape, and (3) constant supersaturation which is achieved by removal of clusters which are sufficiently large (much larger than the critical nucleus, $I \gg i^*$) from the system and then are returned back as single atoms [2.46]. The interested reader is referred to the excellent analysis of *Christian* [2.47]. Relaxing assumption 2 did not affect significantly the final result, whereas allowing variable supersaturation changed only the transient character of nucleation but not the steady-state nucleation rate [2.48]. It was in fact the first assumption which played the essential role in solving the problem.

Becker and Döring considered the nucleation process as a series of consecutive bimolecular reactions (a scheme proposed by Leo Szilard)

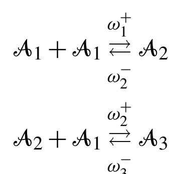

$$\mathcal{A}_1 + \mathcal{A}_1 \underset{\omega_2^-}{\overset{\omega_1^+}{\rightleftarrows}} \mathcal{A}_2$$

$$\mathcal{A}_2 + \mathcal{A}_1 \underset{\omega_3^-}{\overset{\omega_2^+}{\rightleftarrows}} \mathcal{A}_3$$

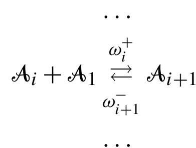

$$\cdots$$

$$\mathcal{A}_i + \mathcal{A}_1 \underset{\omega_{i+1}^-}{\overset{\omega_i^+}{\rightleftarrows}} \mathcal{A}_{i+1}$$

$$\cdots$$

in which the growth and decay of the clusters take place by attachment and detachment of single atoms. Triple and multiple collisions are excluded as less probable. ω_i^+ and ω_i^- denote the rate constants of the direct and reverse reactions. Here $\mathcal{A}$ is used as a chemical symbol.

Clusters consisting of i atoms are formed by the growth of clusters consisting of $i-1$ atoms and the decay of clusters of $i+1$ atoms (birth processes) and disappear by the growth and decay into clusters of $i+1$ and $i-1$ atoms (death processes), respectively. Then the change with time of the concentration $Z_i(t)$ of clusters consisting of i atoms is given by

$$\frac{\mathrm{d}Z_i(t)}{\mathrm{d}t} = J_i(t) - J_{i+1}(t) ,$$

where

$$J_i(t) = \omega_{i-1}^+ Z_{i-1}(t) - \omega_i^- Z_i(t) \tag{2.37}$$

is the net flux of clusters through the size i.

Assuming a steady-state concentration of the clusters in the system, $\mathrm{d}Z_i(t)/\mathrm{d}t = 0$, leads to

$$J_i(t) = J_{i+1}(t) = J_0 ,$$

where we denote by J_0 the time-averaged frequency of formation of clusters of any size. Therefore, J_0 is also equal to the frequency of formation of the clusters with the critical size i^* and thus is equal to the steady-state nucleation rate.

Applying a simple mathematical procedure to the system of rate equations which describe the scheme of Szilard for J_0 one obtains [2.49]

$$J_0 = Z_1 \sum_{i=1}^{I-1} \left(\frac{1}{\omega_i^+} \frac{\omega_2^- \omega_3^- \ldots \omega_i^-}{\omega_1^+ \omega_2^+ \ldots \omega_{i-1}^+} \right)^{-1} . \tag{2.38}$$

This is the most general expression for the steady-state rate of nucleation. It is applicable to any case of nucleation (homogeneous or heterogeneous, from

any ambient phase – vapor, solution or melt, three- or two-dimensional, etc.). It also allows the derivation of equations for the classical as well as the atomistic nucleation rate at small and high supersaturations as limiting cases. The only thing we should know in any particular case are the rate constants ω_i^+ and ω_i^-.

The analysis of (2.38) shows that every term in the sum is equal to $\exp(\Delta G(i)/k_B T)$, where $\Delta G(i)$ is the work to form a cluster consisting of i atoms [2.50]

$$\frac{\omega_2^- \omega_3^- \ldots \omega_i^-}{\omega_1^+ \omega_2^+ \ldots \omega_{i-1}^+} = \exp\left(\frac{\Delta G(i)}{k_B T}\right) . \tag{2.39}$$

The condition of an imaginary equilibrium $J_0 = 0$ applied to (2.37) leads to an equation known in the literature as the equation of *detailed balance*

$$\frac{N_i}{N_{i-1}} = \frac{\omega_{i-1}^+}{\omega_i^-} ,$$

where N_i denotes the equilibrium concentration of clusters consisting of i atoms. Multiplying the ratios N_i/N_{i-1} from $i = 2$ to i gives an expression for the equilibrium concentration of clusters of size i

$$\frac{N_i}{N_1} = \prod_{n=2}^{i} \left(\frac{\omega_{n-1}^+}{\omega_n^-}\right) = \left(\frac{\omega_2^- \omega_3^- \ldots \omega_i^-}{\omega_1^+ \omega_2^+ \ldots \omega_{i-1}^+}\right)^{-1} . \tag{2.40}$$

Substituting (2.39) into (2.40) gives for the *equilibrium concentration of clusters of size i*

$$N_i = N_1 \exp\left(-\frac{\Delta G(i)}{k_B T}\right) . \tag{2.41}$$

We recall that $\Delta G(i)$ displays a maximum at $i = i^*$. It follows that N_i should display a minimum at the critical size.

Substituting (2.39) into (2.38) and replacing the summation by integration valid for large critical nuclei one obtains

$$J_0 = \omega^* \Gamma N_{i^*} ,$$

where $\omega^* \equiv \omega_{i^*}$ is the frequency of attachment of atoms to the critical nucleus, $\Gamma = (\Delta G^*/3\pi k_B T i^{*2})^{1/2}$ is the so-called nonequilibrium Zeldovich factor which accounts for neglecting processes taking place far from the critical size, and N_{i^*} is given by (2.41) for the critical nucleus. It is assumed that the equilibrium monomer concentration N_1 is equal to the steady-state concentration Z_1.

In the particular case of nucleation on surfaces we have to account for the configurational entropy of distribution of clusters and single atoms among the adsorption sites of density N_0 ($\approx 1 \times 10^{15}\,\text{cm}^{-2}$) which should be added to the Gibbs free energy changes (2.31), (2.34) or (2.35) [2.51]. Assuming that the density of clusters is negligible compared with that of single atoms the entropy correction reads

$$\Delta G_{\text{conf}} \approx -k_B T \ln\left(\frac{N_0}{N_1}\right) .$$

Then for the steady-state nucleation rate on surfaces one obtains

$$J_0 = \omega^* \Gamma N_0 \exp\left(-\frac{\Delta G^*}{k_B T}\right) , \tag{2.42}$$

where the frequency of attachment of atoms to the critical nucleus ω^* accounts only for the surface diffusion of atoms to the nucleus, the direct impingement from the vapor being neglected [2.52].

As discussed above the capillary nucleation theory is valid at supersaturations which are sufficiently low that the nuclei are large and can be described in terms of the classical thermodynamics. In order to find the limits of validity of (2.42), or in other words, the maximum value of the supersaturation at which the above equation is still valid, we have to find the values of the pre-exponential $K = \omega^* \Gamma N_0$ and ΔG^* and calculate the time τ elapsed from *switching on* the supersaturation to the appearance of the first nucleus. The latter is given by $\tau = 1/J_0 S$, where S is the area available for nucleation.

Consider for simplicity 2-D nucleation on the surface of the same crystal. The frequency of attachment of atoms to the critical nucleus ω^* is given by the product of the periphery of the nucleus and the flux of adatoms joining the nucleus. We assume that the nucleus consists of at least 49 atoms (a square of 7×7 atoms) in order for the classical theory to be valid. The flux of adatoms to the periphery is $j_s \approx D_s N_1/a$, where $D_s = a^2 \nu \exp(-E_{sd}/k_B T)$ is the surface diffusion coefficient, and the adatom concentration is determined by a dynamic adsorption–desorption equilibrium and is given by $N_1 = R\tau_s$. The reason for using this definition is that it is supposed that the temperature is sufficiently high to ensure low supersaturation and the desorption flux N_1/τ_s is significant. Here ν is the attempt frequency and E_{sd} and E_{des} are the activation barriers for surface diffusion and desorption, respectively. Taking appropriate values for the parameters involved we find a value for the pre-exponential of the order of 10^{20}–$10^{25}\,\text{cm}^{-2}\,\text{s}^{-1}$ for nucleation from vapor. We can further evaluate the supersaturation by using (2.11).

Once we know the supersaturation we can easily evaluate ΔG^* by making use of (2.36).

We consider as an example nucleation on Si(001) at $T = 1500\,\mathrm{K}$ and assume that $S = 1\,\mathrm{cm}^2$, although a more realistic value could be determined from the width of the terraces on the crystal surface. From the enthalpy of evaporation we deduce the bond strength to be of the order of 2–2.2 eV. Then $\Delta\mu \approx 0.3\,\mathrm{eV}$, $\Delta G^* = 15\,\mathrm{eV}$, and $\tau \approx 1 \times 10^{15}$ millennia. This behavior of the classical nucleation rate was noticed by *Dash*, who noted that nucleation on defectless crystal surfaces according to the classical theory requires *astronomically* long times [2.53]. The reason for this behavior is that the pre-exponential in J_0 is a very weak function of the supersaturation compared with the exponential $\exp(-\Delta G^*/k_\mathrm{B}T)$, which varies very steeply with the latter. As a result there is a critical supersaturation below which the rate of nucleation is practically equal to zero and beyond which it takes values of many orders of magnitude (Fig. 2.7). We conclude that, in order for a nucleation event to take place on a laboratory scale of time, $\Delta G^*/k_\mathrm{B}T$ should be smaller than ≈ 30 (in the case under consideration it is 4 times larger). This means that, for most materials at working temperatures between 600 and 1000 K, *the number of atoms in the critical nucleus should be of the order of unity*. This is why we will develop in more detail the atomistic theory of nucleation valid for nuclei consisting of very small number of atoms. It is important to note that a small value (usually not larger than ten) of the number of atoms in the critical nucleus should be expected also in the case of three-dimensional nucleation. A value of $i^* = 9$ was obtained in the case of nucleation of $CoSi_2$ from amorphous Co-Si alloy [2.54]. The reason for the comparatively larger size is due to the much greater value of the pre-exponential, which in this particular case is on the order of 10^{35}–$10^{40}\,\mathrm{cm}^{-3}\,\mathrm{s}^{-1}$ [2.21].

Fig. 2.7 Plot of the nucleation rate versus the supersaturation. The nucleation rate is practically equal to zero up to a critical supersaturation $\Delta\mu_c$. Beyond this value the rate of nucleation increases sharply by many orders of magnitude

2.3.2 Rate of Nucleation on Single-Crystal Surfaces

Single-crystal surfaces always represent vicinal surfaces consisting of terraces divided by steps due to the tilt of the surface by some small angle with respect to the low-index (singular) crystal face. Numerous processes can take place during deposition on the terraces (Fig. 2.8). We consider first the case of complete wetting. Atoms arrive from the vapor and accommodate thermally with the substrate [2.55], diffuse on the crystal surface, and re-evaporate if the temperature is sufficiently high. The atoms can also join pre-existing steps and diffuse along these steps to incorporate into kink sites. The reverse process of detachment of atoms from kink sites directly to the terrace or through the intermediate state of adsorption at the step edge can also take place. Thus when the temperature is sufficiently high the crystal grows by propagation of the pre-existing steps. If the temperature is low and the atom diffusivity is small the atoms cannot reach the steps and collide with other atoms to produce dimers. The dimers can grow further to produce trimers, tetramers, and finally large islands by attachment of new adatoms, or can decay into single atoms. Arriving atoms will preferably join the islands in a later stage of growth, the formation of new dimers being inhibited. Thus we can distinguish two

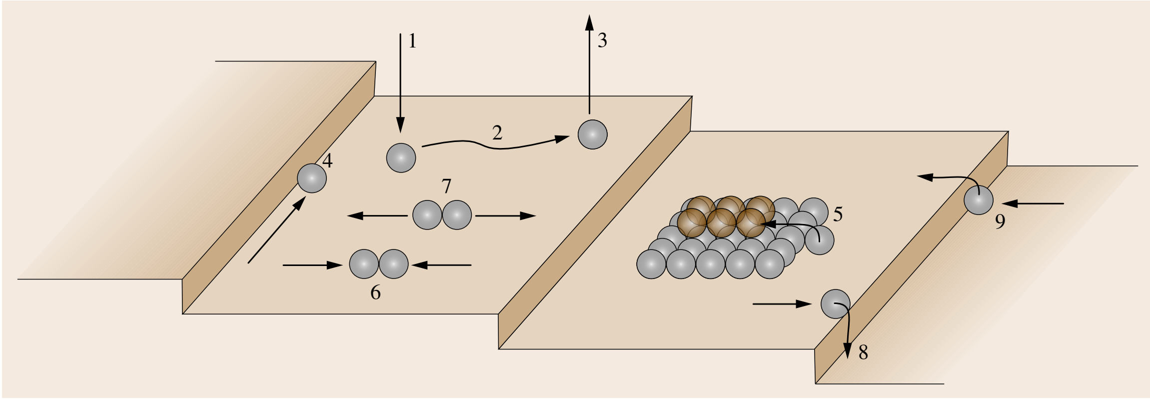

Fig. 2.8 Schematic representation of the different processes which can take place on surfaces during deposition on like and unlike substrates: 1 – adsorption, 2 – surface diffusion, 3 – desorption, 4 – edge diffusion, 5 – transformation of monolayer to bilayer island in heteroepitaxy, 6 – dimer formation, 7 – dimer decay, 8 – step-down hopping, 9 – step-up jump

regimes of growth: step flow growth at high temperatures and growth by two-dimensional nucleation at low temperatures.

In the case of incomplete wetting which favors three-dimensional clustering all the processes listed above remain the same with the exception that step flow growth does not take place (we consider the case of heteroepitaxy with $\psi > \psi'$); nucleation occurs at all temperatures. The mechanism of formation of 3-D clusters depends strongly on the wetting. In the extreme of very weak wetting (metals on alkali halides) visible clustering is observed from the very beginning of deposition. When the wetting is stronger as in the technologically important cases of metals on metals or semiconductors on semiconductors, two-dimensional islands are initially energetically favored but become unstable and transform beyond some critical size into 3-D clusters (Fig. 2.8) [2.35]. The same is observed in Stranski–Krastanov growth beyond the wetting layer [2.56, 57]. Thus in the beginning of deposition the overlayer can be considered as a population of molecules of different size, most of which are one atom high [2.58].

2.3.3 Equilibrium Size Distribution of Clusters

We calculate first the equilibrium concentration of the clusters of size i. The thermodynamic potential of the cluster of size i is given by (2.25), where i is an integer which can be arbitrarily small. Bearing in mind (2.26) and (2.27) the work for nucleus formation reads

$$\Delta G(i) = G(i) - i\mu_v = i(\varphi_{1/2} - \Delta\mu) - U_i \ . \quad (2.43)$$

Assuming the adlayer consisting of clusters of different size behaves as a two-dimensional ideal gas ($\sum_i N_i \ll N_0$) the thermodynamic potential of the population of clusters of size i will be [2.59]

$$\mathcal{G}(N_i) = N_i G(i) - k_B T \ln \frac{N_0!}{(N_0 - N_i)!N_i!} \ .$$

Then for the chemical potential of the two-dimensional ideal gas of clusters of size i one obtains

$$\mu_i = \frac{d\mathcal{G}(N_i)}{dN_i} = G(i) - k_B T \ln\left(\frac{N_0}{N_i}\right) . \quad (2.44)$$

Suppose now that the pressure of the vapor is precisely equal to the equilibrium vapor pressure of the infinitely large crystal at the given temperature so that $\mu_i = i\mu_c^\infty$. The system is in a true equilibrium and the nucleation rate is precisely equal to zero. Rearranging (2.44) and inserting the above equality gives for the equilibrium concentration of i-atomic clusters

$$\frac{N_i^e}{N_0} = \exp\left(-\frac{G(i) - i\mu_c^\infty}{k_B T}\right) .$$

Assume now that the vapor pressure is higher than the equilibrium vapor pressure so that $\mu_i = i\mu_v > i\mu_c^\infty$. The system will be supersaturated and the nucleation rate will differ from zero. We apply as before the artificial condition $J_0 = 0$, which determines a hypothetical equilibrium concentration of clusters of size i

$$\frac{N_i}{N_0} = \exp\left(-\frac{G(i) - i\mu_v}{k_B T}\right) .$$

Substituting for $G(i)$ from (2.43) in the above equation gives

$$\frac{N_i}{N_0} = \exp\left(-\frac{i\varphi_{1/2} - i\Delta\mu - U_i}{k_B T}\right) . \quad (2.45)$$

The condition $i = 1$ yields the density of monomers

$$\frac{N_1}{N_0} = \exp\left(-\frac{\varphi_{1/2} - \Delta\mu - U_1}{k_B T}\right) ,$$

the i-th power of which reads

$$\left(\frac{N_1}{N_0}\right)^i = \exp\left(-\frac{i\varphi_{1/2} - i\Delta\mu - iU_1}{k_B T}\right) . \quad (2.46)$$

Dividing (2.45) and (2.46) gives for this hypothetical equilibrium concentration of clusters of size i [2.58]

$$\frac{N_i}{N_0} = \left(\frac{N_1}{N_0}\right)^i \exp\left(\frac{E_i}{k_B T}\right) , \quad (2.47)$$

where $E_i = U_i - iU_1$ is the net energy gained to form an i-atom cluster from i single atoms. Bearing in mind that U_1 is, in fact, the adhesion energy ψ', E_i is the potential (binding) energy of the lateral bonds in the cluster. The latter means that the value of E_i does not depend (within the framework of the approximation of the additivity of the bond energies) on the material of the substrate. It should be one and the same on like and unlike substrate crystals. Recall that we defined U_i as a positive quantity. This means that E_i is also positive. As $N_1/N_0 \ll 1$ the pre-exponential decreases whereas the exponential increases with i. It follows that (2.47) should display a minimum at some critical size or, in other words, will have the same qualitative behavior as the classical equilibrium size distribution (2.41).

2.3.4 Rate of Nucleation

An approximate expression for the nucleation rate can be obtained by multiplying (2.47) by the flux of atoms to the critical nucleus. Note, however, that in the case of small clusters the classical definition of a nucleus as a cluster with equal probabilities for growth and decay, each one equal to 0.5, is not valid. The nucleus should be defined as the cluster whose probability of growth is smaller than or equal to 0.5, but which after attachment of one more atom will have a probability of growth greater than or equal to 0.5 [2.58]. The latter is called the *smallest stable cluster*. Thus the nucleation rate is the rate at which clusters of critical size become *supercritical* or smallest stable clusters.

It is clear that for small clusters the requirement of constant geometrical shape required by the classical theory is violated. An analytical expression for i^* cannot be derived and the nucleus structure should be determined by a trial-and-error procedure by estimating the binding energy of the different configurations including the possibility of formation of three-dimensional structures. Let us consider as an example the formation of nuclei on the (111) surface of a face-centered cubic (fcc) metal (Fig. 2.9). At $\Delta\mu = 3.25\psi$ the critical nucleus consists of two atoms and the smallest stable cluster consists of three atoms (Fig. 2.10). The work required to decay the nucleus is equal to the work to break a single first-neighbor bond, whereas in order to detach an atom from the smallest stable cluster we have to break simultaneously two first-neighbor bonds. This means that the latter will be much more stable than the nucleus and a higher temperature is required to decay the three-atom cluster. The attachment of additional atoms up to $i = 6$ does not change the stability of the respective clusters. Then at $\Delta\mu = 2.75\psi$ the nucleus consists of six atoms and the smallest stable cluster represents

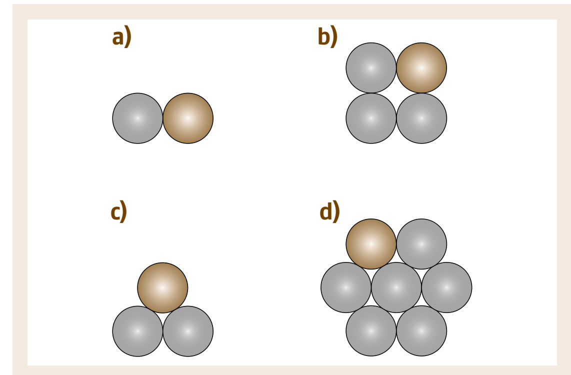

Fig. 2.9a–d Two-dimensional clusters on (001) and (111) surfaces of a crystal with a face-centered cubic lattice. The structure of the nuclei is given by the *gray circles*. The *black circles* denote the atoms that turn the critical nuclei into smallest stable clusters. **(a)** The nucleus consists of a single atom; the stable supercritical cluster is a dimer, which requires a single bond to be broken in order to decay. In **(b)** the nucleus consists of three atoms situated on the apexes of a rectangular triangle on (001) surface; the smallest stable cluster has a square shape. The decay of the latter requires the simultaneous breaking of two bonds. On (111) surface the nuclei consist of **(a)** one, **(c)** two, and **(d)** six atoms. The corresponding stable clusters consist of two, three, and seven atoms, respectively, which require breaking of one, two, and three bonds

a closed structure consisting of a complete ring of six atoms plus an atom in the middle. In order to detach an atom from the smallest stable cluster we have to break simultaneously three first-neighbor bonds. Obviously, such a cluster will be stable at much higher temperatures than a three-atom cluster.

Bearing in mind that every term in the sum of (2.38) is equal to $\exp(\Delta G(i)/k_BT)$ we study the behavior of the latter for small values of i (Fig. 2.10). It is seen that at extremely high supersaturations (low temperatures) $\Delta G(i)$ and $\exp(\Delta G(i)/k_BT)$ are represented by broken curves whereas at low supersaturations (large nuclei) the curve is smooth. Contrary to the classical case where the clusters in the vicinity of the critical size have values of $\exp(\Delta G(i)/k_BT)$ close to that of the nucleus, in the case of small clusters the contribution of $\exp(\Delta G(i^*)/k_BT)$ of the critical nucleus is the largest, all other terms in the sum of the denominator being negligible. Thus, instead of summing all the terms as in the classical theory, we can take the largest term and neglect all the others. For this purpose we write (2.38) in the form

$$J_0 = \omega_1^+ N_1 \left(1 + \frac{\omega_2^-}{\omega_2^+} + \frac{\omega_2^-\omega_3^-}{\omega_2^+\omega_3^+} + \frac{\omega_2^-\omega_3^-\omega_4^-}{\omega_2^+\omega_3^+\omega_4^+} + \ldots\right)^{-1} \quad (2.48)$$

and calculate the rate constants for the birth and death processes.

By analogy with the classical theory, where $\omega_i^+ \approx (P_i/a)D_sN_1$, P_i being the perimeter of the nucleus and P_i/a the number of the dangling bonds, in the atomistic approach [2.60]

$$\omega_i^+ = \alpha_i D_s N_1 ,$$

where α_i is the number of ways of attachment of an atom to a cluster of size i to produce a cluster of size $i+1$. Obviously, this parameter is proportional to the number of dangling bonds.

The decay constant reads

$$\omega_i^- = \beta_i \nu \exp\left(-\frac{E_i - E_{i-1} + E_{sd}}{k_BT}\right) , \quad (2.49)$$

where E_i is the work to disintegrate a cluster of size i into single atoms, and $E_i - E_{i-1}$ is the work required to detach an atom from the cluster of size i. β_i is the number of ways of detachment of an atom from a cluster of size i. It is easy to show that there exists a one-to-one correspondence between the growth ($i \to i+1$) and decay ($i+1 \to i$) processes so that

$$\alpha_i = \beta_{i+1} .$$

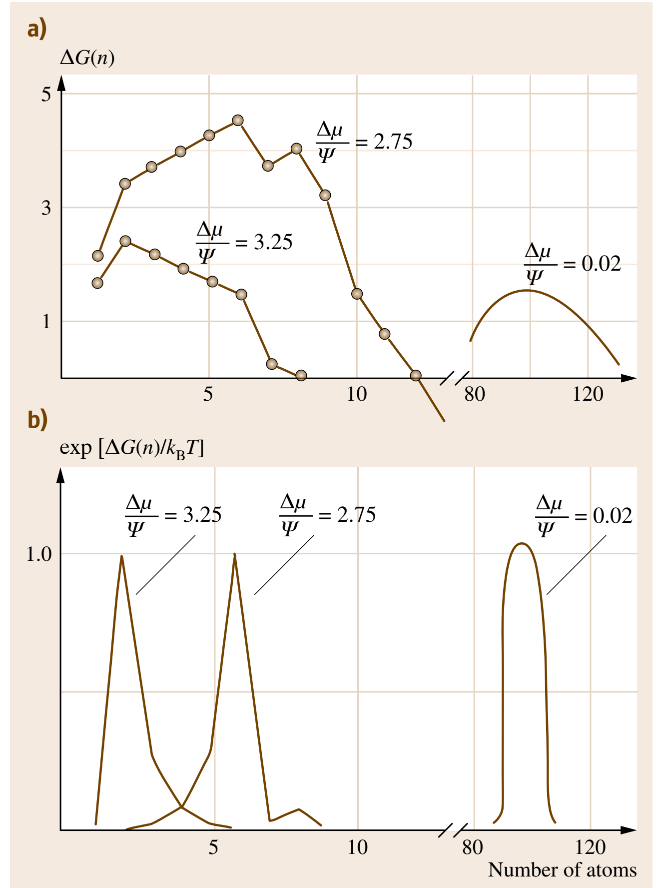

Fig. 2.10a,b Dependence of **(a)** the Gibbs free energy change $\Delta G(i)/\psi$ in units of the work ψ required to break a first-neighbor bond, and **(b)** $\exp(\Delta G(i)/k_BT)$ on the number of atoms i in the cluster at different values of the supersaturation. At small supersaturation ($\Delta\mu = 0.02\psi$) the cluster is large, the respective curves are smooth, and the summation can be replaced by integration. At very large supersaturations the curves are broken and the contribution of the critical nucleus is dominant

Recalling the expression for the diffusion coefficient $D_s = a^2\nu\exp(-E_{sd}/k_BT)$ we can write (2.49) in the form

$$\omega_i^- = \beta_i D_s N_0 \exp\left(-\frac{E_i - E_{i-1}}{k_BT}\right) ,$$

where $N_0 \cong a^{-2}$.

The assumption that all terms in the denominator in (2.48) are smaller than unity means that $i^* = 1$

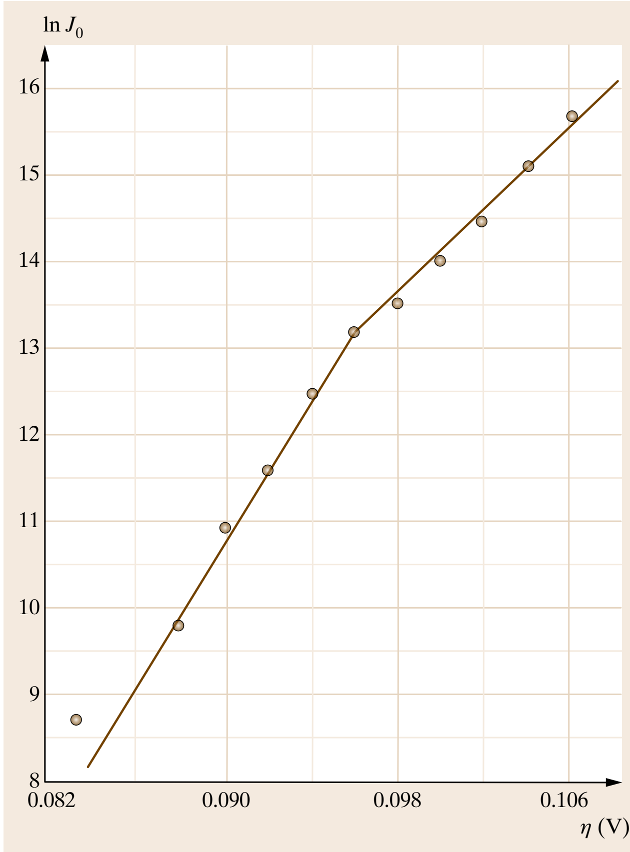

Fig. 2.11 Experimental data for the nucleation rate as a function of the overpotential η in the case of electrochemical nucleation of mercury on platinum single-crystal spheres (after [2.61]), in atomistic coordinates ln $J_0 - \eta$, according to [2.62]. The number of atoms in the critical nucleus changes at about 0.096 V

($E_1 = 0$) and

$$J_0 = \omega_1^+ N_1 = \alpha_1 D_s N_1^2 .$$

Assuming that the adatom concentration is determined by a dynamic adsorption–desorption equilibrium $N_1 = R\tau_s$ as before, for J_0 one obtains

$$J_0 = \alpha_1 \frac{R^2}{N_0 \nu} \exp\left(\frac{2E_{des} - E_{sd}}{k_B T}\right) .$$

When the ratio ω_2^- / ω_2^+ is the largest term in the denominator of (2.48), $i^* = 2$ and

$$J_0 = \omega_1^+ N_1 \frac{\omega_2^+}{\omega_2^-} = \alpha_2 D_s^2 N_1^3 \nu^{-1} \exp\left(\frac{E_2 + E_{sd}}{k_B T}\right)$$

or

$$J_0 = \alpha_2 \frac{R^3}{N_0^2 \nu^2} \exp\left(\frac{E_2 + 3E_{des} - E_{sd}}{k_B T}\right) .$$

In the general case

$$J_0 = \alpha^* R \left(\frac{R}{N_0 \nu}\right)^{i^*} \times \exp\left(\frac{E_{i^*} + (i^*+1)E_{des} - E_{sd}}{k_B T}\right) .$$

Very often the process of re-evaporation is negligible (complete condensation) and $N_1 \neq R\tau_s$. Then we can write J_0 in terms of the adatom concentration in the form

$$J_0 = \alpha^* D_s \frac{N_1^{i^*+1}}{N_0^{i^*-1}} \exp\left(\frac{E_{i^*}}{k_B T}\right) , \qquad (2.50)$$

which is very useful for solving various nucleation problems.

Whereas the attachment or detachment of atoms to and from a comparatively large liquid droplet or crystallite can be considered as a good approximation to a continuous process, this is impossible when the cluster consists of several atoms. In this case the general principles of the thermodynamics are violated, the best example of which is that the Thomson–Gibbs equation is not valid in its familiar form (2.10). The reason becomes obvious if we write it in terms of the number of atoms rather than the linear size of the crystallite

$$\frac{P_i}{P_\infty} = \exp\left(\frac{4\sigma v^{2/3}}{k_B T i^{1/3}}\right) .$$

It is immediately seen that the vapor pressure in the left-hand side of the equation can be continuously varied whereas the right-hand side is a discrete function of the cluster size i. The latter means that to any particular size of the cluster corresponds a fixed value of the vapor pressure, but the opposite is not true; an integer number of atoms does not correspond to any arbitrary value of the vapor pressure. It follows that, contrary to the classical concept, a cluster with an integer number of atoms is stable in an interval of supersaturation (or vapor pressure) which becomes larger as the cluster size becomes smaller [2.63]. This interval is equal to $P_i - P_{i+1}$, where P_i is the fixed value of the vapor pressure corresponding to a cluster consisting of i atoms.

Substituting for ΔG^* from (2.26) with $i = i^*$ in (2.42) gives

$$J_0 = \omega^* \Gamma N_0 \exp\left(-\frac{\Phi}{k_B T}\right) \exp\left(i^* \frac{\Delta\mu}{k_B T}\right) .$$

As the shape does not change at constant number of atoms the *surface* part Φ remains constant in the interval of stability of a given cluster size. Then the logarithm of the nucleation rate as a function of the supersaturation will represent a broken line when the supersaturation interval is sufficiently wide to cover the intervals of several cluster sizes. The slopes of the consecutive straight line parts will be equal to the respective number of atoms i^* of the critical nuclei. This is shown in Fig. 2.11, which represents experimental data for the nucleation rate in electrodeposition of mercury on platinum single-crystal spheres [2.61], interpreted in terms of the atomistic theory in [2.62] (see also [2.64]). The values $i^* = 6$ and 10 have been found from the slopes of the two parts of the plot. A clear evidence for a transition from $i^* = 1$ to $i^* = 3$ has been reported by *Müller* et al. in the case of nucleation of Cu on Ni(001) [2.65]. Thus a single nucleus size is operative over a temperature (supersaturation) interval. The slopes of the consecutive intervals give a distinct series of consecutive numbers of atoms which depend on the crystallographic orientation of the substrate. Thus in the case of nucleation of (001) surface of fcc metals the numbers are one and three, whereas on (111) surface the numbers are one, two, and six. The corresponding smallest stable clusters ($i^* + 1 = 2, 3, 7$ on the fcc(111) surface) are often referred to as *magic* in the literature. The physics behind this magic is simple. In order to detach an atom from the corresponding smallest stable clusters we have to break simultaneously one, two or three bonds.

2.4 Saturation Nucleus Density

Measurements of the nucleus density as a function of time show that, after sufficiently long time, the nucleus density saturates; this means that the nucleation process ceases. Numerous factors can be responsible for this phenomenon. Preferred nucleation on defect sites, overlapping of zones with reduced supersaturation around growing islands, coalescence of neighboring islands, and growth of larger islands at the expense of smaller ones owing to the Thomson–Gibbs effect (Ostwald ripening) take place most frequently and are most studied [2.66].

Although the preparation of defectless single crystals is already a routine procedure, the complete absence of impurity particles, stacking faults, twin boundaries, emerging points of dislocations, etc. cannot be achieved. It is this presence of defects on the crystal surface which is one of the reasons for the observation of saturation of the nucleus density with time and this was the first to be studied. The defects represents sites on the crystal surface which stimulate nucleation by stronger wetting. Assume for simplicity that they have equal activity (wetting function). Nuclei can form on free active sites whose number is $N_\mathrm{d} - N$ with a frequency J_0' per site, N_d being the total number of active sites. Then the change with time t of the nucleus density reads [2.67]

$$\frac{\mathrm{d}N}{\mathrm{d}t} = J_0'(N_\mathrm{d} - N) \,.$$

Integration subject to the initial condition $N(0) = 0$ results in a simple exponential function

$$N(t) = N_\mathrm{d}\left[1 - \exp\left(-J_0't\right)\right] \,,$$

which tends with time to a saturation value equal to N_d. In the more realistic case of a certain activity distribution of the sites, increasing supersaturation will lead to inclusion of less-active sites in the process and increase of the saturation nucleus density [2.68].

Another reason for saturation of the nucleus density is the appearance of *locally undersaturated* zones around growing nuclei where the nucleation rate is reduced or even equal to zero owing to the consumption of the diffusing adatoms [2.69–71]. *Sigsbee* coined for these zones the term *nucleation exclusion zones* [2.72]. They are also known as *denuded* or *depleted* zones. Nuclei and in turn denuded zones around them are progressively formed and grow during film deposition. When the zones overlap and cover the whole substrate surface the process of nucleation is arrested and saturation of the nucleus density is reached. The radii of the nucleation exclusion zones are defined by the intersection of the gradient of the adatom concentration around the growing island and the critical adatom concentration (or supersaturation) for nucleation to occur (Fig. 2.12). A typical nucleation exclusion zone around a mercury droplet electrodeposited on a platinum single-crystal sphere is shown in Fig. 2.13 [2.73].

The problem of finding the nucleus density when the latter is limited by nucleation exclusion zones has been treated by many authors, such as *Kolmogorov*, *Avrami*, and *Johnson* and *Mehl*, and solutions for different cases have been found [2.74–78] (for a review see [2.47]). The simultaneous influence of both nucleation exclusion zones and active sites has also been

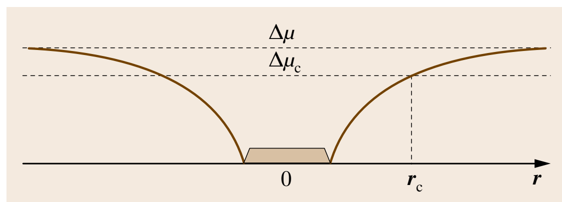

Fig. 2.12 The definition of nucleation exclusion zones. The radius of the latter is determined by the intersection of the gradient of the supersaturation and the critical supersaturation for noticeable nucleation to occur. Because of the very steep dependence of the nucleation rate on the supersaturation (Fig. 2.7) the nucleation rate inside the zone is assumed equal to zero

addressed [2.79,80]. The problem consists of finding the area $\Theta(t)$ uncovered by depleted zones and thus available for nucleation at a moment t. The number of nuclei is then given by

$$N = J_0 \int_0^t \Theta(\tau)\,\mathrm{d}\tau \,.$$

The area $1-\Theta(t)$ represents the sum of all nucleation exclusion zones accounting for the area where neighboring zones have overlapped. The latter is equal to the probability of finding an arbitrary point simultaneously in two or more nucleation exclusion zones [2.74]. Assuming that nuclei are formed on randomly distributed sites with a rate J_0 and that the zones grow with a velocity $v(t) = ck(t)$ the area $\Theta(t)$ is given by [2.74]

$$\Theta(t) = \exp\left(-J_0 \int_0^t S'(t')\,\mathrm{d}t'\right) \,,$$

where

$$S'(t', t) = \pi c^2 \left(\int_{t'}^t k(\tau - t')\,\mathrm{d}\tau\right)^2$$

is the area of a nucleation exclusion zone at a moment t around a nucleus formed at a moment $t' < t$.

Assuming linear growth of the zones ($k(t) = 1$) gives for the nucleus density as a function of time

$$N(t) = J_0 \int_0^t \exp\left(-\frac{\pi}{3} J_0 c^2 t^3\right) \mathrm{d}t \,. \tag{2.51}$$

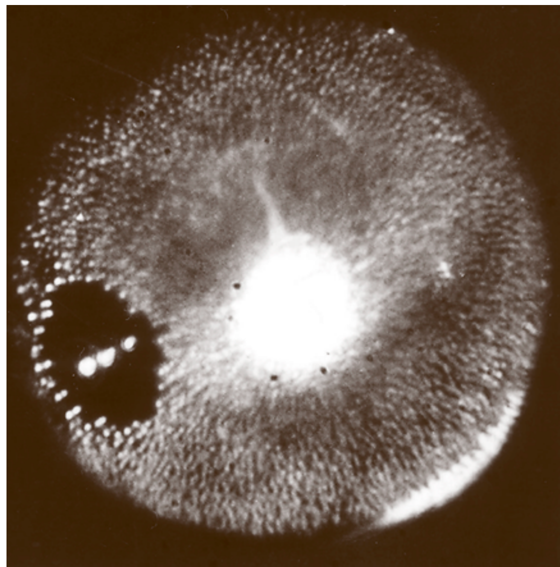

Fig. 2.13 Nucleation exclusion zone around a mercury droplet electrodeposited on a platinum single-crystal sphere. The droplet is practically invisible. Instead, three light reflections from the illuminating lamp are visible. The mercury droplet has been deposited by applying a short electric pulse followed by a lower overpotential in order to grow it to a predetermined size. Then a high electric pulse is applied to cover the whole surface with mercury with the exception of the area around the droplet (after [2.73])

The saturation nucleus density is obtained under the condition $t \to \infty$. Integrating (2.51) from zero to infinity gives

$$N_{\mathrm{sat}} \cong 0.9 \left(\frac{J_0}{c}\right)^{2/3} \,.$$

Another approach was later developed, particularly for nucleation at surfaces, by using a system of kinetic rate equations. It was first introduced by Zinsmeister as a system of equations for the change with time of the concentrations of clusters $\mathrm{d}N_i/\mathrm{d}t$ ($i = 1, 2, 3, \ldots$) for each cluster size, beginning with that of single adatoms [2.81–84]. All birth and death processes were accounted for in $\mathrm{d}N_i/\mathrm{d}t$. In addition, the atom arrival rate and re-evaporation were taken into account in the equation of change of the monomers $\mathrm{d}N_1/\mathrm{d}t$. In order to solve quantitatively the above system of equations the attachment and detachment frequencies had to be determined. As a result a large amount of papers have been devoted to further elaborating the approach [2.85–92]. In the limit $i^* = 1$ (*irreversible aggregation*) the

detachment frequencies are equal to zero. The attachment frequencies (capture numbers) were considered by using different approximations, beginning from the mean-field approximation by assuming that the clusters are immersed and grow in a dilute adlayer with an average concentration that does not depend on the location of the clusters, to solutions of diffusion equation around the growing islands in terms of Bessel functions. The system was later greatly simplified by *Venables* et al. to a system of two equations which were sufficient to illustrate the essential physics [2.93].

We consider first the case of irreversible aggregation. The dimers are assumed to be stable (a third atom joins the dimer before the latter to decay) and immobile. The atoms arrive at the crystal surface, diffuse on it, and collide with each other to produce dimers. Atoms join the dimers and larger clusters upon striking without any obstacle of kinetic origin. This means that the growth of clusters is limited only by the surface diffusion. Coalescence of immobile clusters is ruled out. The detachment frequencies are equal to zero and the capture numbers are omitted for simplicity as they represent figures of the order of unity [2.93]. The system of equations is then reduced to

$$\frac{\mathrm{d}N_1}{\mathrm{d}t} = F - 2DN_1^2 - DN_1N_\mathrm{s}\,, \tag{2.52a}$$

$$\frac{\mathrm{d}N_\mathrm{s}}{\mathrm{d}t} = DN_1^2\,, \tag{2.52b}$$

where $F = R/N_0$ is the atom arrival rate in units of number of monolayers, $D = D_\mathrm{s}/a^2 = \nu\exp(-E_\mathrm{sd}/k_\mathrm{B}T)$ is the diffusion (hopping) frequency, and N_s is the sum of all stable clusters

$$N_\mathrm{s} = \sum_{i=2}^{\infty} N_i\,.$$

Single atoms arrive on the surface with frequency F and are consumed by the formation of dimers (the second term on the right-hand side of (2.52a)) and by incorporation into stable clusters (the third term on the right-hand side of (2.52a)). At the very beginning of deposition most of the adatoms are consumed by the formation of dimers. In a later stage of deposition the density of stable clusters increases and the arriving atoms preferentially join stable clusters rather than colliding with each other to produce dimers. Saturation (or very weak dependence on time) is reached and the consumption of atoms by formation of dimers $2DN_1^2$ is practically arrested and becomes negligible compared with the growth term DN_1N_s. A steady state is reached at this stage ($\mathrm{d}N_1/\mathrm{d}t = 0$) and $N_1 = F/DN_\mathrm{s}$. Substituting the latter into (2.52b) and carrying out the integration gives

$$N_\mathrm{s} \propto \left(\frac{D}{F}\right)^{1/3}.$$

This result is easy to generalize for the case of *reversible aggregation*, assuming the critical nucleus consists of $i^* > 1$ atoms. Then one can write a system of two kinetic equations for the single adatoms and the sum of all clusters larger than i^* [2.93]

$$\frac{\mathrm{d}N_1}{\mathrm{d}t} = F - (i^*+1)DN_1^{i^*+1} - DN_1N_\mathrm{s}\,, \tag{2.53a}$$

$$\frac{\mathrm{d}N_\mathrm{s}}{\mathrm{d}t} = \omega^* Dn_1^{i^*+1}\,, \tag{2.53b}$$

where $\omega^* = \alpha^*\exp(E^*/k_\mathrm{B}T)$ (see (2.50)).

Following the same procedure as above results in

$$N_\mathrm{s} \propto \left(\frac{D}{F}\right)^{-\chi}, \tag{2.54}$$

where

$$\chi = \frac{i^*}{i^*+2} \tag{2.55}$$

is the scaling exponent valid for the case of diffusion-limited nucleation and growth in the absence of any kinetic barrier inhibiting the attachment of atoms to the critical nucleus.

Later *Kandel* relaxed the condition for diffusion-limited regime of growth, assuming that a barrier exists which inhibits the attachment of atoms to any cluster including the critical nucleus [2.94]. Then the frequency ω^* for collision of atoms with the critical nucleus should contain the term $\exp(-E_\mathrm{b}/k_\mathrm{B}T)$, where E_b is the barrier concerned. He integrated (2.53b) taking for N_1 a value calculated by the solution of a diffusion equation from the radius R of the nucleus to half of the mean distance $L = 1/\sqrt{\pi N_\mathrm{s}}$ between the nuclei and then averaged from R to L. As a result the average adatom concentration included two terms

$$N_1 = A\frac{F}{D}\frac{1}{N_\mathrm{s}} + B\frac{F}{D}\frac{1-\exp(-E_\mathrm{b}/k_\mathrm{B}T)}{\exp(-E_\mathrm{b}/k_\mathrm{B}T)}\frac{1}{\sqrt{N_\mathrm{s}}}\,,$$

where A and B are constants.

The first term is inversely proportional to N_s as before and does not include the cluster edge barrier E_b. The second term is inversely proportional to the square root of N_s and includes the barrier E_b. Obviously, when $E_\mathrm{b} = 0$ the second term is equal to zero and the integration of (2.53b) naturally gives the scaling

exponent (2.55). In the other extreme of significant cluster edge barrier the second term dominates and the integration of (2.53b) gives the same power-law dependence (2.54) but with a scaling exponent

$$\chi = \frac{2i^*}{i^* + 3}\,, \tag{2.56}$$

which is valid for a kinetic regime of growth.

Equation (2.54) shows a simple power-law dependence of N_s on the ratio D/F of the frequency of surface diffusion to the frequency of atom arrival. While F represents the increase of atoms with time, D introduces the fluxes of disappearance of atoms due either to formation of nuclei or to the further growth of these nuclei. Physically this is the ratio of the flux of consumption of atoms on the crystal surface to the flux of their arrival. A constant ratio D/F means a constant adatom concentration or a constant supersaturation. The increase of D/F can be performed by either increasing the temperature or decreasing the atom arrival rate. The fact that the island density scales with D/F simply means that it depends on the supersaturation. The island density should have one and the same value at a given value of D/F, irrespective of whether it is a result of increasing (decreasing) of temperature or decreasing (increasing) of the atom arrival rate. Increasing D/F means decreasing the supersaturation, which in turn leads to an increase of the nucleus size i^*. Thus, at sufficiently low values of D/F of the order of 10^4–10^5, i^* is expected to be equal to one, whereas at D/F of the order of 10^7–10^8, i^* is expected to be equal to three on a square lattice [2.95]. Assuming a constant atom arrival rate of the order of 10^{-2} monolayers per second, attempt frequency of the order of $1 \times 10^{13}\,\mathrm{s}^{-1}$, and a surface diffusion barrier of 0.75 eV an increase of D/F by four orders of magnitude is equivalent to a temperature increase of 200 K.

It should be noted that considering the size of the critical nucleus as an integer above which all clusters are stable is an approximation which strongly simplifies the mathematical treatment of the problem [2.95]. In fact there are never fully stable clusters. Atoms can always detach from them, particularly at high values of D/F or high temperatures. Things look better at low temperatures when bond breaking is strongly inhibited.

The scaling exponent (2.55) varies with i^* from 1/3 to 1, whereas (2.56) has values larger than unity already at $i^* > 2$. Thus, one can distinguish between diffusion and kinetic regimes of growth if χ is smaller or greater than unity. Examples of the scaling exponent (2.56) have been reported in surfactant-mediated epitaxial growth: homoepitaxy of Si on Sn-precovered surface of Si(111) [2.96], and of Ge on Pb-precovered surface of Si(111) [2.97]. In the former paper a value of $\chi = 1.76$ has been found from the plot of $\ln N_s$ versus $\ln F$. In the case of homoepitaxial growth of Si(111) under clean conditions a value of $\chi = 0.85$ has been obtained from the same plot of $\ln N$ versus $\ln F$ [2.98]. It could be concluded that the nucleation process takes place either in a diffusion regime with $i^* = 6$ or in a kinetic regime with $i^* = 2$. The latter seems more reasonable, bearing in mind the comparatively low temperature of growth (< 700 K) and that Si is a very strongly bonded material.

2.5 Second-Layer Nucleation in Homoepitaxy

Growth of defectless low-index crystal surfaces takes place by formation and growth of 2-D nuclei with monolayer height. When the linear size L of the crystal face is small, in fact, smaller than $L_c = (v/J_0)^{1/3}$ [2.99], where v is the rate of lateral growth and J_0 is the nucleation rate, the growth proceeds by a periodic process of formation of a single nucleus followed by its growth to cover completely the crystal face. Thus, perfect layer-by-layer growth takes place.

When the surface area which is in contact with the supersaturated vapor is large, a large amount of nuclei are formed on the crystal surface on one and the same level. During the growth of the first layer nuclei, a certain size Λ can be reached at which second-layer nuclei can form on top. The average time elapsed from the nucleation of the first-layer nucleus to the appearance of the second-layer nucleus is $\tau = \Lambda/v$. The latter should be inversely proportional to the frequency of nucleation on top of the first-layer nucleus $\bar{J}_0 = J_0 l^2$, or in other words, $\Lambda/v \cong 1/\bar{J}_0$. Thus we find that the critical size for second-layer nucleation is $\Lambda_c = (v/J_0)^{1/3}$ [2.99]. Obviously, when the surface coverage by first-layer nuclei is $\Lambda_c^2 N_s \ll 1$, where N_s is the saturation nucleus density, nuclei of the second, third, etc. layers can form before significant coalescence of the first-layer nuclei takes place. The crystal surface will be rough with many layers growing simultaneously. Multilayer growth takes place. The number N of simultaneously growing layers

depends on v and J_0. If v is large or J_0 is small, Λ_c will be large and the surface roughness will be small, and vice versa.

In the above physical picture it is assumed that the probabilities of attachment of atoms to a step from both the upper and lower terrace are equal. In other words, it is accepted that the barrier which inhibits the incorporation of the atoms to the step and in turn leads to the kinetic regime discussed above is one and the same from both sides of the step. It was at the beginning of 1966 when *Ehrlich* and *Hudda* discovered that the above is completely incorrect [2.100]. They found with the help of field-ion microscopy (the first method which allowed the visualization of single atoms, invented by *Erwin Müller* in the early 1950s) [2.101], that an atom approaching the step from the upper terrace is repulsed by the step. The additional barrier E_{ES}, known now in the literature as the Ehrlich–Schwoebel barrier, was measured later by *Wang* and *Tsong*, who reported values of the order of 0.15–0.2 eV for Re, Ir, and W [2.102]. Much later *Wang* and *Ehrlich* reported that the steps attract the atoms approaching them from the lower terrace [2.103]. The same authors observed in the case of Ir(111) that the atoms, instead of being repelled from the descending step, were in fact attracted by it. Thus they found another, *push-out*, mechanism of step-down diffusion in which the second-level atom pushes out the edge atom and occupies the position of the latter rather than making a jump [2.104]. The atoms thus sample the potential profiles shown in Fig. 2.14a in the case of step-down jumping and in Fig. 2.14b in the case of the push-out mechanism.

The physics behind these effect are easy to understand if we compare interlayer diffusion with the same phenomenon on terraces. It is clear that an atom jumping down the step from the upper terrace will be less coordinated from the side of the lower terrace. On the contrary, an atom approaching the step from the lower terrace will be additionally attracted from the atoms belonging to the upper atomic plane. In the case of the push-out mechanism the atoms taking part in the process *respect a fundamental rule of chemistry – minimizing the breaking of bonds* [2.105].

Schwoebel immediately grasped the importance of the discovery of Ehrlich and Hudda and published later in the same year a paper dealing with the effect of the step-down diffusion barrier on the bunching of steps during evaporation [2.106, 107]. He went even further to foresee the push-out mechanism long before Ehrlich observed it experimentally [2.106].

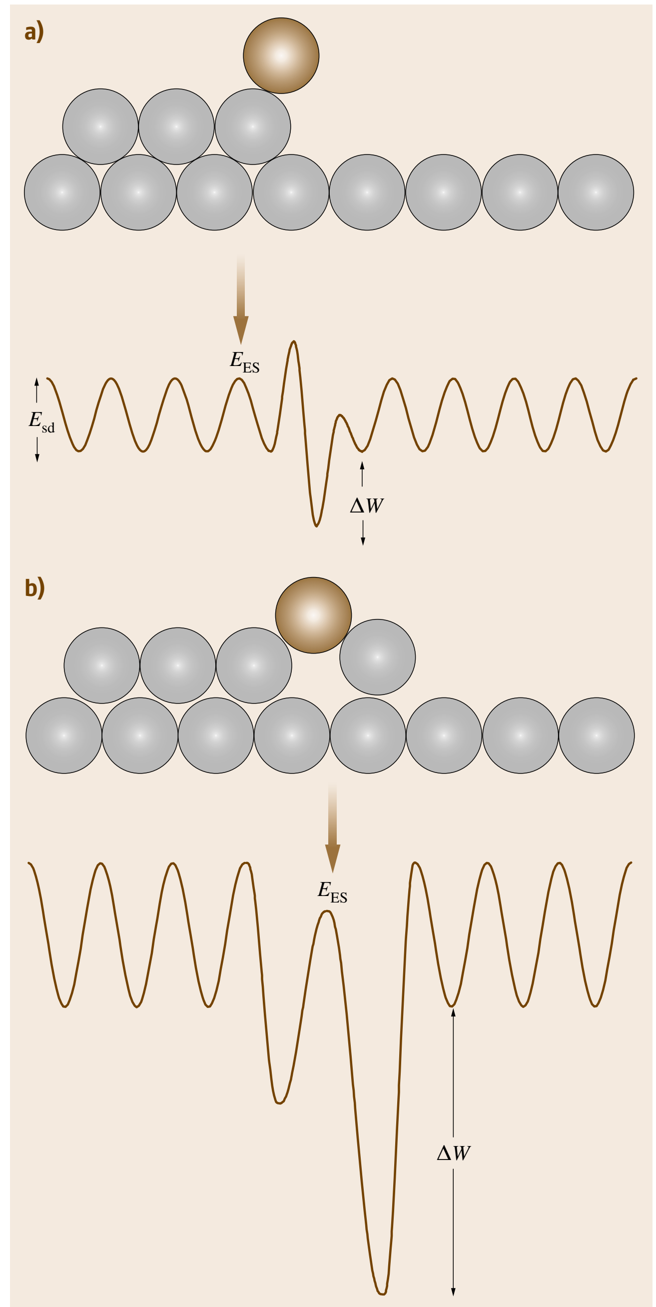

Fig. 2.14a,b Schematic potential diagrams for atoms moving toward ascending and descending steps. **(a)** Traditional view of the Ehrlich–Schwoebel barrier for atoms joining a descending step by a jump and short-range attractive behavior of the ascending step, **(b)** view of the potential sampled by an atom joining a descending step by a push-out mechanism

We consider in this chapter only the traditional Ehrlich–Schwoebel effect of repulsion of atoms from descending steps. The push-out mechanism together with an additional barrier from the lower terrace owing to the presence of surfactant atoms which have decorated the step (the reverse Ehrlich–Schwoebel effect) is considered in [2.108]. The additional ES barrier inhibits the flow of atoms from upper terraces downwards, thus enhancing the nucleation rate on upper terraces. This leads to formation of mounds consisting of concentric two-dimensional islands, one on top of the other, and thus to strong roughening of the surface, a phenomenon which was first predicted by *Villain* [2.109]. We will consider the same problem as above, defining the critical island size Λ for second-layer nucleation accounting for the ES barrier.

We define Λ in the same way as above but writing it in integral form

$$\int_0^{\Lambda} \frac{\bar{J}_0(\rho)}{v(\rho)} \, \mathrm{d}\rho = 1 \,, \tag{2.57}$$

where

$$v(\rho) = \frac{\mathrm{d}\rho}{\mathrm{d}t} = \frac{R}{2\pi\rho N_\mathrm{s} N_0} \tag{2.58}$$

is the rate of growth of the first-layer islands in the case of complete condensation before nuclei on their upper surfaces are formed.

The nucleation frequency $\bar{J}_0$ is defined as before as

$$\bar{J}_0 = 2\pi \int_0^{\rho} J_0(r, \rho) r \, \mathrm{d}r \,, \tag{2.59}$$

where J_0 is the nucleation rate as given by (2.50). It is a function of the island's radius ρ through the adatom concentration on the upper surface of the island N_1. The latter can be determined by solving the diffusion equation (in polar coordinates) in the absence of re-evaporation

$$\frac{\mathrm{d}^2 N_1}{\mathrm{d}r^2} + \frac{1}{r}\frac{\mathrm{d}N_1}{\mathrm{d}r} + \frac{R}{D_\mathrm{s}} = 0 \,. \tag{2.60}$$

The solution reads

$$N_1 = A - \frac{R}{4D_\mathrm{s}} r^2 \,, \tag{2.61}$$

where the integration constant should be determined by the boundary condition

$$j = -D_\mathrm{s} \left(\frac{\mathrm{d}N_1(r)}{\mathrm{d}r} \right)_{r=\rho} \,, \tag{2.62}$$

where $j = j_+ - j_-$ is the net flux of atoms to the descending step which encloses the island, j_+ and j_- being the attachment and detachment fluxes.

Bearing in mind Fig. 2.14 j_+ and j_- read

$$j_+ = a\nu N_\mathrm{st} \exp\left(-\frac{E_\mathrm{sd} + E_\mathrm{ES}}{k_\mathrm{B}T} \right) \,,$$

$$j_- = a\nu N_\mathrm{k} \exp\left(-\frac{\Delta W + E_\mathrm{sd} + E_\mathrm{ES}}{k_\mathrm{B}T} \right) \,,$$

where N_st is the adatom concentration in the vicinity of the step, ν is the attempt frequency, N_k is the concentration of atoms in a position (presumably kink position) for easy detachment from the step, and $\Delta W = \varphi_{1/2} - E_\mathrm{des}$ is the energy to transfer an atom from a kink position onto the terrace.

The total flux j then reads

$$j = a\nu \left(N_\mathrm{st} - N_1^\mathrm{e} \right) \exp\left(-\frac{E_\mathrm{sd}}{k_\mathrm{B}T} \right) \frac{1}{S} \,, \tag{2.63}$$

where $S = \exp(E_\mathrm{ES}/k_\mathrm{B}T)$, and $N_1^\mathrm{e} = N_\mathrm{k} \exp(-\Delta W/k_\mathrm{B}T)$ is the equilibrium adatom concentration (see (2.12)).

Combining (2.62) and (2.63) and bearing in mind that $N_\mathrm{st} = A - R\rho^2/4D_\mathrm{s}$ yields [2.110]

$$N_1 = N_1^\mathrm{e} + \frac{R}{4D_\mathrm{s}} \left(\rho^2 + 2\rho a S - r^2 \right) \,. \tag{2.64}$$

As seen in the case of negligible ES barrier ($2aS/\rho \ll 1$), (2.64) turns into

$$N_1 = N_1^\mathrm{e} + \frac{R}{4D_\mathrm{s}} \left(\rho^2 - r^2 \right) \,. \tag{2.65}$$

The adatom concentration on top of the island surface has a profile of a dome with a maximum above the island's center ($r = 0$) and reaches its equilibrium value N_1^e near the island's edge ($r = \rho$). It follows that second-layer nucleation is favored around the middle of the island.

In the other extreme ($2aS/\rho \gg 1$) we neglect the difference $\rho^2 - r^2$ and obtain

$$N_1 \approx \frac{R}{2D_\mathrm{s}} \rho a S \,.$$

This means that the adatom population on top of an island with repelling boundaries is uniformly distributed all over the surface of the island and a nucleation event can occur with equal probability at any point of it.

We substitute (2.64) into (2.50) and the latter into (2.59) to obtain after integration [2.110]

$$\bar{J}_0 = A \left[\left(\rho^2 + 2\rho a S \right)^{i^*+2} - \left(2\rho a S \right)^{i^*+2} \right] \,, \tag{2.66}$$

where

$$A = \frac{\pi\alpha^*}{(i^*+2)} D_s N_0^2 \exp\left(\frac{E^*}{k_B T}\right)\left(\frac{R}{4D_s N_0}\right)^{i^*+1} .$$

As seen, a negligible ES barrier ($2aS \ll \rho$) turns (2.66) into

$$\bar{J}_0 = A\rho_1^{2(i^*+2)} . \quad (2.67)$$

The condition for layer-by-layer growth (formation of one nucleus for the time $T = R/N_0$ of deposition of a complete monolayer)

$$N = \int_0^T \bar{J}_0(\rho_1)\,dt = 1 \quad (2.68)$$

gives for the number of the growth pyramids the expression [2.111] (for a review see [2.21])

$$N_s = \frac{1}{4\pi} C^* N_0 \left(\frac{D}{F}\right)^{-\chi} \exp\left(\frac{E_{i^*}}{(i^*+2)k_B T}\right) , \quad (2.69)$$

where C^* is a very weak function of i^* of the order of unity. The above equation is in fact (2.54) with the familiar scaling exponent (2.55).

In the other extreme ($2aS \gg \rho$) we take the last two terms of the expansion of the sum in (2.66) and the latter turns into

$$\bar{J}_0 = B\rho^{i^*+3} , \quad (2.70)$$

where

$$B = \pi\alpha^* D_s N_0^2 \exp\left(\frac{E^*}{k_B T}\right)\left(\frac{RaS}{2D_s N_0}\right)^{i^*+1} .$$

Following the above procedure gives for this case [2.112]

$$N_s = \frac{1}{\pi} C^* N_0 \left(\frac{D}{F}\right)^{-\chi} \exp\left(\frac{2[E_{i^*} + (i^*+1)E_b]}{(i^*+3)k_B T}\right) , \quad (2.71)$$

where C^* is another very weak function of i^* of the order of unity. We again obtained (2.54) but the scaling exponent is given by (2.56).

We can now calculate the critical radii of the islands for second-layer nucleation in both cases of low (subscript "0") and high (subscript "ES") Ehrlich–Schwoebel barrier. Substituting (2.67), (2.70) and (2.58) into (2.57) gives after integration [2.110]

$$\Lambda_0 = aC_0\left(\frac{D}{F}\right)^{i^*/2(i^*+3)} , \quad (2.72)$$

with

$$C_0 \cong \left(\frac{N_0 e^{-E^*/k_B T}}{\alpha^* N_s}\right)^{1/2(i^*+3)} , \quad (2.73)$$

for the case of negligible ES barrier, and

$$\Lambda_{ES} = aC_{ES}\left(\frac{D}{F}\right)^{i^*/(i^*+5)} S^{-(i^*+1)/(i^*+5)} , \quad (2.74)$$

with

$$C_{ES} \cong \left(\frac{N_0\,e^{-E^*/k_B T}}{\alpha^* N_s}\right)^{1/(i^*+5)} , \quad (2.75)$$

for the other limiting case of a significant ES barrier.

Let us compare N_s and Λ in both cases. For this purpose we take typical values for the quantities involved: $N_0 = 1\times10^{15}\,cm^{-2}$, $R = 1\times10^{13}\,cm^{-2}\,s^{-1}$, $F = R/N_0 = 1\times10^{-2}\,s^{-1}$, $E_{sd} = 0.4\,eV$, $E_{ES} = 0.2\,eV$, $T = 400\,K$, $i^* = 1$, and $E^* = 0$. Then, in the case of $E_{ES} = 0$, $N_s \approx 6\times10^{10}\,cm^{-2}$ and $\Lambda_0 \approx 180\,Å$. In the other extreme, $N_s \approx 1\times10^{12}\,cm^{-2}$ and $\Lambda_{ES} \approx 50\,Å$ is 3 times smaller. We conclude that with a significant ES barrier a larger density of islands is formed which have much smaller critical size for second-layer nucleation. Mounding rather than planar growth is expected.

It is of interest to check the above theory. For this purpose we calculate the number n of atoms on the surface of the base island when its radius has just reached the critical value Λ. We integrate the adatom concentration (2.64) on the island's surface

$$n = 2\pi \int_0^\Lambda n_s(r,\Lambda) r\,dr$$

and find

$$n = \frac{\pi F}{8D} N_0^2 \Lambda^4 \left(1 + \frac{4aS}{\Lambda}\right) .$$

We will consider as examples two surfaces of fcc crystals: (100) and (111). The reason is that the (100) surfaces are characterized by a large terrace diffusion barrier and a small step-edge barrier. This is the reason why, during growth, (100) surfaces demonstrate as a rule oscillations of the intensity of the specular beam, which are an indication of layer-by-layer growth. On the contrary, the smoother (111) surfaces are characterized with small intralayer diffusion barriers and large interlayer barriers. The result is a roughening of the crystal surface from the very beginning of deposition and a monotonous decrease of the intensity of the specular beam [2.112].

We consider first the case of Cu(001) [2.113]. The authors have measured the step kinetics of a pyramid consisting of 2-D islands, one on top of the other, and determined the critical radius $\Lambda \approx 3\times10^{-5}$ cm of the uppermost island at which the next layer nucleus is formed ($T = 400$ K, $F = 0.0075\,\mathrm{s}^{-1}$, $E_{\mathrm{sd}} = 0.4$ eV, $a = 2.55\times10^{-8}$ cm, $N_0 = 1.53\times10^{15}\,\mathrm{cm}^{-2}$). Comparison with the theory produced the value $E_{\mathrm{ES}} = 0.125$ eV. Then, by using the above formula we find for the number of atoms which gives rise to the new monolayer nucleus the value $n = 70$. Note that $aS/\Lambda \approx 0.03$, which confirms the above statement that the kinetics at fcc(001) surfaces is not dominated by the interlayer diffusion and the profile of the adatom concentration looks like a dome.

We consider next the case of Pt(111) [2.114]. Bott, Hohage, and Comsa observed by scanning tunneling microscopy (STM) the appearance of second-layer nuclei at surface coverages of 0.3 (425 K, $N_{\mathrm{s}} = 3.37\times10^{10}\,\mathrm{cm}^{-2}$) and 0.8 (628 K, $N_{\mathrm{s}} = 3.5\times10^{9}\,\mathrm{cm}^{-2}$) ($R = 5\times10^{12}\,\mathrm{cm}^{-2}\,\mathrm{s}^{-1}$). The activation energy for terrace diffusion is well known to be 0.25–0.26 eV [2.115, 116]. Values for E_{ES} varying from 0.12 eV (see [2.117]) to 0.44 eV have been estimated [2.118]. The average number of atoms on the island's surface as computed with the help of the above equation for n turned out to be of the order of 1×10^{-2}, i. e., much less than unity, which is unphysical. In fact n becomes greater than unity when $E_{\mathrm{ES}} > 0.5$ eV, which means that the atoms at the island's periphery must overcome a total barrier of about 0.75 eV, which is too large to be believed. In contrast to the previous case, however, $aS/\Lambda \gg 1$, which means that it is interlayer diffusion that dominates the kinetics, and the adatom population on top of the island is spatially uniform.

Whereas the Cu(001) case is physically reasonable, the (111) case looks puzzling. In order to solve the problem of the high ES barrier *Krug* et al. accounted for the probabilistic nature of the main processes involved [2.117]. The authors have taken into account the fact that the atoms arrive randomly on the island's surface with an area $\pi\rho^2$ but not at equal intervals $\Delta t = 1/\pi\rho^2 R$ as is implicitly assumed in the model described above. Second, the time τ that the atoms reside on the island before rolling over and joining the descending edge is also a random quantity. The latter is directly proportional to the island's periphery $2\pi\rho$ and inversely proportional to the rate of step-down diffusion $\omega = a\nu\exp[-(E_{\mathrm{sd}} + E_{\mathrm{ES}})/k_{\mathrm{B}}T]$, i. e., $\tau \approx 2\pi\rho/\omega = 2\pi\rho aS/D_{\mathrm{s}}$. We introduce further the time $\tau_{\mathrm{tr}} = \pi\rho^2/D_{\mathrm{s}}$ required for an atom to visit all sites of the island. The condition $\tau/\tau_{\mathrm{tr}} \gg 1$ is equivalent to $2aS/\rho \gg 1$, which is in fact the condition for nucleation kinetics dominated by step-down diffusion (see (2.70)). Assuming $i^* = 1$ (the dimers are stable and immobile) it is concluded that, as soon as two atoms are present simultaneously on the island's surface, their encounter is inevitable. Thus the necessary and sufficient condition for the atoms to meet each other and give rise to a stable cluster is $\tau_{\mathrm{tr}} \ll \tau$. Then the probability of nucleation p_{nuc} is equal to the probability p_2 for two adatoms to be present simultaneously on the island. p_2 is determined by the condition that the time of arrival t_2 of the second atom be shorter than the time t_1 of departure of the first atom. Assuming that t_1 and t_2 are randomly distributed around the average values τ and Δt, respectively, one obtains after integration

$$p_{\mathrm{nuc}} = \frac{1}{\tau\Delta t}\int_0^{\infty} \mathrm{d}t_1\,\mathrm{e}^{-t_1/\tau}\int_0^{t_1} \mathrm{d}t_2\,\mathrm{e}^{-t_2/\Delta t} = \frac{\tau}{\tau+\Delta t}\,.$$

Two limiting cases are possible. The case $\tau \gg \Delta t$ and $p_{\mathrm{nuc}} \approx 1$ is trivial; it means that the ES barrier is infinitely high and there will always be at least one atom on top of the island. The physically interesting case is when $\Delta t \gg \tau$ and $p_{\mathrm{nuc}} = \tau/\Delta t$. Then the nucleation frequency $\bar{J}_0 = \pi\rho^2 R p_{\mathrm{nuc}}$ reads

$$\bar{J}_0 \propto \frac{aR^2\rho^5 S}{D_{\mathrm{s}}}\,. \tag{2.76}$$

This equation should be compared with (2.70). With $i^* = 1$ the latter gives

$$\bar{J}_0 \propto \frac{a^2R^2\rho^4 S^2}{D_{\mathrm{s}}}\,. \tag{2.77}$$

Comparing both formulae shows that the mean-field expression (2.77) is $aS/\rho \gg 1$ times larger than the probabilistic one (2.76). The explanation is simple. Equation (2.77) is based on the implicit assumption that on top of the island there is a time-averaged number (smaller than unity but constant) of atoms all the time. As shown above this is indicative of a large ES barrier whose mathematical expression is just $aS/\rho \gg 1$. In fact the island's surface is empty most of the time and is sometimes populated by a single atom, and it very rarely happens that during this time a second atom arrives. Once two atoms are simultaneously present on the island a nucleus is formed with a probability close to unity. That is why the authors coined for this model the term *the lonely adatom model*. The problem of second-layer nucleation has been intensively studied [2.119, 120]. It has been found that the mean-field

approach is applicable for critical nuclei consisting of more than three atoms. If this is not the case ($i^* = 1, 2$), the random character of the processes involved becomes significant.

2.6 Mechanism of Clustering in Heteroepitaxy

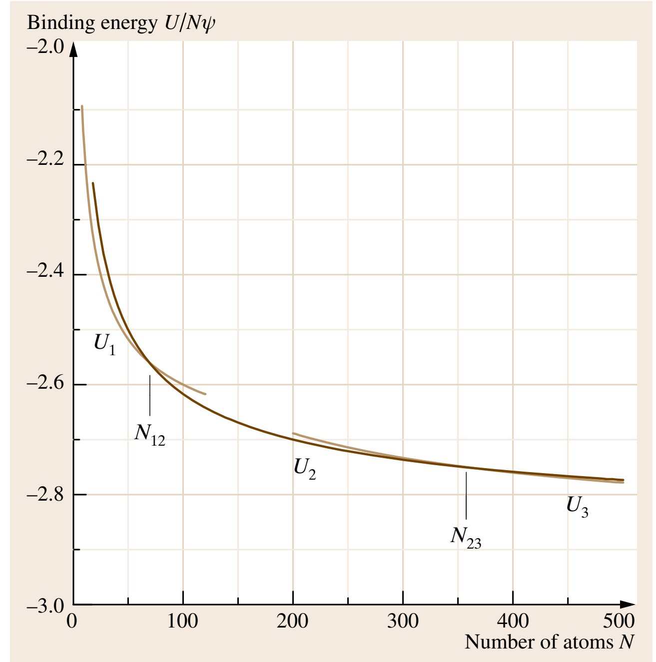

Fig. 2.15 Plot of the binding energy per atom in units of the energy of a single first-neighbor bond ψ of monolayer, bilayer, and trilayer islands with simple cubic lattice as a function of the total number of atoms. The wetting parameter $\phi = 0.1$ (after [2.35]) ▶

We consider first the growth of a heteroepitaxial thin film by the mechanism of Volmer–Weber. As the wetting is incomplete the thermodynamics requires 3-D islanding directly on top of the substrate. We study the stability of islands with different thickness beginning from one monolayer against their volume (or total number of atoms). In other words we study the behavior of the binding energy $-U_i$ in (2.27), which is equal to the *surface* energy term Φ up to a constant $i\varphi_{1/2}$ [2.35].

We study for simplicity a Kossel crystal with (100) substrate orientation. The same result is obtained by using any other lattice and substrate orientation [2.35]. As a first approximation we omit the effect of the lattice misfit. As discussed above the strain energy makes as a rule a minor contribution with the same sign to the difference of the cohesive ψ and adhesive ψ' energies. As another approximation we consider our crystal in a *continuous* way, assuming that the shape remains a complete square irrespective of the number of atoms in it. We calculate first the binding energies of monolayer, bilayer, and trilayer islands with a square shape of the base and consisting of a total of N atoms. Restricting ourselves to nearest-neighbor bonds the energies read

$$\frac{U_1}{N\psi} = -3 + \phi + \frac{2}{\sqrt{N}} ,$$

$$\frac{U_2}{N\psi} = -3 + \frac{\phi}{2} + \frac{2\sqrt{2}}{\sqrt{N}} ,$$

$$\frac{U_3}{N\psi} = -3 + \frac{\phi}{3} + \frac{2\sqrt{3}}{\sqrt{N}} ,$$

where ϕ is the wetting function (2.18).

We plot the above energies as a function of N and find that monolayer-high islands are stable against

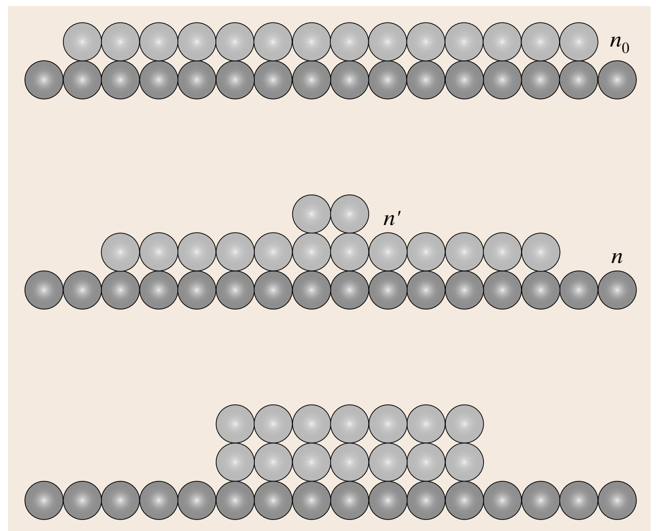

Fig. 2.16 Schematic process for the evaluation of the activation energy of the mono–bilayer transformation. The initial state is a square monolayer island with n_0 atoms in the edge. The intermediate state is a monolayer island with n atoms in the edge plus a second level island with n' atoms in the edge so that $n^2 + n'^2 = n_0^2$. The final state is a complete bilayer island ▶

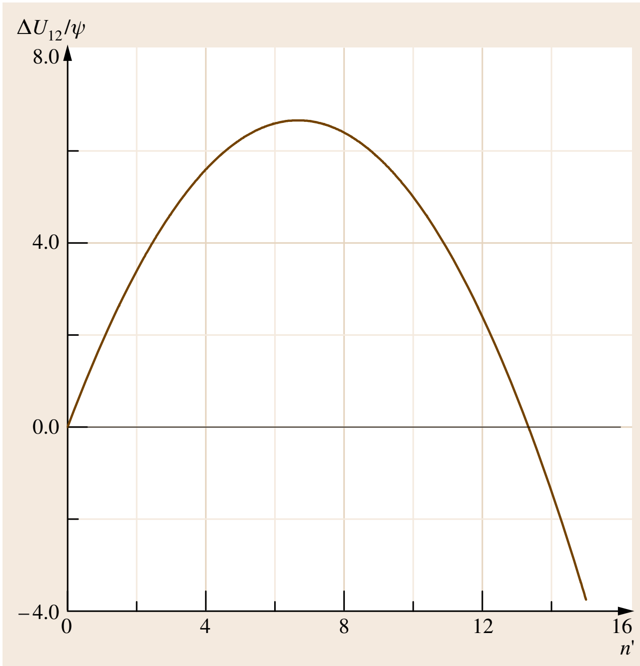

Fig. 2.17 The energy change which accompanies the mono–bilayer transformation in Volmer–Weber growth (after [2.35])

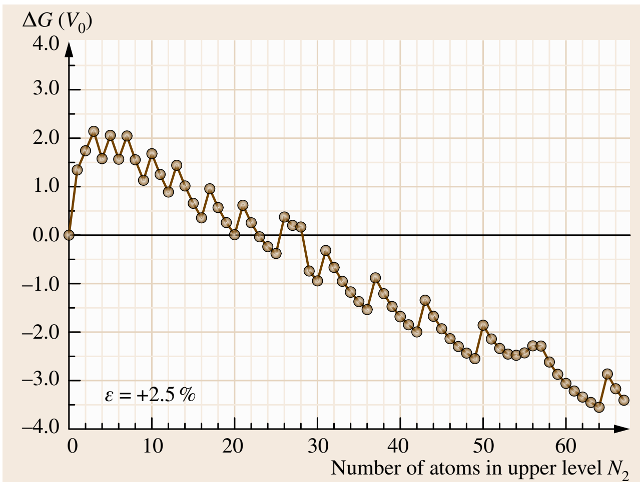

Fig. 2.18 Mono–bilayer transformation curve in Stranski–Krastanov growth representing the energy change in units of bond energy as a function of the number of atoms in the upper level. The lattice misfit is 2.5% (after [2.122])

bilayer islands up to a critical size denoted by N_{12} (Fig. 2.15). The bilayer islands are stable from this size up to a second critical size N_{23}, beyond which trilayer islands become stable, etc. These critical sizes are inversely proportional to the square of the wetting function and go to infinity when $\phi \to 0$. The latter means that, at $\phi = 0$, 3-D islands will not be able to form. Instead, layer-by-layer growth is expected according to the thermodynamics at complete wetting. At finite values of ϕ a mono–bilayer transformation should take place when $N > N_{12}$. A bi–trilayer transformation is expected to occur when $N > N_{23}$, etc. It is very important to note that *monolayer-high islands appear as necessary precursors for 3-D islands* [2.121].

We study further the mechanism of transformation of monolayer to bilayer islands, assuming the following imaginary process illustrated in Fig. 2.16 [2.35]. Atoms detach from the edges of the monolayer islands, which are larger than N_{12} and thus unstable against bilayer islands, diffuse on top of them, aggregate, and give rise to second-layer nuclei. The latter grow further at the expense of the atoms detached from the edges of the lower islands. The process continues up to the moment when the upper island completely covers the lower-level island. The energy change associated with the process of transformation at a particular stage is given by the difference between the energy of the incomplete bilayer island and that of the initial monolayer island

$$\frac{\Delta U_{12}(n')}{\psi} = -n'^2\phi - \frac{n'^2}{n_0} + 2n' , \qquad (2.78)$$

where the approximation $n_0 + n = 2n_0$ is used in the beginning of the transformation, n_0, n, and n' being the numbers of atoms in the edge of the initial monolayer island, in the lower edge of the incomplete bilayer island, and in the edge of the second-layer island, respectively (Fig. 2.16).

Equation (2.78) is plotted in Fig. 2.17. As seen, it displays a maximum at some critical size

$$n'^* = \frac{n_0}{1 + n_0\phi} . \qquad (2.79)$$

The height of the maximum is given by

$$\Delta U^*_{12} = \frac{n_0}{1 + n_0\phi}\psi = n'^*\psi , \qquad (2.80)$$

as should be expected by the classical consideration of the nucleation process (2.36). It follows that the mono–bilayer transformation is a nucleation process.

The same physics functions in the clustering during the Stranski–Krastanov growth of thin films beyond the wetting layer [2.122]. The Stranski–Krastanov growth represents a growth of A on strained A. The strained wetting layer of A is formed on the surface of another

crystal B with different lattice parameter. The 3-D islands which form on the wetting layer are fully strained in the middle but relaxed at the side-walls and edges. The atoms near the edges of the base are displaced from the positions they should occupy if the islands were completely strained to fit the wetting layer. As a result the adhesion of the atoms near the edges of the base to the substrate (the wetting layer) is weaker compared with the atoms in the middle of the island's base. Therefore, the average wetting is incomplete, $0 < \phi < 1$, which is the thermodynamic condition for clustering. The detachment of atoms from the edges and the formation of a cluster in the second level beyond some critical size is energetically favorable. The numerically calculated energy accompanying this process is shown in Fig. 2.18 [2.122]. The atoms interact through a pair potential of Morse type whose anharmonicity can be varied by adjusting two constants that govern separately the repulsive and attractive branches, respectively [2.123, 124]. The 3-D crystallites have fcc lattice and (100) surface orientation, thus possessing the shape of a truncated square pyramid. As seen, a critical nucleus consisting of three atoms is formed, beyond which the energy goes down as in an ordinary nucleation process. The misfit dependence of the critical size N_{12}, the nucleus size, and the work for nucleus formation are shown in Fig. 2.19 [2.122]. The nucleation character of the transformation is clearly observed. The energy barrier and the number of atoms in the cluster with highest energy increase steeply with decreasing lattice misfit, which in this case plays the role of the supersaturation. The number N_{12} also goes to infinity, illustrating the critical behavior of the transition from monolayer (2-D) to bilayer (3-D) islands.

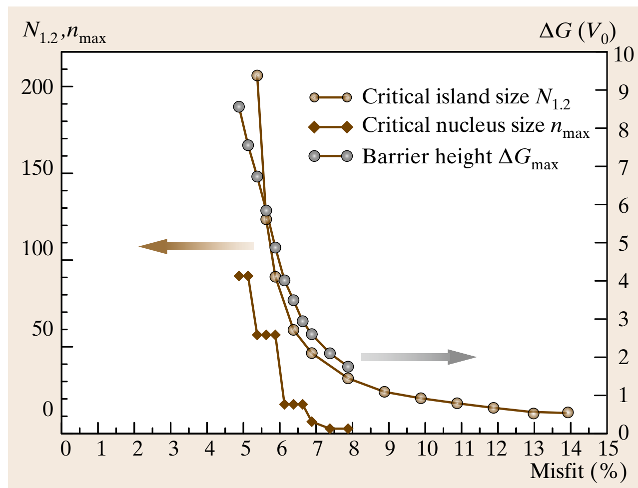

Fig. 2.19 Misfit dependence of the critical size N_{12}, the critical nucleus size (both expressed in number of atoms), and the nucleation barrier (in units of ψ) for compressed overlayers. The initial size of the monolayer island is 20×20 atoms (after [2.122])

It should be pointed out that the mono–bilayer transformation of islands under tensile stress does not display a nucleation behavior, particularly at lower absolute values of the misfit. However, this problem is outside the scope of the present review and will not be discussed.

2.7 Effect of Surfactants on Nucleation

It was found long ago that very often epitaxial films grow in a layer-by-layer mode and show better quality when the vacuum is poor [2.125, 126]. Much later *Steigerwald* et al. found that intentionally adsorbed oxygen on Cu(001) suppresses agglomeration and interdiffusion upon deposition of Fe [2.127]. The significance of these observations was immediately grasped and the very next year *Copel* et al. reported that preadsorption of As drastically alters the mode of growth of Ge on Si(001) and of Si on Ge(001) by suppressing the clustering in the Stranski–Krastanov and Volmer–Weber modes of growth, respectively [2.128]. They suggested an interpretation of their observations in terms of the change of the wetting of the substrate by the overlayer due to the effect of the third element and used the term *surfactant* to stress the thermodynamic nature of the phenomenon. Intensive studies and heated debate concerning the effect of the third elements on the thermodynamics and kinetics of the processes followed. It was shown that the surfactants change not only the thermodynamics but also the kinetics of the processes involved [2.5, 129]. Nevertheless, the term surfactant was widely accepted in the literature. We explore here the effect of surfactants on nucleation in the simpler case of homoepitaxy. Accounting for the unlike substrate requires only the inclusion of a term containing the wetting function (2.19) into the work of nucleus formation.

We calculate first the work for nucleus formation by using the following imaginary process

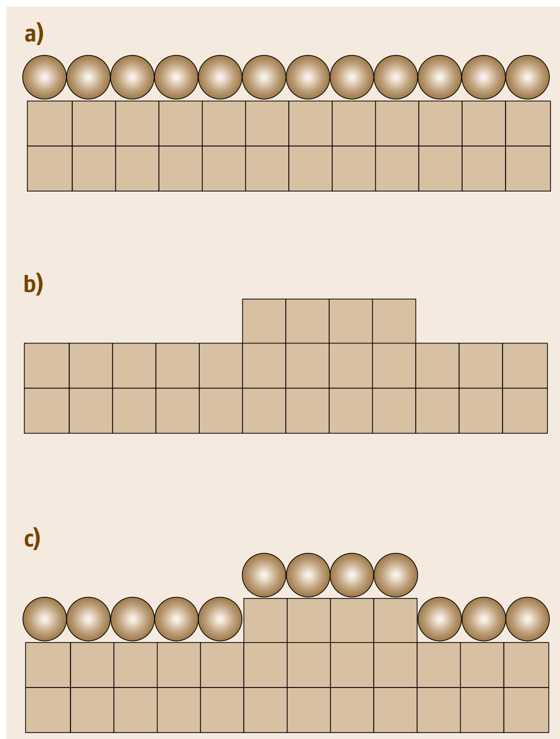

Fig. 2.20a–c Calculation of the Gibbs free energy change for nucleus formation on a surfactant-precovered surface. **(a)** The initial surface covered with a complete monolayer of surfactant atoms denoted by *filled circles*; **(b)** the surfactant layer is evaporated and a cluster consisting of i atoms is created; **(c)** the surfactant layer is condensed back and a cluster consisting of i surfactant atoms is formed on top (after [2.130])

(Fig. 2.20) [2.130]. In order to illustrate the essential physics for simplicity we first make use of the classical nucleation theory. The initial state is a surface of the crystal (C) covered by a complete monolayer of surfactant (S) atoms. We first evaporate reversibly and isothermally all S atoms. Then on the clean surface we produce a cluster consisting of i C atoms. Assuming a square shape with edge length l the work for cluster formation in absence of a surfactant reads

$$\Delta G_0 = -i\Delta\mu + 4l\varkappa_c ,$$

where $\varkappa_c$ is the specific edge energy.

We condense back the S atoms. We gain energy $-4ls\varkappa_c$ due to saturation of the dangling bonds at the cluster periphery by the S atoms, and spend energy $4l\varkappa_s$ to create the new step which surrounds the cluster consisting of S atoms. The work for nucleus formation then reads [2.130]

$$\Delta G_s = \Delta G_0 - 4ls\varkappa_c + 4l\varkappa_s , \quad (2.81)$$

where $\varkappa_s$ is the specific edge energy of the S cluster and the parameter

$$s = 1 - \frac{\omega}{\omega_0}$$

accounts for the saturation of the dangling bonds by S atoms. It is a measure of the *surfactant efficiency*, as the quantities

$$\omega = \tfrac{1}{2}(\psi_{cc} + \psi_{ss}) - \psi_{sc} \quad (2.82)$$

and

$$\omega_0 = \tfrac{1}{2}\psi_{cc}$$

are the energies of the S-saturated and unsaturated dangling bonds, respectively. The subscripts "cc," "ss," and "sc" denote the bond energies C–C, S–S, and S–C, respectively.

Looking at (2.82) it becomes clear that it in fact represents the energetic parameter that determines the enthalpy of mixing of the two species C and S. It must be positive in order to allow the segregation of the surfactant. In the absence of a surfactant $\psi_{ss} = \psi_{sc} = 0$, $\omega = \omega_0$, and $s = 0$. In the other extreme, $\psi_{ss} + \psi_{cc} = 2\psi_{sc}$ and $s = 1$. Thus the parameter s varies from 0 at complete inefficiency to 1 at complete efficiency. (In general the parameter s can be greater than unity, which means $\omega < 0$. However, this means an alloying of the surfactant with the growing crystal, which will have deleterious consequences for the quality of the overlayer and should be avoided.)

It follows from (2.81) that, in the case of surfactant-mediated growth, the Gibbs free energy for nucleus formation contains two more terms that have opposite signs and thus compete with each other. The s-containing term accounts for the decrease of the edge energy of the cluster owing to the saturation of the dangling bonds by the surfactant atoms. The energy $4l\varkappa_s$ of the dangling bonds of the periphery of the cluster, consisting of S atoms, which is unavoidably formed on top of the 2-D nucleus due to the segregation of the surfactant, increases the work of cluster formation.

Finding a solution for a small number of atoms in the critical nucleus in the atomistic extreme is straightforward. We make use of (2.27)

$$\Phi = i\varphi_{1/2} - U_i$$

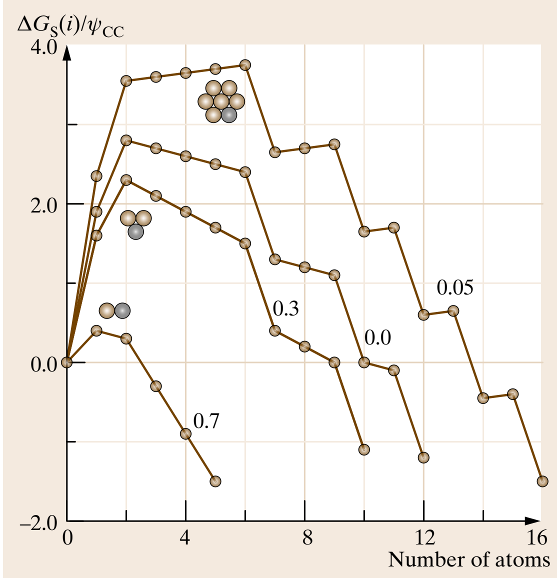

Fig. 2.21 Change of the Gibbs free energy for cluster formation relative to the work needed to disjoin two C atoms versus the number of atoms on the (111) surface of a fcc crystal. The value of the surfactant efficiency s is denoted by figures on each curve. The structure of the nucleus is given by the *filled circles*. The *gray circles* denote the atoms that turn the critical nuclei into smallest stable clusters (after [2.130])

for the edge energy of both clusters instead of using the capillary term for the edge energy $\varkappa$.

The binding energy U_i can be divided into lateral energy E_i and desorption energy E_{des} (assuming additivity of the bond energies)

$$U_i = E_i + iE_{des} ,$$

and for Φ one obtains

$$\Phi = i\Delta W - E_i ,$$

where $\Delta W = \varphi_{1/2} - E_{des}$ is the energy to transfer an atom from a kink position onto the terrace.

We then substitute Φ for $4l\varkappa_c$ in (2.81) to obtain

$$\Delta G_s(i) = -i\Delta\mu + i(1-s)\Delta W - (1-s)E_i + \Phi_s , \quad (2.83)$$

where Φ_s has the meaning of the edge energy $4l\varkappa_s$ of the surfactant cluster.

Figure 2.21 shows the dependence of $\Delta G_s(i)$ in units of the crystal bond strength, ψ_{cc}, on the cluster size i for the (111) surface of fcc metals ($\varphi_{1/2} = 6\psi_{cc}$, $E_{des} = 3\psi_{cc}$, $\Delta W = 3\psi_{cc}$), with $\psi_{ss}/\psi_{cc} = 0.2$, constant supersaturation $\Delta\mu = 1.1\psi_{cc}$, and different values of s denoted by figures on each curve. As seen, $\Delta G_s(i)$ represents a broken line (as should be expected for a small number of atoms, cf. Fig. 2.10), displaying a maximum at $i = i^*$. Under clean conditions ($s = 0$) the critical nucleus consists of two atoms. When s is very small ($= 0.05$, the surfactant is almost inefficient), the number of atoms in the critical nucleus equals six due to the contribution of the edge energy of the surfactant cluster $4l\varkappa_s$. The work of formation of the critical nucleus also increases. Increasing s to 0.3 due to decrease of the edge energy of the cluster leads to a decrease of the nucleation work and i^* becomes again equal to two. At some greater value of s ($= 0.7$), $i^* = 1$ and the aggregation becomes irreversible.

We see that the critical nucleus size differs under one and the same conditions (temperature, rate of deposition) in the absence and presence of a surfactant. In general, we should expect a decrease of the nucleus work and, in turn, a steep increase of the nucleation rate. As a result a larger density of smaller 2-D islands will form. The latter can coalesce and cover completely the surface before formation of nuclei of the upper layer. Thus surfactants can induce layer-by-layer growth by enhancing the nucleation rate [2.131, 132].

The rate of nucleation reads (see (2.42))

$$J_s = \omega_s^* \Gamma N_0 \exp\left(-\frac{\Delta G_s(i^*)}{k_B T}\right) , \quad (2.84)$$

where ω_s^* is the flux of atoms to the critical nucleus in the presence of a surfactant, and $\Gamma \cong 1$ is the Zeldovich factor. $\Delta G_s(i^*)$ is given by (2.83) with $i = i^*$.

Bearing in mind that $\Delta\mu = k_B T \ln(N_1/N_1^e)$, where N_1 and N_1^e are the real and the equilibrium adatom concentrations, we can write

$$\Delta\mu = k_B T \ln\left(\frac{N_1}{N_0}\right) - k_B T \ln\left(\frac{N_1^e}{N_0}\right) , \quad (2.85)$$

where N_1^e is given by (2.12).

Combining (2.83–2.85) and (2.12) gives

$$J_s = \omega_s^* \Gamma N_0 \left(\frac{N_1}{N_0}\right)^{i^*} \times \exp\left(\frac{i^* s\Delta W + (1-s)E^* - \Phi_s}{k_B T}\right) . \quad (2.86)$$

In the absence of a surfactant, $s = 0$, we obtain the familiar expression (2.50) bearing in mind that $\omega_s^* = \omega^* = \alpha^* D_s N_1$.

Note that the presence of the surfactant is not accounted for only by the s-containing terms in the exponential. It is the flux ω_s^* that strongly depends on the mechanism of transport of crystal atoms to the critical nucleus [2.133, 134]. In the case when the transport of atoms to the critical nucleus takes place under the condition of reversible exchange/deexchange of S and C atoms (the time of de-exchange is much smaller than the time of deposition of complete monolayer and atoms have time to perform many exchange/de-exchange events) the nucleus density is given by [2.134] (see for more details [2.21])

$$N_S = N_{s,0} \exp\left(-\frac{\chi}{i_*}\frac{E_S}{k_B T}\right) , \qquad (2.87)$$

where $N_{s,0}$ and χ are given by (2.71) and (2.56), and E_S combines all energy contributions that depend on the presence of the surfactant. Within the framework of the classical nucleation theory the latter is given by

$$E_S = -4ls\varkappa_c + 4l\varkappa_s + E_{ex}^* - i^*\left[(E_{dex} - E_{ex}) - \left(E_{sd}^0 - E_{sd}\right)\right] , \qquad (2.88)$$

where E_{ex} and E_{dex} are the barriers for exchange and de-exchange far from growing nuclei, E_{ex}^* is the barrier for exchange at the edge of the critical nucleus, and E_{sd}^0 and E_{sd} are the barriers for diffusion on clean surface and on top of the surface of the surfactant monolayer. As seen, the first two terms in E_S are of thermodynamic origin whereas the last two terms are of purely kinetic origin.

It follows that the exponential multiplying $N_{s,0}$ can be smaller or larger than unity depending on the sign of E_S. The latter in turn depends on the interplay of the energies involved. We consider in more detail the case of Sb-mediated growth of Si(111) [2.98, 135]. For this case *Kandel* and *Kaxiras* computed the values $E_{dex} = 1.6$ eV, $E_{ex} = 0.8$ eV, and $E_{sd} = 0.5$ eV [2.136]. The value of $E_{sd}^0 = 0.75$ eV has been calculated from experimental data by *Voigtländer* et al. [2.98]. Thus a value of 0.55 eV was found for the difference $(E_{dex} - E_{ex}) - (E_{sd}^0 - E_{sd})$. We recall that $-4ls\varkappa_c = sE^* - i^*s\Delta W$, where ΔW is of order of the half of the heat of evaporation, which for Si is equal to 4.72 eV [2.137]. It can be shown by inspection that $i^*\Delta W$ is always larger than E^*. Thus, when $i^* = 1$, $E^* = 0$ and $\Delta W \cong 2.3$ eV, and when $i^* = 2$, $E^* = 2.3$ eV and $i^*\Delta W \cong 4.6$ eV, etc. The value of s is close to unity as evaluated from the surface energies of Sb and Si available in the literature. It is thus concluded that it is the decrease of the edge energy of the nuclei $4ls\varkappa_c$ due to the saturation of the dangling bonds with S atoms which plays the major role and determines the sign of E_S [2.21]. The latter explains the larger density of 2-D nuclei in surfactant-mediated growth of Si(111) compared with growth in clean conditions [2.98].

Kandel and *Kaxiras* assumed that the exchange/de-exchange processes influence the kinetics of nucleation by affecting the diffusivity of the atoms and derived an expression for an effective diffusion coefficient including the respective barriers [2.5]

$$D_{eff} \cong D_s^0 \exp\left(-\frac{(E_{dex} - E_{ex}) - \left(E_{sd}^0 - E_{sd}\right)}{k_B T}\right) ,$$

and concluded that the atom diffusivity is inhibited due to $(E_{dex} - E_{ex}) > (E_{sd}^0 - E_{sd})$, which leads to increase of the nucleus density according to the scaling relation (2.54). As discussed above the more rigorous analysis shows that it is the thermodynamic term in (2.88) that controls the effect of the surfactant rather than the kinetic barriers.

2.8 Conclusions and Outlook

As shown above the nuclei of the new phase, particularly on surfaces, represent small clusters whose structure, shape, energy, and even size are still unclear. A large amount of work remains to be done in order to study the stability of small clusters of materials with different chemical bonds and crystal lattices as a function of their structure, shape, and size.

References

2.1 T. Michely, J. Krug: *Islands, Mounds and Atoms: Patterns and Processes in Crystal Growth Far from Equilibrium* (Springer, Berlin Heidelberg 2003)

2.2 R. Kern, G. LeLay, J.J. Metois: Basic mechanisms in the early stages of epitaxy. In: *Current Topics in Materials Science*, Vol. 3, ed. by E. Kaldis (North-Holland, Amsterdam 1979) pp. 131–419

2.3 A. Pimpinelli, J. Villain: *Physics of Crystal Growth* (Cambridge Univ. Press, Cambridge 1998)
2.4 P. Politi, G. Grenet, A. Marty, A. Ponchet, J. Villain: Instabilities in crystal growth by atomic or molecular beams, Phys. Rep. **324**, 271–404 (2000)
2.5 D. Kandel, E. Kaxiras: The surfactant effect in semiconductor thin film growth, Solid State Phys. **54**, 219–257 (2000)
2.6 M. Zinke-Allmang, L.C. Feldman, M.H. Grabow: Clustering on surfaces, Surf. Sci. Rep. **16**, 377–463 (1992)
2.7 A.-L. Barabási, H.E. Stanley: *Fractal Concepts in Surface Growth* (Cambridge Univ. Press, Cambridge 1995)
2.8 R. Kaischew, I.N. Stranski: Über den Mechanismus des Gleichgewichts kleiner Kriställchen II, Z. Phys. Chem. **B26**, 114–116 (1934), in German
2.9 J.K. Nørskov, K.W. Jacobsen, P. Stoltze, L.B. Hansen: Many-atom interactions in metals, Surf. Sci. **283**, 277–282 (1993)
2.10 W. Kossel: Zur Energetik von Oberflächenvorgängen, Nachrichten der Gesellschaft der Wissenschaften Göttingen, Mathematisch-Physikalische Klasse, Band 135 (1927), in German
2.11 I.N. Stranski: Über das Wachsen der Kristalle, Ann. Sofia Univ. **24**, 297–315 (1927), in Bulgarian
2.12 I.N. Stranski: Zur Theorie der Kristallwachstums, Z. Phys. Chem. **136**, 259–277 (1928), in German
2.13 R. Kaischew: On the history of the creation of the molecular-kinetic theory of crystal growth, J. Cryst. Growth **51**, 643–650 (1981)
2.14 A. Dupré: *Théorie Méchanique de la Chaleur* (Gauthier-Villard, Paris 1869) p. 369, in French
2.15 E. Bauer: Phänomenologische Theorie der Kristallabscheidung an Oberflächen I, Z. Krist. **110**, 372–394 (1958), in German
2.16 I.N. Stranski, K. Kuleliev: Beitrag zur isomorphen Fortwaschung von Ionenkristallen aufeinander, Z. Phys. Chem. A **142**, 467–476 (1929), in German
2.17 I.N. Stranski, L. Krastanov: Zur Theorie der orientierten Ausscheidung von Ionenkristallen aufeinander, Monatsh. Chem. **71**, 351–364 (1938), in German
2.18 F.C. Frank, J.H. van der Merwe: One-dimensional dislocations I. Static theory, Proc. R. Soc. Lond. Ser. A **198**, 205–216 (1949)
2.19 F.C. Frank, J.H. van der Merwe: One-dimensional dislocations II. Misfitting monolayers oriented overgrowth, Proc. R. Soc. Lond. Ser. A **198**, 216–225 (1949)
2.20 M. Volmer, A. Weber: Keimbildung in übersättigten Gebilden, Z. Phys. Chem. **119**, 277–301 (1926), in German
2.21 I. Markov: *Crystal Growth for Beginners*, 2nd edn. (World Scientific, New Jersey 2003)
2.22 M.H. Grabow, G.H. Gilmer: Thin film growth modes. Wetting and cluster nucleation, Surf. Sci. **194**, 333–346 (1988)
2.23 B. Voigtländer: Fundamental processes in Si/Si and Ge/Si epitaxy studied by scanning tunneling microscopy during growth, Surf. Sci. Rep. **43**, 127–254 (2001)
2.24 W.K. Burton, N. Cabrera, F.C. Frank: The growth of crystals and the equilibrium structure of their surfaces, Philos. Trans. R. Soc. Lond. Ser. A **243**, 299–358 (1951)
2.25 J.W. Gibbs: *On the Equilibrium of Heterogeneous Substances, Collected Works* (Longmans Green, New York 1928)
2.26 R.L. Dobrushin, R. Kotecky, S. Shlosman: *Wulff Construction: A Global Shape from Local Interactions* (American Mathematical Society, Providence 1993)
2.27 R. Kaischew: Equilibrium shape and work of formation of crystalline nuclei on substrates, Commun. Bulg. Acad. Sci. (Phys.) **1**, 100–133 (1950), in Bulgarian
2.28 I.N. Stranski, R. Kaischew: Gleichgewichtsformen homeopolarer Kristalle, Z. Kristallogr. **78**, 373–383 (1931), in German
2.29 R. Peierls: Clustering in adsorbed films, Phys. Rev. B **18**, 2013–2015 (1978)
2.30 Y.I. Frenkel: *Kinetic Theory of Liquids* (Dover, New York 1955)
2.31 R. Kaischew: On the thermodynamics of crystalline nuclei, Commun. Bulg. Acad. Sci. (Phys.) **2**, 191–202 (1951), in Bulgarian
2.32 I.N. Stranski: Zur Berechnung der spezifischen Oberflächen-, Kanten- und Eckenenergien an kleinen Kristallen, Ann. Sofia Univ. **30**, 367–375 (1936), in German
2.33 N. Cabrera, R.V. Coleman: Theory of crystal growth from the vapor. In: *The Art and Science of Growing Crystals*, ed. by J.J. Gilman (Wiley, New York 1963) pp. 3–28
2.34 H.-C. Jeong, E.D. Williams: Steps on surfaces: Experiment and theory, Surf. Sci. Rep. **34**, 171–294 (1999)
2.35 S. Stoyanov, I. Markov: On the 2D–3D transition in epitaxial thin film growth, Surf. Sci. **116**, 313–337 (1982)
2.36 S. Toschev, M. Paunov, R. Kaischew: On the question of formation of three-dimensional and two-dimensional nuclei in crystallization on substrates, Commun. Dept. Chem. Bulg. Acad. Sci. **1**, 119–129 (1968), in Bulgarian
2.37 I. Markov, R. Kaischew: Influence of the supersaturation on the mode of crystallization on crystalline substrates, Thin Solid Films **32**, 163–167 (1976)
2.38 I. Markov, R. Kaischew: Influence of the supersaturation on the mode of thin film growth, Krist. Tech. **11**, 685–697 (1976)
2.39 A. Crottini, D. Cvetko, L. Floreano, R. Gotter, A. Morgante, F. Tommasini: Step height oscillations during layer-by-layer growth of Pb on Ge(001), Phys. Rev. Lett. **79**, 1527–1530 (1997)
2.40 V.V. Voronkov: Movement of elementary step by formation of one-dimensional nuclei, Sov. Phys. Crystallogr. **15**, 13–19 (1970), in Russian

2.41 F.C. Frank: Nucleation-controlled growth one a one-dimensional growth of finite length, J. Cryst. Growth **22**, 233–1236 (1974)
2.42 J. Zhang, G.H. Nancollas: Kink densities along a crystal surface step at ow temperatures and under nonequilibrium conditions, J. Cryst. Growth **106**, 181–190 (1990)
2.43 S. Stoyanov: Formation of bilayer steps during growth and evaporation of Si(001) vicinal surfaces, Europhys. Lett. **11**, 361–366 (1990)
2.44 I. Markov: Kinetics of MBE growth of Si(001)1 × 1, Surf. Sci. **279**, L207–L212 (1992)
2.45 P. Vekilov: Kinetics and mechanisms of protein crystallization at the molecular level, Methods Mol. Biol. **300**, 15–52 (2005)
2.46 R. Becker, W. Döring: Kinetische Behandlung der Keimbildung in übersättigten Dämpfen, Ann. Phys. **24**, 719–752 (1935), in German
2.47 J.W. Christian: *The Theory of Transformations in Metals and Alloys*, 3rd edn. (Pergamon, New York 2002), Parts I and II
2.48 D. Kashchiev: *Nucleation* (Butterwords, Oxford 2000)
2.49 S.W. Benson: *The Foundations of Chemical Kinetics* (McGraw-Hill, New York 1960)
2.50 M. Volmer: *Kinetik der Phasenbildung* (Theodor Steinkopf, Dresden 1939), in German
2.51 J. Lothe, G.M. Pound: Reconsideration of nucleation theory, J. Chem. Phys. **36**, 2080–2085 (1962)
2.52 G.M. Pound, M.T. Simnad, L. Yang: Heterogeneous nucleation of crystals from vapor, J. Chem. Phys. **22**, 1215–1219 (1954)
2.53 J.G. Dash: Clustering and percolation transitions in helium and other thin films, Phys. Rev. B **15**, 3136–3146 (1977)
2.54 J.M. Liang, L.J. Chen, I. Markov, G.U. Singco, L.T. Shi, C. Farrell, K.N. Tu: Crystallization of amorphous $CoSi_2$ thin films I. Kinetics of nucleation and growth, Mater. Chem. Phys. **38**, 250–257 (1994)
2.55 J.P. Hirth, G.M. Pound: *Condensation and Evaporation, Progress in Materials Science* (MacMillan, New York 1963)
2.56 E. Korutcheva, A.M. Turiel, I. Markov: Coherent Stranski–Krastanov growth in 1+1 dimensions with anharmonic interactions: An equilibrium study, Phys. Rev. B **61**, 16890–16901 (2000)
2.57 J.E. Prieto, I. Markov: Thermodynamic driving force of formation of coherent three-dimensional islands in Stranski–Krastanov growth, Phys. Rev. B **66**, 073408 (2002)
2.58 D. Walton: Nucleation of vapor deposits, J. Chem. Phys. **37**, 2182–2188 (1962)
2.59 S. Stoyanov: Nucleation theory for high and low supersaturations. In: *Current Topics in Materials Science*, Vol. 3, ed. by E. Kaldis (North-Holland, Amsterdam 1979) pp. 421–462
2.60 S. Stoyanov: On the atomistic theory of nucleation rate, Thin Solid Films **18**, 91–98 (1973)
2.61 S. Toschev, I. Markov: An experimental study of nonsteady state nucleation, Ber. Bunsenges. Phys. Chem. **73**, 184–188 (1969)
2.62 A. Milchev, S. Stoyanov: Classical and atomistic models of electrolytic nucleation: comparison with experimental data, J. Electroanal. Chem. **72**, 33–43 (1976)
2.63 A. Milchev, J. Malinowski: Phase formation – Stability and nucleation kinetics of small clusters, Surf. Sci. **156**, 36–43 (1985)
2.64 D. Kashchiev: On the relation between nucleation, nucleus size and nucleation rate, J. Chem. Phys. **76**, 5098–5102 (1982)
2.65 B. Müller, L. Nedelmann, B. Fischer, H. Brune, K. Kern: Initial stages of Cu epitaxy on Ni(100): postnucleation and a well-defined transition in critical island size, Phys. Rev. B **54**, 17858–17865 (1996)
2.66 J.A. Venables: *Introduction to Surface and Thin Film Processes* (Cambridge Univ. Press, Cambridge 2000)
2.67 J.L. Robins, T.N. Rhodin: Nucleation of metal clusters on ionic surfaces, Surf. Sci. **2**, 320–345 (1964)
2.68 R. Kaischew, B. Mutaftschiev: Über die elektrolytische Keimbildung des Quecksilbers, Electrochim. Acta **10**, 643–650 (1965), in German
2.69 B. Lewis, D. Campbell: Nucleation and initial growth behavior of thin film growth, J. Vac. Sci. Technol. **4**, 209–218 (1967)
2.70 M.J. Stowell: The dependence of saturation nucleus density on deposition rate and substrate temperature in the case of complete condensation, Philos. Mag. **21**, 125–136 (1970)
2.71 I. Markov: The influence of surface diffusion processes on the kinetics of heterogeneous nucleation, Thin Solid Films **8**, 281–292 (1971)
2.72 R.A. Sigsbee: Vapor to condensed-phase heterogeneous nucleation. In: *Nucleation*, ed. by A.C. Zettlemoyer (Marcel Dekker, New York 1969) pp. 151–224
2.73 I. Markov, A. Boynov, S. Toschev: Screening action and growth kinetics of electrodeposited mercury droplets, Electrochim. Acta **18**, 377–384 (1973)
2.74 A.N. Kolmogorov: Statistical theory of crystallization of metals, Izv. Akad. Nauk USSR (Otd. Phys. Math. Nauk) **3**, 355–359 (1937), in Russian
2.75 M. Avrami: Kinetics of phase change. I. General theory, J. Chem. Phys. **7**, 1103–1112 (1939)
2.76 M. Avrami: Kinetics of phase change. II. Transformation-time relations for random distribution of nuclei, J. Chem. Phys. **8**, 212–224 (1940)
2.77 M. Avrami: Kinetics of phase change III. Granulation, phase change and microstructure of phase change, J. Chem. Phys. **9**, 177–184 (1941)
2.78 W. Johnson, R. Mehl: Reaction kinetics in processes of nucleation and growth, Trans. Am. Inst. Min. Metal. Eng. **135**, 416–458 (1939)
2.79 I. Markov, D. Kashchiev: The role of active centers in the kinetics of new phase formation, J. Cryst. Growth **13/14**, 131–134 (1972)

2.80 I. Markov, D. Kashchiev: Nucleation on active centres I. General theory, J. Cryst. Growth **16**, 170–176 (1972)
2.81 G. Zinsmeister: A contribution to Frenkel's theory of condensation, Vacuum **16**, 529–535 (1966)
2.82 G. Zinsmeister: Theory of thin film condensation, Part b: Solution of the simplified condensation equations, Thin Solid Films **2**, 497–507 (1968)
2.83 G. Zinsmeister: Theory of thin film condensation, Part c: Aggregate size distribution in islands films, Thin Solid Films **4**, 363–386 (1969)
2.84 G. Zinsmeister: Theory of thin film condensation, Part d: Influence of variable collision factor, Thin Solid Films **7**, 51–75 (1971)
2.85 D.R. Frankl, J.A. Venables: Nucleation on substrates from the vapor phase, Adv. Phys. **19**, 409–456 (1970)
2.86 J.A. Venables: Rate equations approaches to thin film nucleation and growth, Philos. Mag. **27**, 697–738 (1973)
2.87 S. Stoyanov, D. Kashchiev: Thin film nucleation and growth theories: A confrontation with experiment. In: *Current Topics in Materials Science*, Vol. 7, ed. by E. Kaldis (North-Holland, Amsterdam 1981), pp. 69–141
2.88 G.S. Bales, D.C. Chrzan: Dynamics of irreversible island growth during submonolayer epitaxy, Phys. Rev. B **50**, 6057–6067 (1994)
2.89 G.S. Bales, A. Zangwill: Self-consistent rate theory of submonolayer homoepitaxy with attachment/detachment kinetics, Phys. Rev. B **55**, R1973–R1976 (1997)
2.90 J.G. Amar, F. Family, P.M. Lam: Dynamic scaling of the island-size distribution and percolation in a model of submonolayer molecular beam epitaxy, Phys. Rev. B **50**, 8781–8797 (1994)
2.91 J.G. Amar, F. Family: Critical cluster size: Island morphology and size distribution in submonolayer epitaxial growth, Phys. Rev. Lett. **74**, 2066–2069 (1995)
2.92 H. Brune, G.S. Bales, J. Jacobsen, C. Boragno, K. Kern: Measuring surface diffusion from nucleation island densities, Phys. Rev. B **60**, 5991–6006 (1999)
2.93 J.A. Venables, G.D.T. Spiller, M. Handbücken: Nucleation and growth of thin films, Rep. Prog. Phys. **47**, 399–460 (1984)
2.94 D. Kandel: Initial stages of thin film growth in the presence of island-edge barriers, Phys. Rev. Lett. **78**, 499–502 (1997)
2.95 C. Ratsch, P. Šmilauer, A. Zangwill, D.D. Vvedensky: Submonolayer epitaxy without a critical nucleus, Surf. Sci. **329**, L599–L604 (1995)
2.96 S. Iwanari, K. Takayanagi: Surfactant epitaxy of Si on Si(111) surface mediated by a Sn layer I. Reflection electron microscope observation of the growth with and without a Sn layer mediate the step flow, J. Cryst. Growth **119**, 229–240 (1992)
2.97 I.-S. Hwang, T.-C. Chang, T.T. Tsong: Exchange-barrier effect on nucleation and growth of surfactant mediated epitaxy, Phys. Rev. Lett. **80**, 4229–4232 (1998)
2.98 B. Voigtländer, A. Zinner, T. Weber, H.P. Bonzel: Modification of growth kinetics in surfactant mediated epitaxy, Phys. Rev. B **51**, 7583–7591 (1995)
2.99 A.A. Chernov: *Modern Crystallography III*, Springer Series in Solid State Sciences, Vol. 36 (Springer, Berlin 1984)
2.100 G. Ehrlich, F.G. Hudda: Atomic view of surface self-diffusion: tungsten on tungsten, J. Chem. Phys. **44**, 1039–1049 (1966)
2.101 E. Müller: Das Feldionenmikroskop, Z. Phys. **131**, 136–142 (1951), in German
2.102 S.C. Wang, T.T. Tsong: Measurements of the barrier height on the reflective W(110) plane boundaries in surface diffusion of single atoms, Surf. Sci. **121**, 85–97 (1982)
2.103 S.C. Wang, G. Ehrlich: Atom condensation at lattice steps and clusters, Phys. Rev. Lett. **71**, 4174–4177 (1993)
2.104 S.C. Wang, G. Ehrlich: Atom incorporation at surface clusters: an atomic view, Phys. Rev. Lett. **67**, 2509–2512 (1991)
2.105 P. Feibelman: Surface diffusion by concerted substitution, Comments Condens. Matter. Phys. **16**, 191–203 (1993)
2.106 R. Schwoebel, E.J. Shipsey: Step motion on crystal surfaces, J. Appl. Phys. **37**, 3682–3686 (1966)
2.107 R. Schwoebel: Step motion on crystal surfaces II, J. Appl. Phys. **40**, 614–618 (1966)
2.108 I. Markov: Kinetics of surfactant mediated epitaxial growth, Phys. Rev. B **50**, 11271 (1994)
2.109 J. Villain: Continuum models of crystal growth from atomic beams with and without desorption, J. Phys. I France **1**, 19–42 (1991)
2.110 J. Tersoff, A.W. Denier van der Gon, R.M. Tromp: Critical island size for layer-by-layer growth, Phys. Rev. Lett. **72**, 266–269 (1994)
2.111 S. Stoyanov: Layer growth of epitaxial films and superlattices, Surf. Sci. **199**, 226–242 (1988)
2.112 I. Markov: Surface energetics from the transition from step-flow growth to two-dimensional nucleation in metal homoepitaxy, Phys. Rev. B **56**, 12544–12552 (1997)
2.113 R. Gerlach, T. Maroutian, L. Douillard, D. Martinotti, H.-J. Ernst: A novel method to determine the Ehrlich–Schwoebel barrier, Surf. Sci. **480**, 97–102 (2001)
2.114 M. Bott, T. Hohage, G. Comsa: The homoepitaxial growth of Pt on Pt(111) studied by STM, Surf. Sci. **272**, 161–166 (1992)
2.115 P. Feibelmann, J.S. Nelson, G.L. Kellogg: Energetics of Pt adsorption on Pt(111), Phys. Rev. B **49**, 10548–10556 (1994)
2.116 M. Bott, T. Hohage, M. Morgenstern, T. Michely, G. Comsa: New approach for determination of diffusion parameters of adatoms, Phys. Rev. Lett. **76**, 1304–1307 (1996)

2.117 J. Krug, P. Politi, T. Michely: Island nucleation in the presence of step-edge barriers: Theory and applications, Phys. Rev. B **61**, 14037–14046 (2000)
2.118 I. Markov: Method for evaluation of the Ehrlich–Schwoebel barrier to interlayer transport in metal homoepitaxy, Phys. Rev. B **54**, 17930–17937 (1996)
2.119 J. Rottler, P. Maass: Second layer nucleation in thin film growth, Phys. Rev. Lett. **83**, 3490–3493 (1999)
2.120 S. Heinrichs, J. Rottler, P. Maass: Nucleation on top of islands in epitaxial growth, Phys. Rev. B **62**, 8338–8359 (2000)
2.121 C. Priester, M. Lannoo: Origin of self-assembled quantum dots in highly mismatched heteroepitaxy, Phys. Rev. Lett. **75**, 93–96 (1995)
2.122 J.E. Prieto, I. Markov: Quantum dots nucleation in strained-layer epitaxy: Minimum energy pathway in the stress-driven two-dimensional to three-dimensional transformation, Phys. Rev. B **72**, 205412 (2005)
2.123 I. Markov, A. Trayanov: Epitaxial interfaces with realistic interatomic forces, J. Phys. C **21**, 2475–2493 (1988)
2.124 I. Markov: Static multikink solutions in a discrete Frenkel–Kontorova model with anharmonic interactions, Phys. Rev. B **48**, 14016–14019 (1993)
2.125 J.W. Matthews, E. Grünbaum: The need for contaminants in the epitaxial growth of gold on rock salt, Appl. Phys. Lett. **5**, 106–108 (1964)
2.126 E. Grünbaum: Epitaxial growth of single-crystal films, Vacuum **24**, 153–159 (1973)
2.127 D.A. Steigerwald, I. Jacob, W.F. Egelhoff Jr.: Structural study of the epitaxial growth of fcc-Fe films, sandwiches and superlattices on Cu(100), Surf. Sci. **202**, 472–492 (1988)
2.128 M. Copel, M.C. Reuter, E. Kaxiras, R.M. Tromp: Surfactants in epitaxial growth, Phys. Rev. Lett. **63**, 632–635 (1989)
2.129 I. Markov: Surfactants in semiconductor heteroepitaxy: thermodynamics and/or kinetics?. In: *NATO ASI Series: Collective Diffusion on Surfaces: Correlation Effects and Adatom Interactions*, ed. by M. Tringides, Z. Chvoy: (Kluwer, Dordrecht 2001) pp. 259–271
2.130 I. Markov: Kinetics of nucleation in surfactant-mediated epitaxy, Phys. Rev. B **53**, 4148–4155 (1996)
2.131 G. Rosenfeld, R. Servaty, C. Teichert, B. Poelsema, G. Comsa: Layer-by-layer growth of Ag on Ag(111) induced by enhanced nucleation: A model study for surfactant-mediated growth, Phys. Rev. Lett. **71**, 895–898 (1993)
2.132 H.A. van der Vegt, J. Vrijmoeth, R.J. Behm, E. Vlieg: Sb-enhanced nucleation in homoepitaxial growth of Ag(111), Phys. Rev. B **57**, 4127–4131 (1998)
2.133 I. Markov: Scaling behavior of the critical terrace width for step-flow growth, Phys. Rev. B **59**, 1689–1692 (1999)
2.134 I. Markov: Nucleation and step-flow growth in surfactant mediated homoepitaxy with exchange/de-exchange kinetics, Surf. Sci. **429**, 102–116 (1999)
2.135 M. Horn-von Hoegen, J. Falta, R. Tromp: Surfactants in Si(111) homoepitaxy, Appl. Phys. Lett. **66**, 487–489 (1995)
2.136 D. Kandel, E. Kaxiras: Surfactant mediated crystal growth of semiconductors, Phys. Rev. Lett. **75**, 2742–2745 (1995)
2.137 R. Hultgren, P.D. Desai, D.T. Hawkins, M. Gleiser, K.K. Kelley, D.D. Wagman: *Selected Values of the Thermodynamic Properties of the Elements* (American Society for Metals, Metals Park 1973)

3. Morphology of Crystals Grown from Solutions

Francesco Abbona, Dino Aquilano

Growth from solutions is widely used both in research laboratories and in many industrial fields. The control of crystal habit is a key point in solution growth as crystals may exhibit very different shapes according to the experimental conditions. In this chapter a concise review is given on this topic. First, the equilibrium shape is rather deeply developed due to its primary importance to understand crystal morphology, then the growth shape is treated and the main factors affecting the crystal habit are briefly illustrated and discussed. A rich literature completes the chapter.

3.1 **Equilibrium Shape** ... 55
3.1.1 The Atomistic Approach: The Kossel Crystal and the Kink Site 55
3.1.2 Surface Sites and Character of the Faces ... 55
3.1.3 The Equilibrium Crystal – Mother Phase: The Atomistic Point of View . 57
3.1.4 The Equilibrium Shape of a Crystal on a Solid Substrate ... 58
3.1.5 The Stranski–Kaischew Criterion to Calculate the Equilibrium Shape . 60

3.2 **The Theoretical Growth Shape** ... 64
3.2.1 The Structural Approach ... 64
3.2.2 Crystal Structure and Bond Energy: The Hartman–Perdok Theory ... 64
3.2.3 The Effect of Foreign Adsorption on the Theoretical Growth Shape ... 66

3.3 **Factors Influencing the Crystal Habit** ... 71

3.4 **Surface Structure** ... 72
3.4.1 The α–Factor and the Roughening Transition ... 72
3.4.2 Kinetic Roughening ... 72
3.4.3 Polar Crystals ... 72
3.4.4 Looking at Surfaces with AFM ... 73

3.5 **Crystal Defects** ... 73

3.6 **Supersaturation – Growth Kinetics** ... 73
3.6.1 Growth Laws ... 74
3.6.2 Some Experimental Results ... 74

3.7 **Solvent** ... 75
3.7.1 Choice of Solvent ... 76
3.7.2 Change of Solvent ... 76
3.7.3 Solvent–Solute ... 77
3.7.4 Solvent–Crystal Surface ... 77
3.7.5 Mechanisms of Action ... 77

3.8 **Impurities** ... 78
3.8.1 The Main Factors ... 78
3.8.2 Kinetic Models ... 78
3.8.3 Adsorption Sites ... 80
3.8.4 Effect of Impurity Concentration and Supersaturation ... 80
3.8.5 Effect of Impurity Size ... 82
3.8.6 Composition of the Solution: pH ... 83

3.9 **Other Factors** ... 84
3.9.1 Temperature ... 84
3.9.2 Magnetic Field ... 85
3.9.3 Hydrodynamics ... 85

3.10 **Evolution of Crystal Habit** ... 85

3.11 **A Short Conclusion** ... 86

3.A **Appendix** ... 86
3.A.1 The Equilibrium Pressure of an Infinite Monoatomic Crystal with Its Own Vapor ... 86

References ... 87

Interest in the crystal habit of minerals dates back a long time in the history of mankind. A detailed history on this topics and crystallization in general is given by *Scheel* [3.1]; here only a short account of crystal morphology is presented. Crystal habit, which attracted the interest of great scientists such as Kepler, Descartes, Hooke, and Huygens, is relevant from the scientific point of view, since it marks the beginning of crystallography as a science. Its birth can be dated to 1669 when the Danish scientist Niels Steensen, studying in Florence the quartz and hematite crystals from Elba island, suggested the first law of crystallography (constancy of the dihedral angle) and the mechanism of face growth (layer by layer). A century later this law was confirmed by Romé de l'Isle. At the end of the 18th century the study of calcite crystals led the French abbé René Just Haüy to enunciate the first theory on crystal structure and to discover the second law (rational indices). It is worth noticing that these early scholars met with great difficulty in studying crystal habit since, contrary to botany and zoology where each species has its own definite morphology, the crystal habit of minerals is strongly variable within the same species. In the first part of the 19th century the study of crystal habit led to the development of the concept of symmetry and the derivation of the 32 crystal classes. Bravais, by introducing the idea of the crystal lattice, was the first to try to relate crystal habit to internal structure (the Bravais law, saying that the crystal faces are lattice planes of high point density). At the end of the 19th century research on internal symmetry ended with the derivation of the 230 space groups. In this century research on crystallization, mainly from solution but also from melt, went on and interlaced with progress in other disciplines (chemistry, physics, thermodynamics, etc.). We should recall the important contributions by Gibbs (1878), Curie (1885), and Wulff (1901) on the equilibrium form of crystals, which was tackled later from an atomistic point of view by *Stranski* [3.2] and *Stranski* and *Kaischew* [3.3, 4].

The relationship between morphology and internal structure (the Bravais law) was treated by *Niggli* [3.5] and developed by *Donnay* and *Harker* [3.6], who considered the space group instead of the Bravais lattice type as a factor conditioning the crystal morphology. From about 1950 onwards, interest in crystal growth increased due to the role of crystals in all kinds of industry and the discovery of relevant properties of new crystalline compounds. Besides the technological progress, a milestone was the publication in 1951 of the first theory on growth mechanisms of flat crystal faces by *Burton*, *Cabrera*, and *Frank* (BCF) [3.7].

Also, the crystal habit was receiving growing attention due to theoretical interest and industrial needs. The Donnay–Harker principle is exclusively crystallographic. A chemical approach was adopted by Hartman and Perdok; looking at crystal structure as a network of periodic bond chains (PBC) they published in 1955 a method that is still fundamental to studies of theoretical crystal morphology [3.8–10]. The method, at first qualitative, was made quantitative through the calculation of the broken bond energy and, since about 1980, has been integrated with the statistical mechanical theory of Ising models which led to the integrated Hartman–Perdok roughening transition theory [3.11], later applied to modulated crystals [3.12]. These methods do not take into account the external habit-controlling factors, namely the effects of fluid composition and supersaturation, which are explicitly considered in the interfacial structure (IS) analysis [3.13]. An improvement in predicting morphology was represented by the application of ab initio calculations to the intermolecular interactions between tailor-made additives and crystal surface [3.14].

Computer facilities have promoted tremendous advances in all kinds of calculation necessary in the different sectors of crystal growth, enabling progress in theoretical approaches and sophisticated simulations which are now routine practice. A relevant instrumental advance was achieved when atomic force microscopy (AFM) was applied to study the features of crystal faces, giving new impulse to a topic that had always been the center of thorough research [3.15–18].

This chapter is devoted to the morphology of crystals grown from solution. In the first part, the theoretical equilibrium and growth shapes of crystals are treated from the thermodynamic and atomistic points of view. In the second part the factors affecting crystal habit will be considered with some specific examples. High-temperature solution growth, mass, and protein crystallization are excluded to limit the scope of the chapter.

3.1 Equilibrium Shape

When equilibrium is reached between a crystalline phase and its surroundings, the statistical amount of growth units exchanged between the two phases is the same and does not change with time. This implies that the crystallized volume remains constant, but nothing is specified about many important questions, such as:

1. The surface of the crystals, i. e., how large its extension is and which $\{hkl\}$ forms enter the equilibrium shape (ES).
2. The difference, if any, between the stable ES of a crystal immersed in either a finite or infinite mother phase and the unstable shape obtained when the activation energy for nucleation is reached.
3. How does the ES change when some adhesion is set up between the crystal and a solid substrate?
4. How can solvent and impurity concentrations affect the ES?

To address these questions, a few elementary concepts must be fixed to structure our language and a simple but effective crystal model adopted in the following.

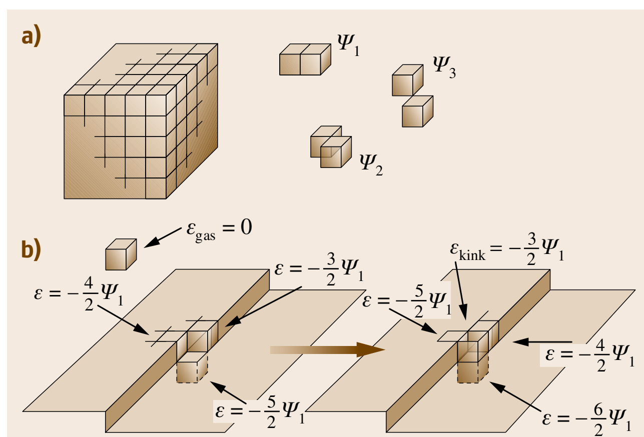

Fig. 3.1 **(a)** Kossel crystal; separation work between first (ψ_1), second (ψ_2), and third (ψ_3) neighbors. **(b)** When an atom enters a kink, there is a transition in the potential energy, the difference between final and initial stage being $-3\psi_1$ (first neighbors)

3.1.1 The Atomistic Approach: The Kossel Crystal and the Kink Site

Let us consider a perfect monoatomic, isotropic, and infinite crystal. The work needed to separate an atom occupying a *mean lattice site* from all its n neighbors is $\varphi^{\text{sep}} = \sum_i^n \psi_i$, where ψ_i is the energy binding one atom to its ith neighbor. We will see later on that this peculiar site really exists and is termed a *kink*. The potential energy (per atom) of the crystal will be $\varepsilon_{\text{p}}^{\text{c}\infty} = -(1/2)\varphi^{\text{sep}}$. The simplest model, valid for homopolar crystals, is due to *Kossel* [3.19]. Atoms are replaced by elementary cubes bounded by pair interactions, $\psi_1, \psi_2, \ldots, \psi_n$: the separation work between the first, second, and nth neighbors, with the pair potential decreasing with distance, $\psi_1 > \psi_2 > \ldots > \psi_n$ (Fig. 3.1a). In the first-neighbors approximation, the separation work for an atom lying in the crystal bulk is $\varphi^{\text{sep}} = 6\psi_1$. Thus, $\varepsilon_{\text{p}}^{\text{c}\infty} = -3\psi_1$. On the other hand, $\varepsilon_{\text{p}}^{\text{c}\infty}$ represents the variation of the potential energy that an atom undergoes when going from the vapor to a *mean lattice site*, which coincides with a well-defined surface site, as suggested by *Kossel* [3.19] and *Stranski* [3.2]. Once an atom has entered this special site, the potential energy variation of the considered system is equal to $-3\psi_1$ and so the separation work for an atom occupying this site is $\varphi_{\text{c}\infty} = 3\psi_1$ (Fig. 3.1b). A *kink* is the name adopted worldwide for this site, for practical reasons. Different historical names have been given: *repetitive step* [3.2, Z. Phys. Chem.] and *half-crystal position* [3.2, Annu. Univ. Sofia], both related to the physics of the site. In fact, deposition or evaporation of a growth unit onto/from a kink reproduces another kink, thus generating an equal probability for the two processes [3.20]. Moreover, the chemical potential (μ) of a unit in a kink is equal to that of the vapor. Hence, *kinks are crystal sites in a true* (and not averaged) *thermodynamic equilibrium*, as will be shown below.

3.1.2 Surface Sites and Character of the Faces

Flat (F) faces. A crystal surface, in equilibrium with its own vapor and far from absolute zero temperature, is populated by steps, adsorbed atoms, and holes. In the Kossel model all sites concerning the adsorption and the outermost lattice level are represented (Fig. 3.2). The percentage of corner and edge sites is negligible for an infinite crystal face, and hence we will confine our attention to the *adsorption and incorporation sites*. Crystal units can adsorb either on the surface terraces (ad_s) or on the steps (ad_l), with the same situation occurring for the incorporation sites (in_s, in_l).

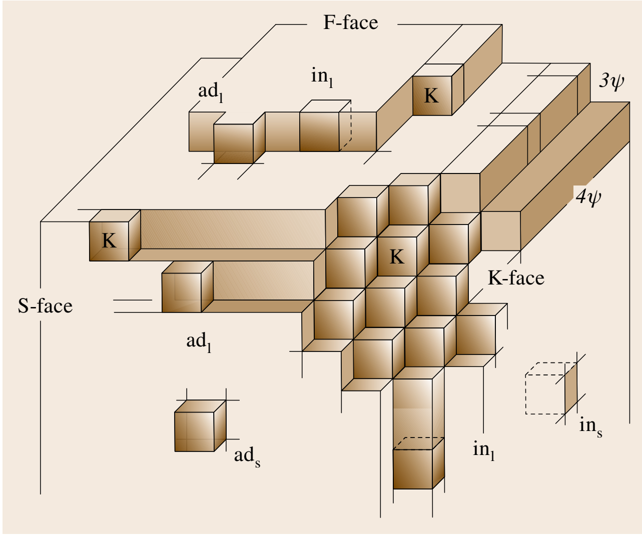

Fig. 3.2 The different types of faces of a Kossel crystal: {100}-F, {111}-K, and {110}-S faces. Adsorption (ad_s, ad_l) and incorporation (in_s, in_l) sites are shown on surfaces and steps. The uniqueness of the K (kink) site is also shown

The binding energies of *ad-sites* and *in-sites are complementary to one another*

$$\begin{aligned}\varphi_{ad_s}+\varphi_{in_s}&=\varphi_{ad_l}+\varphi_{in_l}\\&=2\varphi_{kink}\rightarrow\varphi_{ad}+\varphi_{in}=2\varphi_{kink}\,,\end{aligned}\tag{3.1}$$

which is generally valid since it depends neither on the type of face, nor on the crystal model, nor on the kind of lattice forces [3.21, p. 56]. The interaction of the unit in the kink with the crystal (φ_{kink}) consists of two parts. The first represents its *attachment energy* (φ_{att}) with all the *crystal substrate*, and coincides with that of an ad-unit, which implies

$$\varphi_{att}=\varphi_{ad}\,.\tag{3.2a}$$

The second is its *slice energy* (φ_{slice}), i.e., the interaction with the half of the outermost crystal slice, $\varphi_{slice}=(\omega/2)$, where ω is the interaction of the unit with all of its slice. Thus

$$\varphi_{in}=\varphi_{att}+\omega\,,\tag{3.2b}$$

and, from relation (3.1)

$$\varphi_{kink}=\varphi_{att}+\varphi_{slice}\,.\tag{3.2c}$$

Relation (3.2c) states that φ_{att} and φ_{slice} *of a growth unit are complementary to one another*. In fact, since φ_{kink} is constant for a given crystal, the higher the lateral interaction of one unit, the lower its interaction with the subjacent crystal. This criterion is of the utmost importance for understanding the growth morphology of crystals. Moreover, the binding of a growth unit must fulfil the qualitative inequality: $\varphi_{ad}<\varphi_{kink}<\varphi_{in}$. The quantitative treatment was elegantly addressed by *Kaischew* [3.3, 4], who calculated the coverage degree (θ_i) and other related quantities for every i-site of the surface drawn in Fig. 3.2

$$\theta_i=\{1+\exp[(\varphi_{kink}-\varphi_i)/(k_BT)]\}^{-1}\,,\tag{3.3}$$

where k_B is the Boltzmann constant. For a (001) Kossel surface and within the first-neighbors approximation, having assumed for the binding energy the standard value $\psi_1=4k_BT$ (valid for Au crystals not far from the melting point), the set of results shown in Table 3.1 was obtained.

From Table 3.1 it follows that:

1. Kinks are the only sites in thermodynamic equilibrium, being half filled and half empty at the same time.
2. Ad-units form a very dilute layer (row) which moves randomly on the surface (step edge) and hence cannot belong to the crystal.
3. In-units belong to the crystal, from which they may escape, generating a temporary hole, with a very low exchange frequency with respect to the other sites.

Looking at the face as a whole, the face profile can neither advance nor move backwards: hence, the face is in *macroscopic equilibrium*. Fluctuations around the equilibrium cannot change its flatness since the lifetime of the growth units in the ad-sites is very short and the vacancies generated among the in-sites are filled again in

Table 3.1 Coverage degree (3.3) and exchange frequency of growth units in the main surface sites of the (001) face of a Kossel crystal, assuming $\psi_1=4k_BT$ (after [3.21]). The exchange frequency is the reciprocal of the mean time between two successive evaporation (or condensation) events on the same i-site (i.e. s^{-1} indicates the number of exchanges per unit time in a given site)

Type of surface site	Separation work	Coverage degree θ_i	Exchange frequency (s^{-1})
$ad_{surface}$	ψ_1	0.0003	3.06×10^7
ad_{ledge}	$2\psi_1$	0.0180	3.02×10^7
kink	$3\psi_1$	1/2	1.54×10^7
in_{ledge}	$4\psi_1$	0.9820	5.55×10^6
$in_{surface}$	$5\psi_1$	0.9997	1.03×10^4

even shorter time. So, this kind of *equilibrium face* has been named an F-*type* (flat) *face*.

Kinked (K) and Stepped (S) Faces. The uniqueness of F-faces is even more evident when considering the behavior of the {111} form of a Kossel crystal, near the equilibrium. Only kinks can be found on this surface and hence only one type of binding exists ($3\psi_1$) among growth units, within the first neighbors. Since in this case no units exhibit bonds in their slice, $\omega = 0$, which implies: $\varphi_{ad} = \varphi_{kink} = \varphi_{in}$. With every ad-unit transforming into an in-unit, the surface profile is not constrained and hence fluctuates, with the mother phase, around the equilibrium. This interface is diffuse and the corresponding faces are termed K (kinked) *faces*.

The behavior of the {110} form may be thought of as midway between that of F- and K-faces, since only ledge-type sites exist, apart from the kinks. Any fluctuation near the equilibrium can lead either to the evaporation of an entire [100] step or to the growth of a new one. In the first case, it is sufficient that a unit leaves an in-ledge site to promote step evaporation, while in the second case the formation of an ad-ledge site automatically generates two kinks, allowing the filling of a new step. Both processes are not correlated, even for contiguous steps, since there are no lateral bonds ($\omega = 0$) in the outermost (110) slice; thus, steps can form (or disappear) independently of each other and may bunch, giving rise to an undulating profile around the zone axis. Parallel steps being the feature of this kind of surface, the corresponding faces are termed S-*type* (stepped) *faces*.

3.1.3 The Equilibrium Crystal – Mother Phase: The Atomistic Point of View

Here we will deal with the equilibrium between a crystal and its vapor; however, *our conclusions can be basically applied to solutions and melts as well*. Let us consider a Kossel crystal built by n^3 units (each having mass m and vibration frequency ν). Since the work to separate two first neighbors is ψ, the mean evaporation energy of the n-sized crystal is easily calculated

$$\langle \Delta H \rangle_{cn} = 3\psi[1-(1/n)] = \varphi_{cn} \ . \quad (3.4a)$$

Then, for an infinite-sized crystal,

$$\langle \Delta H \rangle_{c\infty} = 3\psi = \varphi_{c\infty} = \text{const} \ . \quad (3.4b)$$

This means that the *units belonging to the crystal surface* reduce the value of the mean evaporation energy and so they *cannot be neglected when dealing with finite crystals*.

An Infinite Crystal and Its Mother Phase

As shown in Appendix 3.A, the equilibrium pressure (p_{eq}^{∞}) between a monoatomic vapor and its infinite crystalline phase decreases with its evaporation work $\varphi_{c\infty} = (\varepsilon_v - \varepsilon_{c\infty})$, according to

$$p_{\infty}^{eq} = [(2\pi m)^{3/2}(k_B T)^{-1/2}\nu^3] \exp(-\varphi_{c\infty}/(k_B T)) \ , \quad (3.5a)$$

ε_v and $\varepsilon_{c\infty}$ being the potential energy of a unit in the vapor and in the infinite crystal, respectively. The term $p\,\mathrm{d}V$ can be neglected in $\langle \Delta H \rangle_{c\infty}$ with respect to the term ($\mathrm{d}U$). Assuming, as a reference level, $\varepsilon_v = 0$, it is easy to show that $\langle \Delta H \rangle_{c\infty} = \varphi_{c\infty} = -\varepsilon_{c\infty}$.

The Finite Crystal – The Link to the Thermodynamic Supersaturation

When dealing with finite crystals (3.5a) transforms simply by changing $\varepsilon_{c\infty}$ with ε_{cn}, which is the potential energy of a unit in the finite crystal. It ensues that $\varphi_{cn} = (\varepsilon_v - \varepsilon_{cn})$. The frequency ($\nu$) does not vary from large to small crystal size, so

$$p_n^{eq} = (2\pi m)^{3/2}(k_B T)^{-1/2}\nu^3 \exp(-\varphi_{cn}/(k_B T)) \ . \quad (3.5b)$$

From (3.5a) and (3.5b) the following fundamental relation is obtained:

$$p_n^{eq} = p_{\infty}^{eq} \exp[(\varphi_{c\infty} - \varphi_{cn})/(k_B T)] \ . \quad (3.5c)$$

Since $\varphi_{\infty} > \varphi_n$, (3.5c) shows that *the equilibrium pressure for finite crystals is higher than that for infinite ones*. This can also be written

$$\varphi_{c\infty} - \varphi_{cn} = k_B T \ln\left(p_n^{eq} / p_{\infty}^{eq}\right) = k_B T \ln \beta \ , \quad (3.6)$$

where $\beta = p_n^{eq}/p_{\infty}^{eq} = (p_{\infty}^{eq} + \Delta p)/p_{\infty}^{eq} = 1 + \sigma$ is the *supersaturation ratio* of the vapor with respect to the finite crystal. The (percentage) distance from equilibrium is $\sigma = (\Delta p / p_{\infty}^{eq})$, the exceeding pressure being $\Delta p = p_n^{eq} - p_{\infty}^{eq}$.

Equilibrium can also be viewed in terms of chemical potentials. Using the Helmholtz free energy, the chemical potentials, per unit, of the infinite and finite crystal read: $\mu_{c\infty} = -\varphi_{c\infty} - Ts_{c\infty}$ and $\mu_{cn} = -\varphi_{cn} - Ts_{cn}$. The vibrational entropies per unit, $s_{c\infty}$ and s_{cn}, are very close. Thus $\varphi_{c\infty} - \varphi_{cn} = \mu_{cn} - \mu_{c\infty} = \Delta\mu$ (Fig. 3.3). Hence, the following master equation for the equilibrium is obtained:

$$\Delta\mu = k_B T \ln \beta \ , \quad (3.7)$$

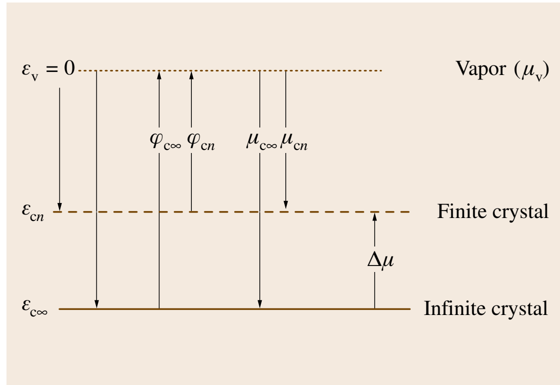

Fig. 3.3 Potential energy ε, evaporation work φ, and chemical potential μ of a growth unit in the vacuum, in a *mean site* of both finite and infinite crystal. $\Delta\mu = \mu_{cn} - \mu_{c\infty}$ is the thermodynamic supersaturation

where $\Delta\mu$ is the *thermodynamic supersaturation*. In heterogeneous systems a unit spontaneously goes from the higher chemical potential (μ') to the lower one (μ''). During the transition a chemical work ($\mu'' - \mu') = -\Delta\mu$ is gained, per growth unit.

The equilibrium between a finite crystal and its surroundings is analogous to the equilibrium of a spherical liquid drop of radius r (finite condensed phase 2) immersed in its own vapor (infinite dispersed phase 1). The phenomenological treatment is detailed in [3.21], where the two different equilibria are compared in the same way as we dealt with the atomistic treatment. Hence, one obtains the Thomson–Gibbs formula for droplets

$$\Delta\mu = k_B T \ln(p/p_{eq}) = \Omega_2 p_\gamma = 2\Omega_2(\gamma/r) , \quad (3.8)$$

where:

1. p_{eq} is the pressure of the vapor in equilibrium with a flat liquid surface
2. γ and Ω_2 are the surface tension at the drop–vapor interface and the molecular volume of the drop, respectively
3. The capillarity pressure p_γ at the drop interface defined by Laplace's relation ($p_\gamma = 2\gamma/r$) equilibrates the difference between the internal pressure of the drop (p_r) and the actual vapor pressure (p): $p_\gamma = (p_r - p)$.

The ratio (p/p_{eq}) is nothing else than β. When working with ideal or nonideal solutions, β is expressed by the concentrations (c/c_{eq}) or by the activities (a/a_{eq}), respectively. When a crystal is considered instead of a liquid drop, the system is no longer isotropic and then the radius r represents only the *size* of the crystal, as we will see later on. Nevertheless, the Thomson–Gibbs formula continues to be valid and expresses the relation among the deviation $\Delta\mu$ of the solution from saturation, the tension γ_{cs} of the crystal–solution interface, and the size of the crystals in equilibrium with the solution.

3.1.4 The Equilibrium Shape of a Crystal on a Solid Substrate

This topics has been deeply treated by *Kern* [3.22], who considered simultaneously both mechanical (capillary) and chemical (thermodynamic) equilibrium to obtain the ES of a crystal nucleating on a substrate from a dispersed phase. In preceding treatments, the Curie–Wulff condition and the Wulff theorem [3.23] only took into account the minimum of the crystal surface energy, the crystal volume remaining constant. According to [3.22], when n_A units of a phase A (each having volume Ω) condense under a driving force $\Delta\mu$ on a solid substrate B (heterogeneous nucleation) to form a three-dimensional (3-D) crystal (Fig. 3.4), the corresponding variation of the free Gibbs energy reads

$$\Delta G^{3\text{-D}}_{\text{hetero}} = -n_A \times \Delta\mu + \left(\gamma_i^A - \beta_{adh}\right) S_{AB} + \sum_j \gamma_j^A \, S_j^A , \quad (3.9)$$

where the second and the third term represent the work needed to generate the new crystal–substrate interface of area S_{AB} and the free crystal surfaces (of surface tension γ_j^A and area S_j^A), respectively.

The term $(\gamma_i^A - \beta_{adh})S_{AB}$ comes from the balance between the surface work lost ($-\gamma_B \times S_{AB}$) and gained ($\gamma_{AB} \times S_{AB}$) during nucleation. It is obtained from Dupré's formula: $\gamma_{AB} = \gamma_B + \gamma_i^A - \beta_{adh}$, where γ_{AB} is the crystal/substrate tension, γ_B is the surface tension of the substrate, γ_i^A is the surface tension of

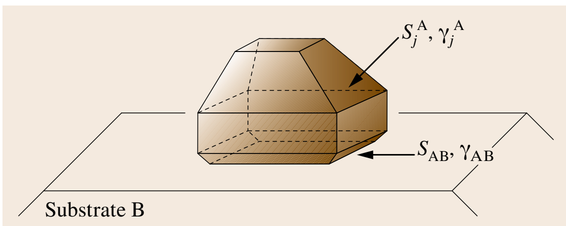

Fig. 3.4 Surface parameters involved in the balance of the free Gibbs energy variation when n_A units of a phase A condense on a solid substrate B to form a 3-D crystal (heterogeneous nucleation)

the i-face of the A crystal (when considered not in contact with the substrate), and β_{adh} stands for the specific crystal/substrate adhesion energy. At the (unstable) equilibrium of the nucleation any variation of $\Delta G^{3\text{-D}}_{hetero}$ must vanish. Then, under the reasonable assumption that also the specific surface tensions do not vary for infinitesimal changes of the crystal size,

$$\mathrm{d}\left(\Delta G^{3\text{-D}}_{hetero}\right) = -\,\mathrm{d}n_{A} \times \Delta\mu + \left(\gamma_i^{A} - \beta_{adh}\right)\mathrm{d}S_{AB} + \sum_j \gamma_j^{A}\,\mathrm{d}S_j^{A} = 0\,. \tag{3.10}$$

The fluctuation $\mathrm{d}n_A$ is related to those of the face areas ($\mathrm{d}S_j^A$ and $\mathrm{d}S_{AB}$) and to their distances (h_j and h_s) with respect to the crystal center. Then, (3.10) may be written in terms of $\mathrm{d}S_j^A$ and $\mathrm{d}S_{AB}$. Its solution is a continuous proportion between the energies of the faces and their h_j and h_s values

$$\frac{\gamma_1^A}{h_1} = \frac{\gamma_2^A}{h_2} = \cdots = \frac{\gamma_j^A}{h_j} = \frac{\gamma_i^A - \beta_{adh}}{h_s} = \text{const} = \frac{\Delta\mu}{2\Omega}\,. \tag{3.11}$$

This is the *unified Thomson–Gibbs–Wulff (TGW) equation*, which provides the ES of a crystal nucleated on a solid substrate:

1. The ES is a polyhedron limited by faces whose distances from the center are as shorter as lower their γ values.
2. The distance of the face in contact with the substrate will depend not only on the γ value of the lattice plane parallel to it, but also on its adhesion energy.
3. The faces entering the ES will be only those limiting the *most inner* polyhedron, its size being determined once $\Delta\mu$ and one out of the γ values are known.

The analogy between the crystal ES and that of a liquid drop on solid substrates is striking. It is useful to recall Young's relation for the mechanical equilibrium of a liquid drop on a substrate (Fig. 3.5)

$$\gamma_{sl} = \gamma_{lv}\cos\alpha + \gamma_{sv}\,, \tag{3.12a}$$

where α is the contact angle and γ_{sl}, γ_{lv}, and γ_{sv} are the surface energies of the substrate–liquid, liquid–vapor, and substrate–vapor interfaces, respectively. Besides, from Dupré's relation one obtains

$$\gamma_{sl} = \gamma_{sv} + \gamma_{lv} - \beta_{adh}\,. \tag{3.12b}$$

Since $-1 \le \cos\alpha \le 1$, the range of the adhesion energy (wetting) must fulfil the condition

$$2\gamma_{lv} \ge \beta_{adh} \ge 0\,. \tag{3.12c}$$

Adhesion values affect the sign of the numerator in the term $\left(\gamma_i^A - \beta_{adh}\right)/h_s$ (3.11).

The ES of the crystal is a nontruncated polyhedron when the crystal/substrate adhesion is null, as occurs for homogeneous nucleation. However, as the adhesion increases, the truncation increases as well, reaching its maximum when $\beta_{adh} = \gamma_i^A$. If the wetting

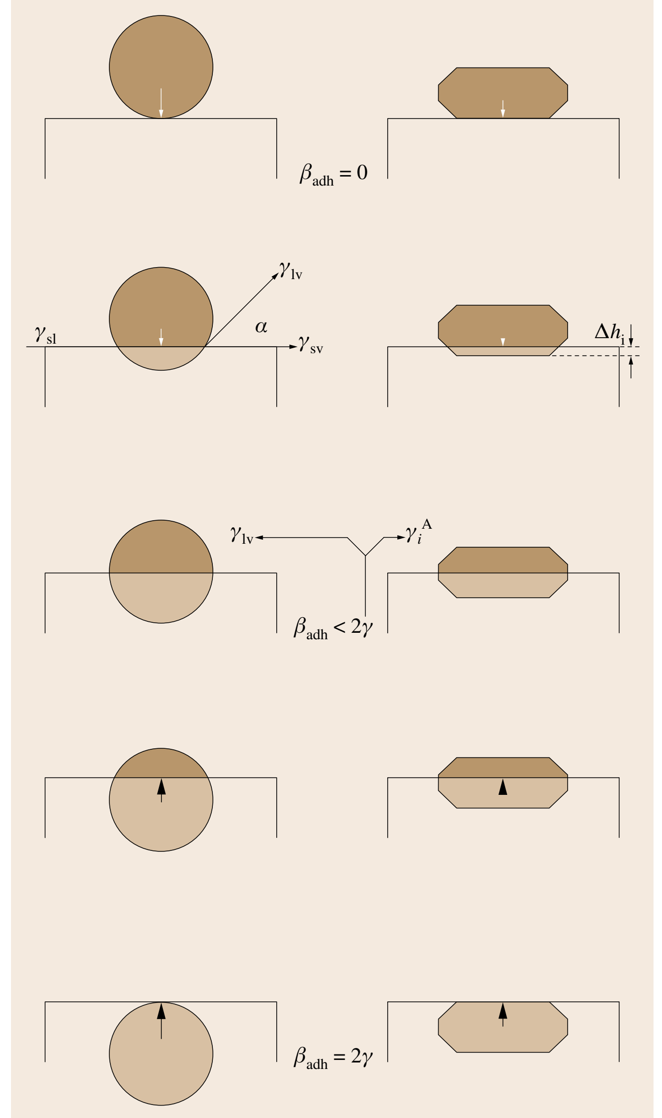

Fig. 3.5 Analogy between the equilibrium shape of a liquid drop on a solid substrate and that of a crystal, both heterogeneously nucleated. The adhesion energy β_{adh} rules both the contact angle of the drop with the substrate and the *crystal truncation*

further increases the truncation decreases, along with the thickness of the crystal cup. When β_{adh} reaches its extreme value, $2\gamma_i^A$, the crystal thickness reduces to a *monomolecular* layer.

The Equilibrium Shape of a Finite Crystal in Its Finite Mother Phase

Microscopic crystals can form in fluid inclusions captured in a solid, as occurs in minerals [3.25], especially from solution growth under not low supersaturation and flow. If the system fluctuates around its equilibrium temperature, the crystal faces can exchange matter among them and with their surroundings: then crystals will reach their ES, after a given time. *Bienfait* and *Kern* [3.24], starting from an inspired guess by *Klija* and *Lemmlein* [3.26], first observed the ES of NH_4Cl, NaCl, and KI crystals grown in small spherical inclusions (10–100 µm) filled by aqueous solution (Fig. 3.6). The crystals contained in each inclusion (initially dendrites) evolve towards a single convex polyhedron and the time to attain the ES is reasonable only for microscopic crystals and for droplet diameter of a few millimeters. The ES so obtained did not correspond to the maximum of the free energy (unstable equilibrium) but to its minimum, and then to a stable equilibrium. Finally, it was shown that both unstable and stable ESs are homothetic but with different sizes.

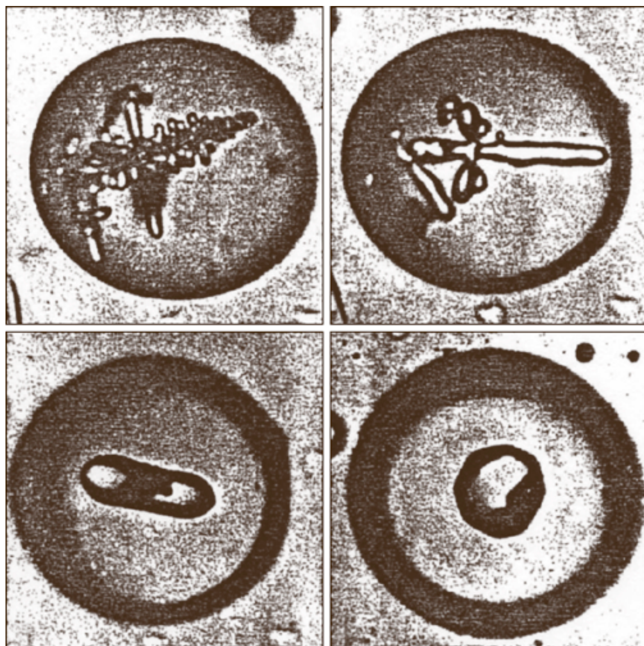

Fig. 3.6 The evolution towards equilibrium of NH_4Cl dendrites formed in an aqueous solution droplet (closed system) (after [3.24]). The total surface energy is minimized in passing from the dendritic mass to a single convex polyhedron at constant volume and T (equilibrium shape). Droplet size: 100 µm

3.1.5 The Stranski–Kaischew Criterion to Calculate the Equilibrium Shape

Without Foreign Adsorption

In the preceding sections, the surface tensions of the $\{hkl\}$ forms have been considered to be independent of crystal size. This is true when the crystal exceeds microscopic dimensions, but is no longer valid for those sizes which are very interesting both in the early stages of nucleation and in the wide field of nanosciences. In these cases, it should be reasonable to drop the use of the surface tension values, which are macroscopic quantities, to predict the equilibrium shape of micro- and nanocrystals. To face this problem, it is useful to recall the brilliant path proposed by *Stranski* and *Kaischew* [3.21, p. 170]. Their method, named the *criterion of the mean separation works*, is based on the idea that the mean chemical potential $\langle\mu\rangle_{c,m} = (1/m)\sum_{j=1}^{m}\mu_{j,c}$ averaged over all m units building the outermost layer of a finite facet, must be constant over all the facets, once the phase equilibrium is achieved. The chemical potential of a unit in a kink (Appendix 3.A) is

$$\mu_{c\infty} = -\varphi_{kink} - k_B T \ln \Omega_c + \mu^0 , \quad (3.13a)$$

and, by analogy, in a j-site of the surface

$$\mu_{j,c} = -\varphi_{j,c} - k_B T \ln \Omega_j + \mu^0 . \quad (3.13b)$$

The mean vibrational volumes being the same for every crystal sites, one can write for a generic site and especially at low temperature

$$\mu_{j,c} \approx -\varphi_{j,c} + \text{const} . \quad (3.14)$$

At equilibrium between a small crystal and its vapor: $\mu^{gas} = \langle\mu\rangle_{c,m}$. Subtracting the equality which represents the equilibrium between an infinite crystal and its saturated vapor ($\mu^{gas}_{saturated} = \mu_{c\infty}$) and applying relation (3.14), one can finally obtain

$$\Delta\mu = \mu^{gas} - \mu^{gas}_{saturated} = \langle\mu\rangle_{c,m} - \mu_{c\infty} \approx \varphi_{kink} - \langle\varphi\rangle_{c,m} .$$

That represents the *Thomson–Gibbs formula, valid for every face of small-sized crystals*

$$\varphi_{kink} - \langle\varphi\rangle_{c,m} \approx \Delta\mu = k_B T \ln \beta , \quad (3.15)$$

which allows one to determine the β value at which a unit (lying on a given face) can belong to the ES. Using (3.15), the ES can be determined without using the γ values of the different faces.

Let n_{01} and n_{11} be the number (not known a priori) of units in the most external $\langle 01\rangle$ and $\langle 11\rangle$ rows of a 2-D Kossel crystal (Fig. 3.7). Within the second neighbors, the mean separation works for these rows are

$$\begin{aligned}\langle\varphi\rangle_{01} &= (1/n_{01})[2\psi_1(n_{01}-1)+\psi_1+2\psi_2 n_{01}]\\ &= 2\psi_1+2\psi_2-(\psi_1/n_{01})\,, \qquad (3.16a)\\ \langle\varphi\rangle_{11} &= (1/n_{11})[2\psi_2(n_{11}-1)+\psi_2+2\psi_1 n_{11}]\\ &= 2\psi_1+2\psi_2-(\psi_2/n_{11})\,. \qquad (3.16b)\end{aligned}$$

The separation work from the kink is $\varphi_{\text{kink}} = 2\psi_1+2\psi_2$ and hence from (3.15) it ensues that

$$\begin{aligned}\Delta\mu &= \varphi_{\text{kink}}-\langle\varphi\rangle_{01} = \varphi_{\text{kink}}-\langle\varphi\rangle_{11}\\ &= (\psi_1/n_{01}) = (\psi_2/n_{11})\,, \qquad (3.16c)\end{aligned}$$

which represents both the phase equilibrium and the ES of the 2-D crystal. In fact the ratio between the lengths of the most external rows is obtained as

$$(n_{01}/n_{11}) = (\psi_1/\psi_2)\,. \qquad (3.17)$$

Equation (3.17) is nothing other than Wulff's condition $(h_{01}/h_{11}) = (\gamma_{01}/\gamma_{11})$ applied to this small crystal (3.11) [3.21, p. 172].

The *criterion of the mean separation work* can also answer a question fundamental to both equilibrium and growth morphology: how can we predict whether a unit is stable or not in a given lattice site? Let us consider, as an example, the unit lying at corner X of the 2-D Kossel crystal (Fig. 3.7). Its separation work, within the second neighbors, reads $\varphi_X = 2\psi_1+\psi_2$. Stability will occur only if the separation work of the unit X is higher than the mean separation work of its own row, i.e., $\varphi_X \ge \langle\varphi\rangle_{01}$ and hence, from (3.16c), $\varphi_X \ge \varphi_{\text{kink}}-\Delta\mu$. It ensues that $2\psi_1+\psi_2 \ge 2\psi_1+2\psi_2-\Delta\mu$. Finally, one obtains $\Delta\mu = k_BT\ln\beta \ge \psi_2$, which transforms to

$$\beta \ge \beta^* = \exp(\psi_2/k_BT)\,. \qquad (3.18)$$

This means that, when β is lower than the critical β^* value, the unit must escape from the site X, thus generating an ES which is no longer a square, owing to the beginning of the $\langle 11\rangle$ row. In other words, the absolute size (n_{01}, n_{11}) of the crystal homothetically decreases with increasing β (ψ_1 and ψ_2 being constant), as ensues from (3.16c). Since $\psi_1 > \psi_2$, $n_{01} > n_{11}$ and the ES will assume an octagonal shape dominated by the four equivalent $\langle 01\rangle$ sides, the octagon reducing to the square

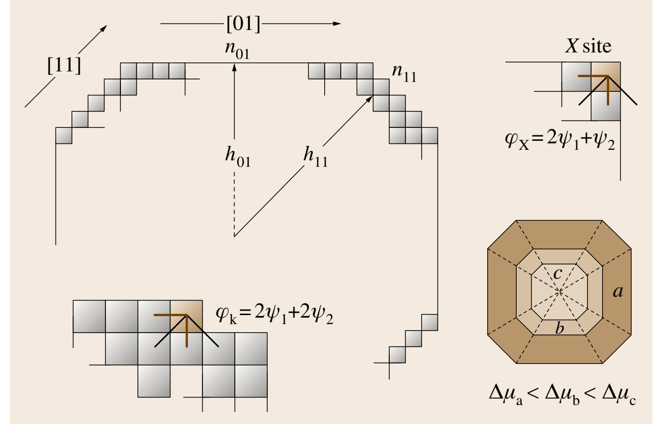

Fig. 3.7 To derive the equilibrium shape of a 2-D Kossel crystal by the criterion of the mean separation work, only the 1st, 2nd, ..., n-th-neighbors interactions are needed. The figure illustrates the scheme for the second-nearest neighbors approximation, the kink energy (φ_{kink}), the stability criterion for a unit X occupying a corner site and, finally, the 2-D equilibrium shape and size for $(\psi_1/\psi_2) = 1.5$ and for increasing supersaturation ($\Delta\mu$) values

when the number of units along the $\langle 11\rangle$ sides is reduced to $n_{11} = 1$. As $\Delta\mu = (\psi_2/n_{11})$, this occurs when $\Delta\mu = \psi_2$, which exactly reproduces what we have just found in (3.18).

With Foreign Adsorption

In growth from solution a second component (the solvent) intervenes in the interfacial processes, since its molecules interact strongly with the crystallizing solute. Here we are interested in studying how the ES of a crystal is affected by the presence of a foreign component. Two approaches exist in order to give a full answer to this problem:

1. The *thermodynamic* approach, which allows one to forecast the variation $d\gamma$ of the surface tension γ of a face due to the variation $d\mu_i$ of the chemical potential of component i of the system, when it is adsorbed. To calculate $d\gamma$ for a flat face one has to apply Gibbs' theorem [3.22, p. 171]

$$d\gamma = -s^{(s)}\,dT - \sum_i \Gamma_i\,d\mu_i\,, \qquad (3.19)$$

where $s^{(s)}$ is the specific surface entropy and $\Gamma_i = -(\partial\gamma/\partial\mu_i)_{T,s,\mu\neq\mu_i}$ corresponds to the excess of the surface concentration of component i. Solving (3.19) is not simple, even at constant T, since one has to know the functional dependence of Γ_i on

μ_i and hence on the activity a_i of component i. This means that one has to know Γ_i, which ultimately represents the adsorption isotherm of component i on a given face.

2. The approach grounded on the *atomistic view of equilibrium* proposed by *Stranski* [3.27, 28]. This model is based on the simplifying assumptions that foreign ad-units have the same size as those building the adsorbing surface (Kossel model) and that only first-neighbor interactions are formed between ad-units and the substrate. Three types of adsorption site are defined (Fig. 3.8), each of them having its own binding energy.

From (3.19) it ensues that adsorption generally lowers the surface tension of the substrate ($\Delta\gamma < 0$), so γ increases when an adsorption layer is reversibly desorbed. Let us denote the desorption work by $w = -\Delta\gamma \times a$, representing the increase per ad-site of the surface tension of the substrate (where a is the mean area occupied by an ad-unit) [3.29–31]. Thermodynamics allows to evaluate w, according to the type of adsorption isotherm [3.21, p. 175]

$$w = -k_BT\ln(1-\theta) - (\omega/2)\theta^2 \quad \text{(Frumkin–Fowler type)}, \tag{3.20a}$$

$$w = -k_BT\ln(1-\theta) \quad \text{(Langmuir type)}, \tag{3.20b}$$

valid when ω, the lateral interaction of the ad-unit with the surrounding, vanishes and

$$w = -k_BT \times \theta \quad \text{(Henry type)}, \tag{3.20c}$$

when the coverage degree in ad-units is low ($\theta \ll 1$). In the last case one can compare the θ values of the different sites remembering that, at given bulk concentration of foreign units, the coverage degree for an isolated adunit behaves as $\theta \propto \exp(\varphi_{ads}/(k_BT))$. Here, φ_{ads} is the binding energy of the ad-unit with the substrate. From (3.20c) one can write

$$\frac{w_i}{w_j} = \frac{\theta_i}{\theta_j} = \exp\frac{(\varphi^i_{ads} - \varphi^j_{ads})}{k_BT}, \tag{3.21}$$

which shows that the difference in the desorption works is very sensitive to the φ_{ads} value. This can be verified by applying (3.21) to the three sites in Fig. 3.8a of a cubic Kossel crystal and remembering that, in this case, φ_{ads} is equal to ψ_{ads}, $2\psi_{ads}$, and $3\psi_{ads}$, where $\psi_{ads} = k_BT$, $2\times k_BT$, $3\times k_BT, \ldots$ is the energy of one adsorption bond. An important consequence of this reasoning is that *the chemical potential of an infinite crystal* (and hence its solubility) *is not changed by the adsorption of impurities on its surfaces*, as is proved by the balance detailed in Fig. 3.8b, which represents the initial and final stages of the desorption of a foreign unit from a kink site.

Let us now evaluate how the ES of a finite crystal changes, by applying the criterion of the mean separation works to the mentioned Stranski adsorption model. The stability of a unit in the corner site X when adsorption occurs (Fig. 3.9a) can be compared with that obtained without adsorption (3.18). The separation work of a unit in X is $\varphi^{ads}_X = 2\psi_1 + \psi_2 + 2w_1 - w_2$, where w_1 and w_2 are the desorption works for the two ad-sites, respectively.

The stability criterion requires $\varphi^{ads}_X \geq \langle\varphi\rangle_{01}$ and hence, from (3.16c), $\varphi^{ads}_X \geq \varphi_{kink} - \Delta\mu$.

Since $\varphi_{kink} = 2\psi_1 + 2\psi_2$, stability occurs only when $\Delta\mu \geq \psi_2 - (2w_1 - w_2)$. This implies

$$\beta^*_{ads} \geq \exp\{[\psi_2 - (2w_1 - w_2)]/(k_BT)\}. \tag{3.22}$$

Comparing (3.22) with (3.18) it turns out that the stability of the corner unit occurs at lower β value ($\beta^*_{ads} < \beta^*$) if $w_2 < 2w_1$. This means that, if the impurity fulfils the inequality $w_2 < 2w_1$, the ES is a pure square crystal at a β value lower than that predicted in pure growth medium. The $\langle 11\rangle$ edges begin to appear when the corner units can escape from the crystal (instability of the X-site), i. e., if $\beta < \beta^*_{ads}$. On the contrary, if $w_2 > 2w_1$ the impurity adsorption does not favor the stability of the corner unit and an octagonal ES forms at a β value lower than that found in pure growth medium. Figure 3.9b illustrates how the smoothing of a 2-D K-face can be obtained with foreign adsorption [3.21, pp. 178–189]. The energy difference between the final and initial stages is that which we obtained for the X-site, so the conclusions are obviously those fulfilling (3.22). Figure 3.9c concerns the stability of an ad-unit (site A) on

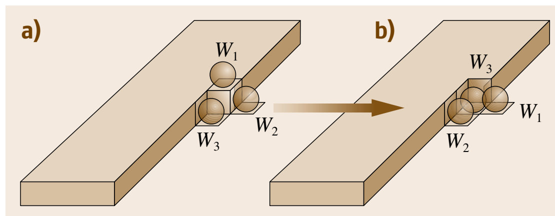

Fig. 3.8 **(a)** The three types of adsorption sites on a Kossel crystal (only 1st neighbors interaction). Each ad-site has its binding energy: $w_1 < w_2 < w_3$. **(b)** Energy balance representing the initial a) and the final b) stage of the desorption of a foreign unit from a kink-site. The binding energy does not vary on the adsorbance (after [3.21])

the $\langle 10 \rangle$ edges in the presence of foreign adsorption. The separation work of a unit at A is $\varphi_A^{ads} = \psi_1 + 2\psi_2 + 2(w_2 - w_1)$. The stability criterion for this site requires

$$\beta^*_{ads} \geq \exp\{[\psi_1 - 2(w_2 - w_1)]/(k_B T)\} , \tag{3.23}$$

while, in analogy with (3.18), the stability criterion without impurities reads

$$\beta^* \geq \exp\left(\frac{\psi_1}{k_B T}\right) . \tag{3.24}$$

Thus, the foreign adsorption favors the stability of the growth units at site A if $\beta^*_{ads} < \beta^*$ and hence if $w_2 > w_1$. If this occurs, $\langle 10 \rangle$ edges transform from flat to rough owing to the random accumulation of ad-units.

Transferring these results from 2-D to 3-D crystals, the conditions expressed by (3.22) and (3.23), respectively, rule the transition of character K→F and F→K due to foreign adsorption.

The changes in the ES when adsorption occurs can now be calculated, according to the Stranski–Kaischew principle of the *mean separation work*. This means that, when an entire $\langle 10 \rangle$ or $\langle 11 \rangle$ row is removed from a 2-D crystal in the presence of adsorbed impurities, the mean separation works must fulfil the condition $\langle \varphi \rangle_{01}^{ads} = \langle \varphi \rangle_{11}^{ads}$, in analogy with (3.16a) and (3.16b). From calculation it ensues that

$$\left(\frac{n_{01}}{n_{11}}\right)_{ads} = \frac{\psi_1 - 2(w_2 - w_1)}{\psi_2 - (2w_1 - w_2)} , \tag{3.25}$$

which can be compared with the analogous expression (3.17) obtained without foreign adsorption

$$\left(\frac{n_{01}}{n_{11}}\right)_{ads} : \left(\frac{n_{01}}{n_{11}}\right) = \frac{\psi_1 - 2(w_2 - w_1)}{\psi_2 - (2w_1 - w_2)} : \frac{\psi_1}{\psi_2}$$
$$= \frac{\psi_1\psi_2 - \psi_2 \times 2(w_2 - w_1)}{\psi_1\psi_2 - \psi_1 \times (2w_1 - w_2)} . \tag{3.26}$$

Hence the importance of the $\langle 10 \rangle$ edges in the ES increases to the detriment of the $\langle 11 \rangle$ edges, if the condition $2(w_2 - w_1)/(2w_1 - w_2) < \psi_1/\psi_2$ is fulfilled. A simpler solution is obtained within the first-neighbors approximation ($\psi_2 = 0,\ \psi_1 = \psi$). Remembering that, without foreign adsorption, the ES is a pure square, in the presence of impurities some changes should occur. In this case, expression (3.25) reduces to $(n_{01}/n_{11})_{ads}^{1st} = (\psi - 2(w_2 - w_1))/(w_2 - 2w_1)$.

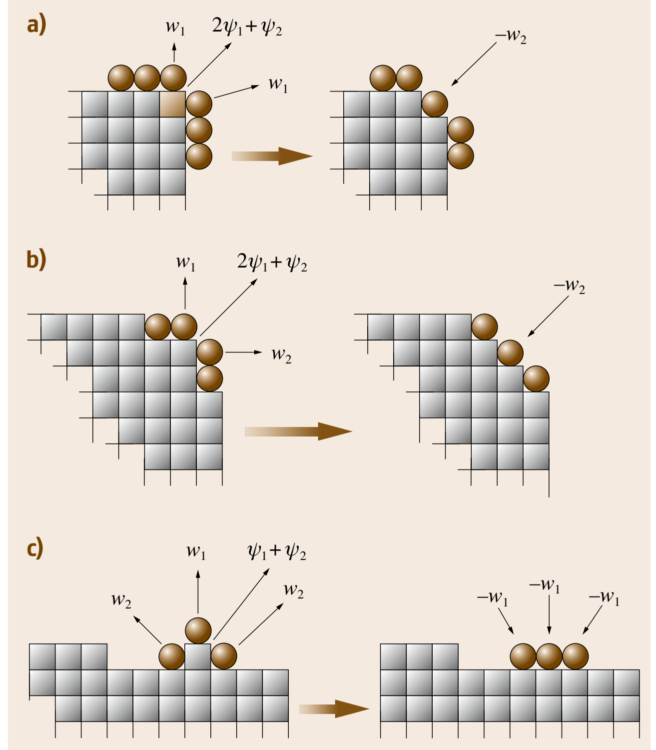

Fig. 3.9a–c The criterion of the mean separation works applied to the Stranski adsorption model in the second-neighbors approximation. **(a)** The first balance corresponds to the stability of the X site (*corner*) in the presence of foreign adsorption. **(b)** The second balance shows that the $\langle 11 \rangle$ row becomes smooth with foreign adsorption if $w_2 > 2w_1$. **(c)** The third balance describe the energies involved in calculating the stability of an ad-unit (site A) on the $\langle 10 \rangle$ edges in the presence of foreign adsorption. The figure has been inspired by [3.21]

The $\langle 11 \rangle$ row will exist if $n_{11} > 0$. Taking into account that necessarily $n_{10} > 0$, one must have simultaneously that $\psi > 2\psi(w_2 - w_1)$ and $w_2 > 2w_1$. The first inequality is verified by (3.23) since the ES of a finite crystal needs a supersaturated mother phase ($\beta^*_{ads} > 1$), so the only way for the $\langle 11 \rangle$ row to exist is for the second inequality also to be true, as found above. Summing up, the method of the *mean separation work* is a powerful tool to predict both qualitatively and quantitatively the ES of crystals, with and without foreign adsorption, without an a priori knowledge of the surface tension of their faces.